UNIVERSITÀ DEGLI STUDI DI MILANO

Doctorate School in Chemical Sciences and Technologies

Department of Chemistry

Ph.D. course in industrial chemistry – XXVII cycle

Gas management as possible solution for long-life Li-ion batteries

PhD Candidate

Andrea Carrà (R09747)

Tutor: Prof. Alberto Vertova

Co-Tutor: Dr. Alessandra Fernicola

PhD course Coordinator: Prof. Dominique Roberto

Director of the School: Prof. Silvia ARDIZZONE

A.A. 2013-2014

INDEX

Introduction

Scientific and economic rationale

i.1. Technological and economical context of the work

The lowering of fossil fuels and the accumulation of their pollutants in the environment have led to develop new energy vectors. For future energy supply, electrochemical energy storage devices (EESD) represent the technology enabling the use of power sources alternative to fossil fuels.

EESD consist of one or more electrochemical cells, which convert stored chemical energy into electrical energy. Each cell contains a positive and a negative pole, which are called cathode and anode. Inside EESD, cells could be connected either in series or in parallel. In the case of cells configured in series, the nominal voltage of the EESD is the summation of the voltage due to each single cell. On the contrary, cells configured in parallel lead to increase the current released by EESD, without inducing any enhancement of the voltage. A proper configuration of cells connection within the EESD makes it possible to supply any kind of electrical circuit.

EESD could be primary (disposable) or secondary (rechargeable). Primary devices do not support recharge because the inner chemistry of the cells is not reversible and thus reagents could not be replaced in any way. On the contrary, secondary devices reach an equilibrium by discharging the cells and thus reagents could be electrochemically replaced.

Presently, EESD are widely used for many applications such as portable electronic and electro-mobility. Moreover, the relative segments of the market are strongly influenced by EESD technology and it's not surprising that energy storage is becoming one of the main economic issues.

Although a serious economic crisis has affected several segments of the market, the battery market has been growing for all of the present decade. One of the main reasons for its growth is the implementation of energy storage solutions within new technological contexts. Figure ii-1 reports an example of the market trend for Li-ion batteries (LiBs). The trend shown ranges from year 2000 to 2013. The market is obviously growing also thanks to the use of LiBs in the automotive segment [1].

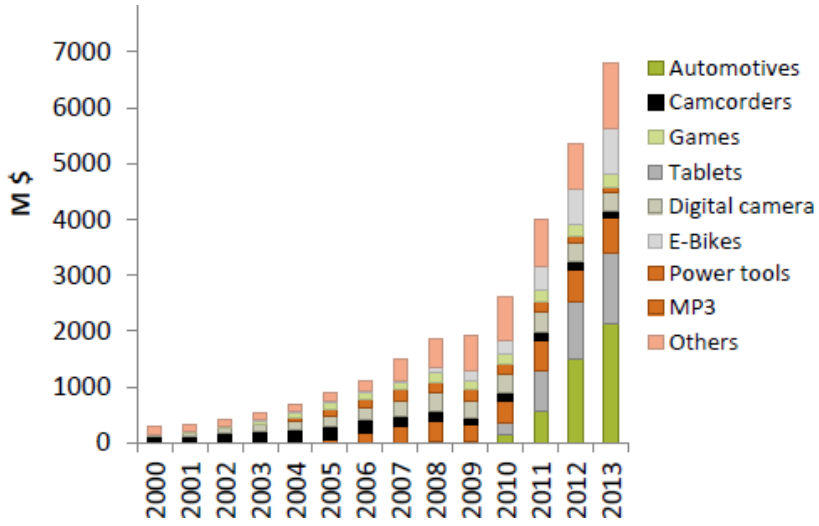

Figure ii-1 Market Li-ion cells [1]

The reason for the economic success of Li-ion cells could be easily explained considering technological improvements provided by them. In fact, Li-ion technology is characterised by a low memory effect, low self-discharge and high energy densities. In Figure i-2 the main classes of battery have been classified according to the Ragone plot [1]. Among all EESDs, Li-ion cells exhibit an energy density (200-300 Wh/kg) much higher than all of the other batteries (50-80 Wh/kg, Ni-MH), nowadays available on the market.

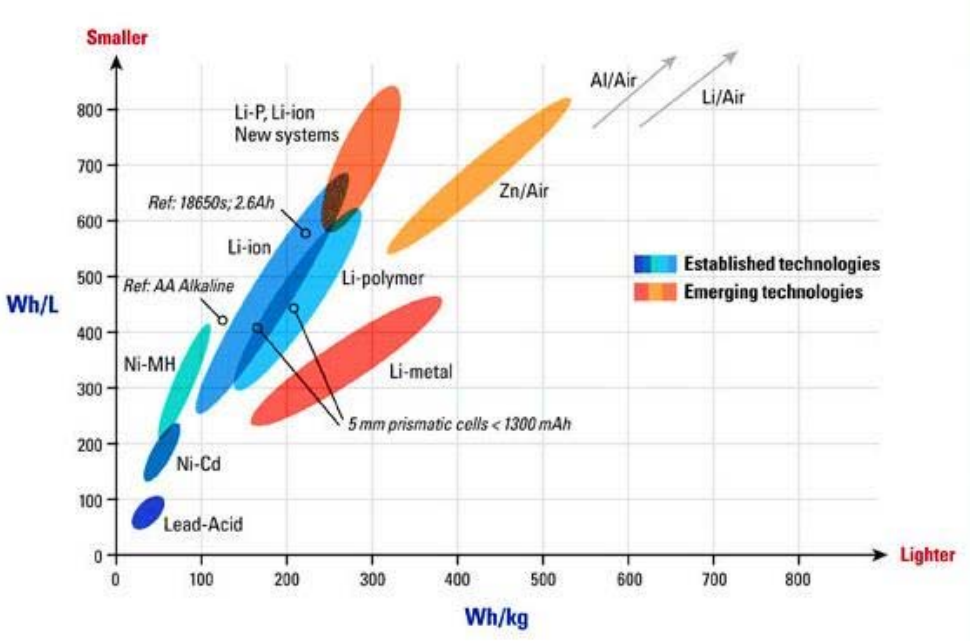

Figure i-2 classification of energy storage devices [1]

Moreover, considering that 70 L of diesel fuel (4000 Wh/kg) can power a car to travel for 800-1000 Km, one can calculate that an engine supplied by Li-ion batteries should be able to cover distances of 60-80 km. Thus Li-ion technology could replace fossil fuels for short

distance travels, or they could be used in combination with fossil fuel in hybrid engine, in order to save fuel for long distances travels.
Summarising, Li-ion technology is the most advanced type of rechargeable devices at the state of the art.

Despite the relevant performances that characterise LiBs, the safety requirements for this kind of batteries are stricter than all the other energy storage devices. In particular, the higher the energy of the battery, the more relevant is the risk of explosion.
For LiB manufacturers failures and recalls are some of the main causes for profit loss. Figure i-3 describes the economic impact that safety issues determine on Li-ion market (**REF-1**). In particular, Figure i-3-a reports the case of the LiBs production of one manufacturer for the year 2006. Looking on the chart one can notice that battery failure determines a loss of profit of 62% of the expected operational margin. In conclusion, the improvement of LiBs stability is becoming a segment of EESD market.

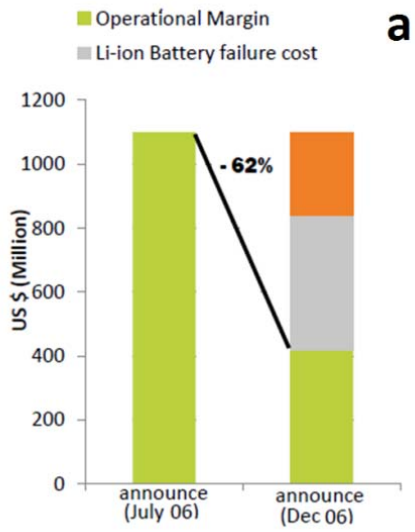

Figure i-3 the economic impact of safety

According to this economic rationale, many research projects have been aimed at understanding the chemical causes of LiBs failure [3]. A complete review about the chemistry of LiBs has been reported in the chapter 1.2. A short summary about LiBs failure modes has been reported below, in order to provide the reader with an introduction to Li-ion technology topics.
During charge and discharge processes energy is stored into the LiB and then released by it. Thus when the device is full of energy, irreversible side reactions might occur within the battery environment and can lead to cell instability.

Usually, side reactions stop thanks to the passivation of the electrodes. However, electroactive species could be gradually consumed, if the electrodes are not properly passivated. In these conditions side reactions proceed, reducing the cell capacity (capability of the cell to store energy). Frequently, the users try to recover capacity by prolonging the time of charge (overcharge), but capacity cannot be recovered if the electroactive species are irreversibly consumed. Thus overcharge can further stimulate side reactions, generating several gaseous side products. Gasses evolve and accumulate in the head space of the cell, increasing the internal pressure of the battery [4]. Overpressure results in the bulging of the battery case. Inflammable vapours could be released, whether the battery case opens under the effect of an increasing internal pressure. For these reasons the abuse of a Li-ion batteries can determine serious safety issues.

i.2. Aim of the project

In this project an analytical method based on a multi-technique approach is proposed to investigate pressurisation phenomena within Li-ion cells. In particular, the project is aimed at characterising the causes that determine the pressure build-up into Li-ion cells.
For this purpose the research work has been divided in four main tasks, which are briefly summarised below:

In the first task a research on literature has been aimed at identifying the battery materials most frequently used into Li-ion cells. Moreover, the inner chemistry of the cell has been studied, highlighting the most relevant gaseous side products and the analytical approaches conventionally used to investigate their generation. The end point of this task is the identification of a cell configuration, which could be used to develop a lab-scale Li-ion cell, useful for the non-perturbative investigation of gas evolution in the cells.

In the second task the cell prototype has been designed and optimised. A test protocol based on galvanostatic cycling and electrochemical impedance spectroscopy has been used to validate the cell prototype. The task concluded by comparing the experimental data with the results present in literature.

In the third task a cell suitable for gas detection has been designed and developed by using standard vacuum components. Several types of optical components have been evaluated, optimising the gas cell configuration. The gas detection system has been

calibrated and validated. This task concluded by assessing dynamic range, limit of detections and reproducibility.

In the fourth task electrochemical and spectroscopic analyses have been coupled, characterising the evolution of gas in the Li-ion cells. Investigations have been performed under resting and operative conditions. At the end of cell operations all devices have been disassembled and their electrodes have been characterised by electron scanning microscopy. The task concluded defining a relationship between gas evolution and the operative conditions of Li-ion cells.

The project concludes by proposing a gas management solution according to experimental results and literature data about specific scavengers.

i.3. References

1. The Worldwide rechargeable Battery, market 2013 – 2025. Courtesy of Avicenne company, Energy division (2013)
2. T. Christen, M. W. Carlen Journal of Power Sources 91 _2000. 210–216 2000. 210–216
3. P. Arora, R.E. White and M. Doyle. J. Electrochem. Soc. 1998 volume 145, issue 10, 3647-3667
4. C.L Campion, W. Li, W.B. Euler, B. L. Lucht, B. Ravdel, J.F. DiCarlo, R. Gitzendanner and K. M. Abraham , Electrochem. and Solid -State Lett., 7, A194 (2004)

Chapter 1

A review about Li-ion cells

1.1. Cell configuration

In general, Li-ion cell devices consist of two electrodes, separated by an insulator (separator) which prevents a direct contact between electrodes (shorting). The circuit is closed by an electrolyte, which migrates through the separator ensuring conduction by ion transport; a representative scheme is reported in Figure ii-1 [1].

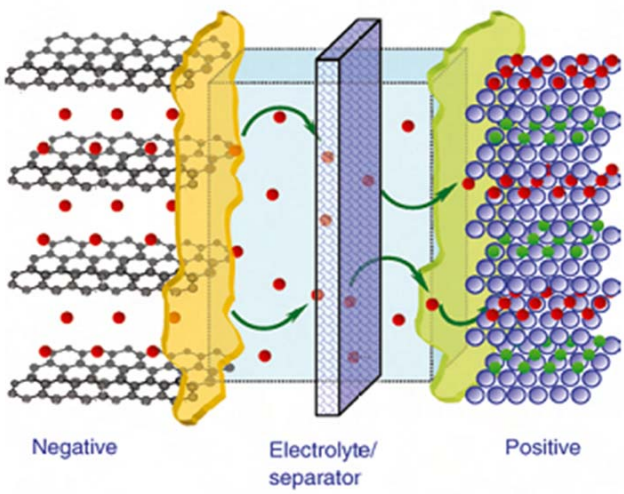

Figure ii-1 Scheme of Li-ion cell.

Commercial Li-ion cell have cathodes that consist of lithium metal oxides such as $LiCoO_2$, whereas anodes are carbonaceous materials such as graphite. The cell starts to work by charging, thanks to an external current over imposed to the cell by a power supplier.

During charging, cathode and anode are positive and negative polarised. The electrons in the Valence bands of the Cathode (VbC) are transferred in the Conduction bands of the Anode (CbA). According to the electroneutrality principle, by reducing the electron density of the cathode, Li^+ cations are less retained by the lattice and thus they could be easily released into the electrolyte (deinsertion process).

At the anode side, the additional electron density attracts Li^+ from the electrolyte and induces an increasing repulsion between graphitic plains. Repulsion compels planes to slide one against the other, leading to trigonal primitive cell. This structural modification generates new sites, wherein Li^+ could be easily intercalated compensating interplanar repulsions (intercalation process).

When the cell is charged, the external current stops to flow. In this condition the electrons stored in the anode do not spontaneously go back to the cathode. This happens because intercalated Li^+ cations help to retain exceeding electrons.

When the cell is discharged the Li^+ cations cannot retain these electrons, so they leave the anode and go back in the cathode. Whenever an electron leaves the anode for the cathode, it leaves an electron-state with high energy (anode conduction band) to reach an

electron-state characterised by a lower energy (cathode valence band). Summarising, the wider is the energy gap (CbA vs. VbC), the higher the electromotive force of the cell will be.

Taking into account the electroneutrality principle, the number of electrons available into Li-ion cell must be equal to the number of Li^+ cations available from the pristine electrodes. Unfortunately, more of the side reactions in Li-ion cell, irreversibly consume lithium cations, reducing the cell capacity. The highest loss of Li^+ is usually observed during the first charge/discharge cycles, during which the electrolyte is consumed by electrodes, generating passivation layers called SEI (Solid Electrolyte Interphase). SEI consists of insoluble side products, which remain embedded on the electrodes surface. Side products consist of both ionic and organic species and thus SEI is able to behaves as a secondary conductor. The physical properties of the SEI depends mainly on the electrolyte/electrode couple implemented in the Li-ion cell. Summarising, the quality of the SEI determine the battery performances.

The cathode and the anode materials more frequently used in Li-ion cells have been reported in Table 1 and Table 2, respectively. The rationale for the choice of the anode/cathode couple is to maximize the Energy Density of the cell (ED). According to the following formalism, ED=OV•C, the Energy Density depends on both Operating Voltage (OV) and the discharge Capacity (C).

Table ii-1 Most common cathode materials (lit. review)

Structure	Formula	Operating Voltage (OV)	Capacity (C)	Note	Reference
		Volt (vs Li^+/Li)	$mAhg^{-1}$		
Layered oxides	$LiCoO_2$	2.0-4.2	~140	Toxic	[4]
	$LiCoO_2$	2.0-4.7	~200	With Al_2O_3 nano-coating	[5]
	$LiNiO_2$	3.2-3.8	~180	Not completely stable	[6]
	Li_2MnO_3	2.0-4.5	~250	Jahn-Teller distortion at 3V	[7]
	$LiNi_{0.85}Co_{0.15}O_2$	3.2-4.7	~180	High capacity loss under 3V	[8]
	$LiNi_{0.8}Co_{0.15}Al_{0.05}O2$	3.0-4.5	~197	High capacity loss under 3V	[9]
Spinel	Li_2MnO_3	2.0-4.8	~280	With $AlPO_4$ nano-coating	[**10**]
	$LiMn_2O_4$	3.0-4.0	~120	Mn^{3+} disproportionation	[**11**]
	$LiMn_{1.5}Ni_{0.5}O_4$	3.5-4.7	~140	NiO impurities reduce OV	[**12**]
	$LiMn_{1.5}Fe_{0.5}O_4$	3.5-5.0	~120	disordered phase reduced performance	[**12**]
	$LiMn_{1.5}Co_{0.5}O_4$	3.5-5.2	~110		[**12**]
Olivine	$LiFePO_4$ /C	2.0-3.4	~160	(90 mAhg-1 without Carbon)	[**13**]
	$LiCoPO_4$ /C	2.0-4.8	~170	(100 mAhg-1 without Carbon)	[**13**]
	$LiNiPO_4$ /C	2.0-5.1	~160	(90 mAhg-1 without Carbon)	[**13**]

Table ii-2 Most common anode materials (lit. review)

Structure	Formula	Operating Voltage (OV)	Capacity (C)	Note	Referece
		Volt (vs Li^+/Li)	$mAhg^{-1}$		
Carbonaceous	Graphitic carbon (LiC_6)	0.0-2.0 V	~400	Susceptible to exfoliation, reversible Li^+ intercalation	[**14**]

	Hard carbon (LiC_6)	0.0-2.0 V	500-1000	Reversible Li^+ intercalation, heterogeneous response	[**15**]13
	Doped carbon (Li-N/C_6)	0.0-2.0 V	~550	Residue compounds reduce Li+ intercalation reversibility	[**16**]
Other anodes materials	$Li_4Ti_5O_{12}$/C	1.2-2.0	~160	(90 mAhg-1 without Carbon)	[**17**]
	Sn/C	2.5-0.0	~1280	Low reversible Li^+ intercalation	[**17**]
	Amorphous Sn_2O	0.0-1.5	~600	mechanical degradation	[**18**]

Although $LiCoO_2$ has not the highest discharge capacity, it exhibits unique properties. In particular, it shows a good operating voltage, sufficiently high capacity and it does not need the support of an electronic conductor (carbon), thanks to the electronic-bands developed along the Co-planes. For these features, $LiCoO_2$ is one of the most frequently implemented cathodes into Li-ion cells and it represents a benchmark for the emerging cathode technology.

On the anode side, graphitic carbon is preferentially used, although emerging anodes materials exhibit higher capacities. The reason why emerging anode are barely used is related to their strong capacity fade [**20**]. On the contrary, hard carbon could represent an alternative to graphite, but its application is limited by its less conductive properties and its relative high capacity loss after the first discharge cycle. Moreover, hard carbons support the growth of Li-dendrimers, which could be generated around sp^3 aliphatic domain, increasing the risk of cell shorting.

The solvents most frequently used in Li-ion cells are reported in Table 3 along with their chemical and physical proprieties as reported in literature [3].

Table ii-3 Most common solvents for LiB electrolytesε,η,ρ, represent permittivity, viscosity and density, respectively Errore. L'origine riferimento non è stata trovata..

Class	Solvent	Acronym	Melting	Bolling	ε	η	ρ	Note
			°C	°C		(mPa/s)	g/cm^3	
Carbonates	Diethyl carbonate	DEC	–43.0	126.8	28.059	0.7529	0.969	
	Dimethyl carbonate	DMC	4.6	90	31.075	0.5902	1.063	
	Ethylene carbonate	EC	36.5	238	90.36	1.9	1.321	at 40°C
	Ethyl methyl carbonate	EMC	–	–	2.4	0.65	1.007	
	Propylene carbonate	PC	–54.53	242	64.95	2.512	1.199	
Ethers	2-Methyltetrahydrofuran	MTHF	–137.2	79.9	6.75	–	0.854	at 20°C
	Dimethoxy ethane	DME	–58	84.50	7.075	0.407	0.861	
	1,3-Dioxolane	DIOX	.97.22	76.5	.	0.6	1.064	at 20°C
	Tetrahydrofuran	THF	–108.5	65.965	7.43	0.459	0.881	
Esters	γ-Butyrolactone	GBL	–43.53	204	39.1	17.315	1.124	
	methyl acetate	MA	–98.05	56.868	6.68	0.364	0.927	at 20°C

	methylformate	MF	–99.0	31.75	8.5	0.328	0.966	
Nitrogen Comp.	3-Methyl-2-oxazolidinone	3Me2OX	15.9	74–75	77.5	2.450	1.170	
	n-Butylamine	n-BU	–49.1	77.4	4.88	0.681	0.738	
	Acetonitrile	AN	–48.835	81.60	35.95	0.341	0.776	
Sulphureted comp.	Sulfolane	SL	28.45	287.3	43.30	1.0287	1.261	
	Dimethyl sulfoxide	DMSO	18.54	189	46.5	1.992	1.095	

As reported in Table 3, ethylene carbonate (EC) shows good solvation properties (highest permittivity, ε=90) but it is solid at room temperature (melting point 35°C) and therefore it should be used in combination with other solvents of the same class such as propylene carbonate (PC), dimethyl carbonate (DMC) and diethyl carbonate (DEC). PC is a solvents characterised by permittivity values higher than the other co solvents (ε=60). Unfortunately, it co-intercalates with Li^+ the interplanar regions of the graphite, promoting the anode exfoliation [**21**]. For these reasons DMC is preferentially used in combination with EC, even though the permittivity of the mixture is lower than pure PC based electrolyte (ε = 45 for a mix EC/DMC 1:1v/v). Figure ii-2 reports a scheme, which sketches the mechanism for anode exfoliation.

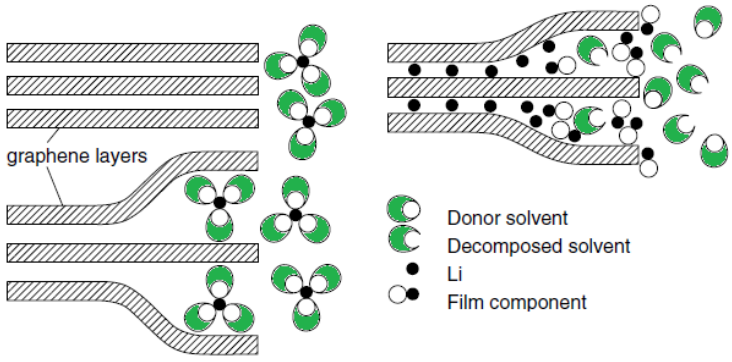

Figure ii-2 Scheme of anode exfoliation [Errore. L'origine riferimento non è stata trovata.**]**

Table ii-4 reports the salts used in Li-ion devices and relative conductivity.

Table ii-4 Short survey of some salts and their conductivities

Class	Formula	Name	Conductivity	Solvent	Ref.
			mS/Cm (1M)	w/w	
Chlorates	$LiClO_4$	Lithium perchlorates	8.4	EC/DMC 1:1	[**22**]
Arsenate	LiAsF6	Lithium esafluoro arsenate	8.2	EC/DMC 1:1	[**22**]
Phosphates	$LiPF_6$	Lithium esafluoro phosphate	7.0	EC/DMC 1:1	[**22**]
	$LiP(C_2F_5)_6$	Lithium esa(pentafluoroethyl) phosphate	8.2	EC/DMC 1:2	[**23**]
Borate	$LiBF_4$	Lithium Tetrafluoroborate	3.2	EC/DMC 1:2	[**22**]
	$LiB_2(C_2O_4)_2$	Lithium bis(oxalato)borate	4.4	PC/EC/EMC 1:1:1	[**24**]
	$LiBF_2B(C_2O_4)_2$	Lithium difluoro(oxalato)borate	4.0	PC/EC/EMC 1:1:1	[**24**]

Imide	$Li(NSFO)_2$	Lithium bis(fluorosulfonyl)imide	8.0	PC	[**25**]
	$Li(NSCF_3O)_2$	Lithium Bis(Trifluoromethanesulfonyl)Imide	14.2	PC	[**25**]

Although lithium arsenate and perchlorate have conductivities higher than all the other salts, their use is limited by the high toxicity for humans and the risk of explosion. Electrolytes comprising imide salts and carbonate-based solvents show promising conductivity, but their application is limited by the occasional corrosion of current collectors. So far imide salts will be safely used only in combination with Ionic Liquids (ILs) as solvents. However ILs are an emerging solution for Li-ion cells. Presently, they have not been extensively used because of their high industrialization costs. For these reasons they have been neglected in this work, because it aims at identifying a benchmark for the present Li-ion technology.

$LiPF_6$ offers a good conductivity, acceptable toxicity. Safety limitations concern thermal and chemical stability. In particular, the thermal decomposition onset is close to the battery operative condition [**26**] and in presence of water the salt spontaneously hydrolyses, releasing toxic gasses such as HF.

$LiBF_4$ and $LiB_2(C_2O_4)_2$ are not moisture-sensitive and more thermally stable then $LiPF_6$. Presently their lower conductivity is a severe limitation for LiBs application.

Among all the electrolytes, $LiPF_6$-DMC/$EC_{1:1vol}$ based electrolytes show SEI layers, characterised by good conductivity and high mechanical resistance. For these reasons $LiPF_6$-DMC/$EC_{1:1vol}$ based electrolyte are used in almost all Li-ion cells.

Based on the review here briefly summarized, **LiC_6/$LiPF_6$-DMC:$EC_{1:1vol}$/$LiCoO_2$** cell configuration has been assumed as a reference for the experimental work.

1.2. Li-ion cell side chemistry

In order to have a survey of the side-reaction mechanisms and to understand the most prominent gaseous by-products generated into Libs, literature has been reviewed identifying several side reactions. Side processes have been reported below according to the class of electrolyte implemented in to Li-ion cells.

Cyclic carbonates:

EC and PC are known to be reduced on carbonaceous anodes to ethylene and propylene, respectively, and lithium carbonate via a two-electron process.

$Li^+ + PC(orEC) + e^- \rightarrow Li+[PC]^{\bullet -} + Li^+ + e^- \rightarrow CH_2CHR + Li_2CO_3$

The reductive decomposition of EC via a one-electron process is responsible for the formation of lithium semicarbonate which is one of the key components of the SEI [**27**].

$2Li^+ + 2PC\ (orEC) + e^- \rightarrow 2Li^+[PC]^{\bullet -} \rightarrow 2Li^+[CO_2(OCH_2R1)]^{\bullet -} + [semicarbonate]^+$

The above mechanism is driven by the stabilization of the intermediate radical anion due to conjugation and by the release of the neutral ethylene species. The semicarbonates may undergo further reactions to release CO_2. The lithium alkoxides, generated by reduction, attack further the carbonate solvents boosting up the polymerization process [28]. In normal cell operation, CO2 evolution may be also enhanced by water impurities.

$(CH_2OCO2Li)_2 + H_2O \rightarrow Li_2CO_3 + 2CH_2OH + \mathbf{CO_2}$

Neglecting CO_2, other gases such as CO and trace of O_2 may be generated. H_2 evolution may occur due to reduction of trace of water. Hydrocarbon gases are also generated during the formation process and typically they are CH_4, C_2H_2, C_2H_4, C_2H_6, C_3H_6 and C_3H_8. C_3H_6 is not detected in the EC/DMC electrolyte [**29**].

Linear carbonates

A list of possible reactions of reductive degradation of DMC and DEC is reported below:

$EC + 2Li^+ + 2e^- \rightarrow CH_3CH_2OLi\downarrow + CO\uparrow$

$CH_3OCO_2Li + e- + Li+ \rightarrow Li_2CO_3\downarrow + CH_3\bullet$

$CH_3\bullet + CH_3\bullet \rightarrow C_2H_6\uparrow$

$CH_3\bullet + ½\ H_2 \rightarrow CH_4\uparrow$

$DMC + 2Li^+ + 2e^- \rightarrow CH_3OLi\downarrow + CO\uparrow$

$DEC + 2Li+ + 2e- + H_2 \rightarrow Li_2CO_3\downarrow + 2C_2H_6\uparrow$

$DEC + 2Li^+ + 2e^- + H_2 \rightarrow CH_3CH_2CO_2OLi\downarrow + C_2H_6\uparrow$

$C_2H_5OCO_2Li + e^- + Li^+ \rightarrow Li_2CO_3\uparrow + C_2H_5^{\bullet}$

$C_2H_5^{\bullet} + ½\ H_2 \rightarrow C_2H_6\uparrow$

$C_2H_5^{\bullet} + CH_3^{\bullet} \rightarrow C_3H_8\uparrow$

CH_4, C_2H_6, C_3H_6, and C_3H_8 are produced from the reduction of DEC and radical derivatives on the surface of anode. CO_2 gas can also be generated in two different processes. One is the oxidation reaction of DEC (or DMC) with the O_2 present in the battery, and the other is the reaction of the $ROCO_2Li$ with trace of H_2O and HF:

$DEC + 6O_2 \rightarrow \mathbf{5CO_2} + 5H_2O$

$DMC + 4O_2 \rightarrow \mathbf{3CO_2} + 5H_2O$

$C_2H_5OCO_2Li + HF \rightarrow LiF + C_2H_5OH + \mathbf{CO_2}$

$2C_2H_5OCO_2Li + H_2O \rightarrow Li_2CO_3 + 2C_2H_5OH + \mathbf{2CO_2}$

The results reported above are independent from the cathode materials [**30**]. During accelerated aging, the gas volumes increase especially due to the CO_2 and CO content, which is proportional to the aging temperature. However, the CO_2 evolution in each cycle shows a much slower process and it approaches to an equilibrium [**29**]. The decay in CO_2 evolution may be explained by the formation of an (imperfect) SEI layer, which reduces the rate of the CO_2 formation reaction but does not inhibit it completely:

$2CO_2 + 2e^- + 2\,Li^+ \rightarrow Li_2CO_3 + \mathbf{CO_2}$

$ROCO_2Li + H_2O \rightarrow 2ROH + \mathbf{CO_2} + Li_2CO_3$

Decomposition of EC and DEC in presence of LiPF6.

The ring-opening reaction of EC is favoured in presence of $LiPF_6$ and its reactivity is much higher than linear carbonates, particularly at low temperatures [**31**].

Hexafluorophosphate (PF_6^-) salts can produce PF_5 gas, a strong Lewis acid which can react with the solvent, see Figure ii-3. Ring-opening polymerization of EC is driven by the evolution of CO_2, under mild acidic conditions. Continued reaction produces polyethylene oxide (PEO), and oligo-ether carbonates. Both oligopolymers can further react with PF_5 leading to CO_2 evolution. In conclusion, CO_2 is the main gaseous product from heated electrolyte solutions. Moreover, CO_2 could be reduced at the anode to yield oxalate, formate and CO. Both oxalate and formate can be re-oxidized at the cathode to CO_2 to give a reversible self-discharge mechanism.

Initiation of the EC degradation cascade may also occur with protic impurities. Phosphorus oxyflouride (OPF_3) is generated by the reaction of $LiPF_6/PF_5$ with such impurities. OPF_3 reacts with the EC to produce CO_2 and $OPF_2OCH_2CH_2F$, or inserting ethylene-oxide units into the P–O bond. Both pathways involves CO_2 generation [**32**].The phosphorus oxyflouride (OPF_3) reacts with DEC also, to generate $OPF_2OC_2H_5$ along with CO_2 and C_2H_5F. Decomposition mechanisms for mixtures of EC/DMC and EC/DEC/DMC are similar to those here shown for the single components EC and DEC. DMC gives rise to fewer side reactions compared to DEC. Finally, the products of the chemical degradation of the solvent components of the electrolyte may also react with $LiPF_6/PF_5$.

Lithium alkyl carbonates for example give rise to the formation of phosphate entities usually found in the SEI composition.

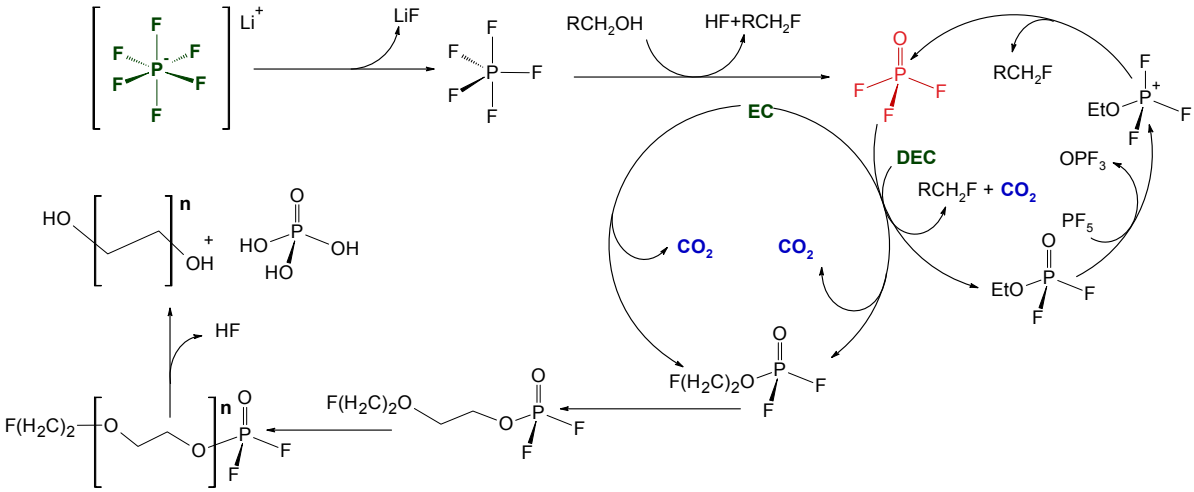

Figure ii-3 scheme of $LiPF_6$ based decomposition

Summarizing, among all gaseous side products the most important are H_2, CH_4, H_2O, and CO_2. However, CO_2 has the unique property to be the endpoint of the first side-reactions and the starting point of secondary side reactions. Thus, the capture of CO_2 could prevent overpressure, and could increase the battery lifetime. For these reasons, the work has been focused on CO_2 evolution in Li-ion cells.

1.3. A short review about Li-ion cell analysis

In the frame of well-known analytical science, Liquid-Chromatography–Tandem-Mass-Spectrometry (LC/MS) or Ionic Chromatography (IC) are used to identify side products in battery cells liquid phase, whereas Gas-Chromatography/Thermocondutivity (GC/TCD) or Gas-Chromatography-Tandem-Mass-Spectrometry (GC/MS) are used to reveal the evolved gas species [**33**]. These analytical methods are conventionally aimed at revealing side products, in order to identify the decomposition pathway.

In particular Britta Vortmann and co-worker [**34**] used LC/MS to reveal side products originated from the decomposition of $LiPF_6$ based electrolyte at the end of the battery operation. On the contrary, Steven E. Sloop et al. used GC/TCD to investigate the role of the electrolyte reactivity in performance decline and self-discharge of Li-ion cells [**33**]. Unlike these scientific works, other research groups have focused their attention on the thermal stability of electrolyte. In particular, Philip N. Ross and co-workers used TGA/FTIR

thermal analysis demonstrated that molten $LiPF_6$ display higher thermal stability compared to the corresponding organic based electrolyte [**26**].

Although all these examples represent good approaches for the investigation of side chemistry of LiBs, they are unsuitable to monitor the evolution of side products. In particular, such kind of analysis required minimum gaseous or liquid aliquots, which are comparable to the amount of the electrolyte present in the operating cell. Thus, one has to conclude that sampling procedure promotes irreversible alteration in the inner chemistry of the cell. In other words, sampling induces the whole equilibria towards the replacement of the subtracted species (Le Chatelier Principle).

Other methods, such as residual gas analysis, would not induce such perturbations involving a single measurement at the end of device operation. Although these approaches give extremely precise quantitative information, they require opening the device and they cannot give additional information such as the side reactions time evolution. For all these reasons non-perturbative analytical protocol aimed at revealing gaseous side products should be optimised and validated.

Excluding chromatography and mass spectrometry, the only way to reveal this kind of substances is an analytical approach based on spectroscopy. The methods of choice to reveals these kind of analytes are Raman and FTIR spectroscopies. Raman spectroscopy is aimed at revealing any kind of molecule. Unfortunately, its sensitivity is theoretically unsuitable to reveal gaseous side products within a Li-ion cell, because the relative abundance of each side product is close to limit of detection of this kind of apparatus. On the contrary, the FTIR detection system is more performing than Raman spectroscope. Unlike Raman, FTIR applicability domain is limited to analytes characterised by permanent dipolar moments. However, considering the relevance of CO_2 in the inner chemistry of Li-ion cells, FTIR spectroscopy will be able to provide qualitative and quantitative information. Thus, FTIR has been assumed as the method of choice for the aim of this project.

For the analytical purpose here described a Li-ion cell must be designed and validated, in order to have a cell model suitable for in situ detection of CO_2.

The next paragraphs will describe the rationale and the theoretical aspects of the techniques used in this project. Then will be presented the test protocol followed to validate all of the analytical methods. At the end, the result of the spectro-electrochemical analysis will be presented revealing the conditions under which CO_2 pressurised the cell.

1.4. References

1. K. Xu Encyclopedia of Elelctrochemical Power Sources, Elsevier, 2012
2. J. G. Thevenin and R. H. Muller J. Electrochem. Soc. (1987), 134, 2, pp.273-280
3. Claus Daniel, Jürgen O. Besenhard Handbook of Battery Materials, Second Edition Wiley-VCH (2011)
4. C. Dyer, p. Moseley, Z. Ogumi, D. Rand, B. Scrosati. (2009) Enc. of Elect. Pow. Sources, vol.1, 223.
5. Kim, J., Noh, M., Cho, J., and Kim, H.(2005) J. Electrochem. Soc., 152, A1142.
6. Kanno, R., Kubo, H., Kawamoto, Y., Kamiyama, T., Izumi, F., and Takano, Y. (1998) J. Solid State Chem., 140, 145.
7. Rossouw, M.H. and Thackeray, M.M.(1991) Mater. Res. Bull., 26, 463.
8. Im, D. and Manthiram, A. (2002) J. Electrochem. Soc., 149, A1001.
9. Jisuk Kim,a Youngsik Hong,b,d Kwang Sun Ryu,b, Min Gyu Kim,c and Jaephil Choa,*,zElectrochemical and Solid-State Letters, 9 (1), A19-A23 (2006)
10. Wang, Q.Y., Liu, J., Vadivel Murugan,A., and Manthiram, A. (2009) J. Mater.Chem., 19, 4965.
11. Scrosati, B. (2000) Electrochim. Acta, 45,2461.
12. Kim, J.H., Myung, S.T., Yoon, C.S., Oh, I.H., and Suna, Y.K. (2004) J. Electrochem. Soc., 151, A1911.
13. Huang, H., Yin, S.-C., and Nazar, L.F.(2001) Electrochem. Solid State Lett., 4,A170
14. Fisher, J.E. (1987) in Chemical Physics of Intercalation, NATO ASI Series, Vol. B172 (eds A.P. Legrand and S. Flandrois), Plenum Press, New York, p. 59.
15. Kanno, R., Takeda, Y., Ichikawa, T.,Nakanishi, K., and Yamamoto, O.(1989) J. Power Sources, 26, 535.
16. Way, B.M. and Dahn, J.R. (1994) J.Electrochem. Soc., 141, 907.
17. Besenhard, J.O. and Winter, M. J. Power Sources, 54, 228
18. in Ulmer Elektrochemische Tage, Ladungsspeicherung in der Doppelschicht, (1995) , vol. 2 (ed. W. Schmickler), Universit¨atsverlag Ulm, p. 47.
19. Reddy, T. and Hossain, S. (2002) in Handbook of Batteries, 3rd edn, Chapter 34 (eds D.E. Linden and T.B. Reddy),McGraw-Hill, New York, pp. 1–62.
20. L. Li, X. Liu, S.Wang, W. Zhao. Sustainable Chem. Eng.2014, 2, 1857−1863
21. H. Zhao, S.J. Park, F.Shi, Y. Fu, V. Battaglia, P. N. Ross Jr. G. Liu J. Electrochem. Soc. 2014 volume 161, issue 1, A194-A200
22. Zhang, S.S. (2007) ECS Trans., 3, 59.

23. Han, H.-B, Zhou, S.-S., Zhang, D.-J., Feng, S.-W, Li, L.-F. Liu, K., Feng, W.-F., Nie, J., Li, H., Huang, X.J.,Armand, M., and Zhou, Z.-B. (2011) J. Power Sources, 196, 3623.
24. Xu et al. Electrochem. Solid-State Lett. 6 (2003) A144
25. Gireaud et al. J. Electrochem. Soc. (2005) A850
26. H. Yang, G. V. Zhuang, P. N. Ross Journal of Power Sources 161 (2006) 573–579
27. Shin et al. Journal of Power Sources 109 (2002) 47
28. Kong et al. Journal of Power Sources 142 (2005) 285
29. Abraham et al. Journal of Power Sources 119–121 (2003) 511
30. Vetter et al. J. Power Sources 159 (2006) 277; Arora et al., J. Electrochem. Soc. 145 (1998) 3647
31. L. Terborg, S. Nowak, S. Passerini, M. Winter, U. Karst, P. R. Haddad, P. N. Nesterenko Analytica Chimica Acta 714 (2012) 121– 126
32. P. Kendra, A. Vazquez, Nancy d. Epsky, and Robert R. Heath Environ. Entomol. 34(3): 569-575 (2005)
33. S.teven E. Sloop, John B. Kerr, K.Kinoshita Journal of Power Sources 119–121 (2003) 330–337
34. B. Vortmann, S. Nowak, C. Engelhard Anal. Chem. 2013, 85, 3433−3438

Chapter 2

Theoretical aspects of the analytical methods

2.1. Abstract

This paragraph describes the most prominent aspects of the analytical techniques used for the experimental work. The analytical rationale of all methods has been commented in details, explaining the results that all techniques can provide.
The analytical methods here described are Fourier Transform InfraRed spectroscopy (FTIR), Electrochemical Impedance Spectroscopy (EIS) and Galvanostatic Cycling with Potential Limitations (GCPL).

2.2. Introduction to FTIR technique

Fourier Transform Infrared Spectroscopy (FTIR) is an analytical technique, which provides qualitative information about functional groups within molecules. This kind of spectroscopy is widely used in food and drug industries, in order to identify the presence of specific contaminants.
Despite this conventional application, in the past it had been extensively used to quantify the analytes in gas phase. However, the utilization of FTIR detectors is limited to molecules characterised by permanent dipolar moments.
The advent of mass spectrometry in analytical science had led to replace FTIR gas detector with mass spectrometer (MS) [1]. The technological success of MS detector is due to their superior sensitivity and a wider applicability domain. Contrary to FTIR, mass spectrometers are theoretically able to reveal any kind of substances, and thus MS technology extended the potentiality of analytical science in gas phase analysis.
Despite its inferior analytical performances, FTIR spectroscopes is still offering specific advantages which make it non replaceable in specific analytical tasks. One example of a practical failure of MS analysis is ion suppression [2]. This phenomenon occurs into MS-detectors by analysing samples characterised by strong acid/base properties. In these conditions, anionic and cationic adducts are generated in the ion source, generating neutral species, which could not be revealed by the mass spectrometer [2].
In conclusion, MS-detectors should not be considered as the instruments of choice for analytical investigations in the case of batteries, where ion suppression could be critical [2]. Thanks to a lesser susceptibility to matrix effects, FTIR instrumentations offered more reproducible analytical responses. In the specific case of gas phase analysis, FTIR should be considered as an alternative technique to mass spectrometry.

2.3. Theoretical and practical aspects of FTIR

The rationale of FTIR spectroscopy is based on the interaction between molecules and electromagnetic waves. In particular, light absorbance determines transitions between rotational and vibrational states of the molecules. In order to stimulate these transitions, the photons should have specific energies (12eV-1.7eV). Thus the light sources implemented in this kind of instruments should have a spectral emission, which ranges from 4000 cm^{-1} to 400 cm^{-1}.

In the past, dispersive instrumentations have been extensively used. However, light dispersive apparatus required careful tuning and involved long scan time to achieved acceptable sensitivity. Interferometer based technology has overcome these limitations, increasing sensitivity and reducing scan time [3].

The main output of interferometers is the interferogram, which is a system of signals defined in the frequency domain. Interferogram could be easily converted into a common spectrum by performing the Fourier transform.

The core of the FTIR spectroscope is the interferometer system and in principle it determines the performances of these instrumentations. Figure 2-1 describes the typical hardware setup of a FTIR spectroscope.

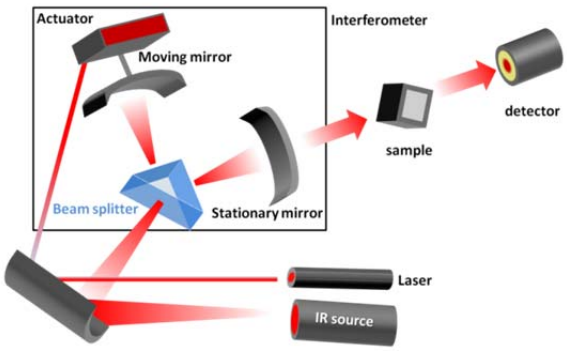

Figure 2-1 Scheme of a FTIR instrument

The Interferometer within FTIR employs a beam splitter which takes the incoming infrared ray and divides it in two optical beams. The first beam reflects on a stationary mirror, whereas the second beam reflects off a moving mirror. A laser controlled actuator allows moving the mirror along very short distance (typically a few millimetres) away from the beam splitter. The actuator movements are controlled by measuring the laser interference on the moving mirror. The two beams reflect off of their mirrors and recombine when they meet back at the beam splitter.

Taking into account that the rays have different optical paths and one of them is changing by moving the position of its mirror, the signal which exits the interferometer is the summation of several frequencies. This outcome signal is called interferogram, which has the unique property that every data point (a function of the moving mirror position) has information about every infrared frequency which comes from the source, [3].

2.4. The practical case of CO_2

Molecules can absorb infrared light by changing either vibrational or rotational states. In order to absorb infrared light it is necessary for the molecule to have a dipolar momentum greater than zero. For this reasons, also apolar polyatomic molecules can absorb infrared light under the condition of the presence of a local dipolar states.

Whenever molecules absorb infrared light, roto-vibrational transitions might occur. Molecules in their upper vibrational level ($\Delta v=+1$), could preserve their rotational state ($\Delta J=0$). Otherwise they can be either promoted or demoted to next or previous rotational state ($\Delta J=\pm 1$). Under these quantum mechanics assumptions, three branches can be theoretically observed. A FTIR spectrum acquired with high resolution can show roto-vibrational branches. These branches are called:

P-branch if $\Delta J=-1$

Q-branch if $\Delta J=0$

R-branch if $\Delta J=+1$

A representation of these transitions has been sketched in Figure 2-2.

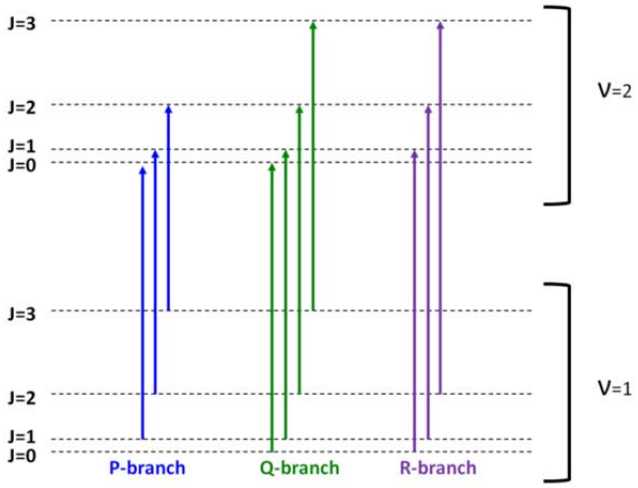

Figure 2-2 Rotovibrational transitions

For each variation of molecular vibrational state (Δv) it is possible to observe transitions from each of the accessible rotational levels. Thus, if pure rotovibrational transitions were observed, one could find narrow peaks corresponding to each transition involved. However, when instrumental resolution is insufficient, the spectrum revealed convolved bands, as occurred in the case of CO_2. Moreover, in the mid infrared region it is quite common to have specific selection rules, which forbid some rotovibrational transition [3]. For example, CO_2 shows the suppression of the Q*branch at 2360cm^{-1}.

A FTIR spectrum of CO_2 has been reported in Figure 2-3. By looking at the plot, one can notice two systems of signals in the far and mid infrared regions. The pattern in the far infrared region (680-650 cm^{-1}) consists of three branches and it is attributed to bending vibrational mode. On the contrary, in the mid infrared region (2340-2360cm^{-1}) the pattern reveals only P and R branches. These signals have been attributed to stretching vibrational mode.

All of the optical components cut off frequencies below 1000 cm^{-1}, making it difficult to observe the bending transition. Although bending signals are more intense than stretching peaks, they are practically unsuitable. Thus CO_2 is preferentially investigated in the mid infrared region, neglecting the bending signals.

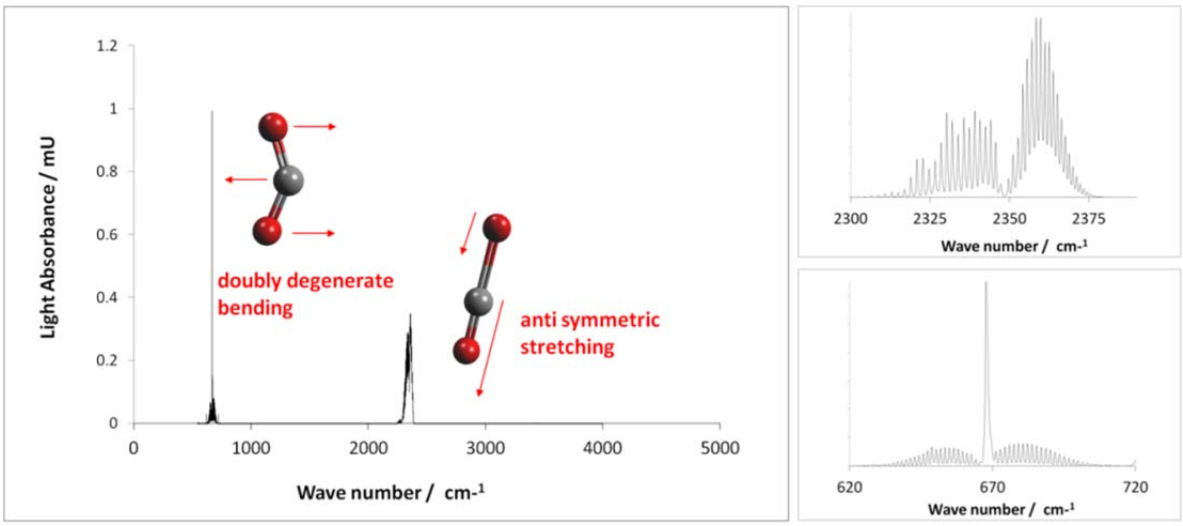

Figure 2-3 spectrum of CO_2

It is also important to consider that such kind of spectra could be observed only in the case of monoisotopic composition such as $^{12}C^{16}O$. On the contrary, CO_2 in the gaseous form is a mixture of several isotopic compositions. Thus, different bands depending on the isotopic composition will be revealed by analysing atmospheric CO_2.

According to the model of the harmonic oscillator (**eq1**), the atomic weights influence the energy of the vibrational states and thus isotopes could induce shoulder or peaks convolution.

$$\mathbf{v} = \frac{\mathbf{1}}{\mathbf{2\pi c}}\sqrt{\frac{\mathbf{k}}{\mu}} \xrightarrow{\text{with}} \boldsymbol{\mu} = \frac{\mathbf{Mo \cdot Mc}}{\mathbf{Mo + Mc}} \qquad \textbf{eq1}$$

Where ν is the vibrational state, **c** represents the speed of light, **k** is the elastic constant that bring together atoms "O" and "C", whereas **μ** is the reduced mass that characterises the harmonic oscillator.

Figure 2-4 shows a threshold at the base of the stretching peak of the $^{12}CO_2$. This convolved peak is due to ^{13}C atoms.

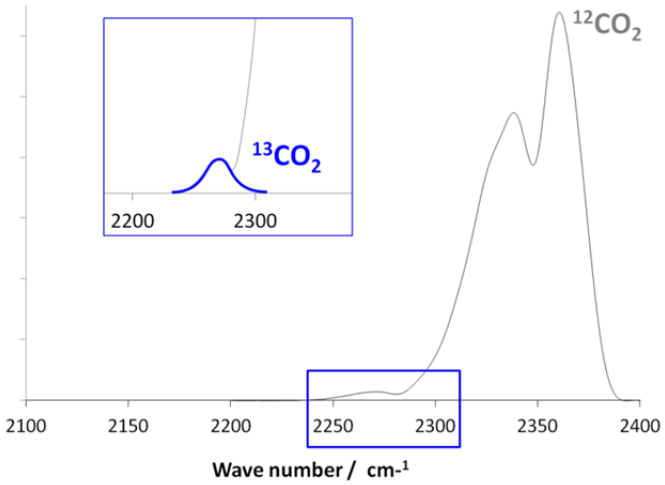

Figure 2-4 threshold due to ^{13}C atoms

.

2.5. Analytical rationale of FTIR-quantification

as quantitative analysis, FTIR technique might be used in absorbance optical mode, according to Lambert-Beer law (**eq2**)

$$\mathbf{A} = -\log(\mathbf{T}) = -\log\left(\frac{\textbf{incoming photons}}{\textbf{outcoming photons}}\right) = \boldsymbol{\varepsilon} \cdot \mathbf{c} \cdot \mathbf{l} \qquad \textbf{eq2}$$

Where **A** is the amount of light absorbed, **Ɛ** represents the molar extinctions, **C** is the concentration, **l** is the length of optical path followed by IR-photons.

This means that absorbance and concentration should have a linear dependence, whenever the electronic of the FTIR apparatus gives a constant response. Thus, it is possible to build up a quantification method by performing calibration. This kind of experiment consists of absorbance measurements, which are usually performed at constant wave number and by changing the concentrations of the substance of interest. According to the equation of ideal

gases, the concentration (**C**) could be replaced by pressure (**P**) under the restriction of isothermal conditions [3].

Considering that a linear dependence between **A** and **P** occurred at each absorption edge, it is possible to evaluate the absorption ratio due to a couple of near absorption peaks. This approach makes it possible to control whether interfering species are contributing to light absorbance leading to wrong analytical evaluations. In other words, signals which are not useful in term of quantification can be used as internal reference.

In the case of CO_2, the wavelength selected for the calibration is the maximum of the highest absorption band for the asymmetric stretching of CO_2 (around 2360 cm^{-1}). The second maximum (2340 cm^{-1}) is used as reference.

2.6. Introduction to EIS technique

Electrochemical impedance spectroscopy (EIS) is a technique based on the measurement of the impedance expressed by a complex system, when an AC voltage is imposed to it with a sweep of frequency.

The impedance is an electrical parameter, defined as the opposition that a circuit presents when a voltage is applied to it. Generally speaking, impedance should be considered as an extension of resistance to an AC circuit and therefore its current exhibits both magnitude attenuation and phase shift, unlike DC resistance which only shows magnitude attenuation. Working with an AC circuit, two impeding mechanisms should be considered. The first mechanism is the dissipative process due to resistances and the second one is the energy storage process due to self-capacitances (and/or self-inductances). The different nature of these mechanisms induces different effects on the current. Resistances reduce the amplitude of current, but they do not perturb the phase. Capacitances (or inductances) induce phase shifts but they do not change the amplitude of the current.

Starting from the formalism expressed by the first Ohm law (**eq1**), which describes the resistance in a DC circuit, it is possible to obtain a similar expression (**eq2**) for the impedance in an AC circuit, describing potential and current as complex sinusoidal functions in the form "$y=|A|e^{ix}$":

$$\mathbf{R} = \frac{\mathbf{V}}{\mathbf{I}} \qquad \textbf{eq1}$$

$$\vec{\mathbf{Z}} = |\mathbf{Z}|\frac{|\mathbf{V}|\mathbf{e}^{\mathbf{i}(\omega\mathbf{t}+\boldsymbol{\varphi}^{\mathbf{V}})}}{|\mathbf{I}|\mathbf{e}^{\mathbf{i}(\omega\mathbf{t}+\boldsymbol{\varphi}^{\mathbf{i}})}} = |\mathbf{Z}|\frac{|\mathbf{V}|}{|\mathbf{I}|}\mathbf{e}^{\mathbf{i}(\omega\mathbf{t}-\omega\mathbf{t})}\mathbf{e}^{\mathbf{i}(\boldsymbol{\varphi}^{\mathbf{V}}-\boldsymbol{\varphi}^{\mathbf{i}})} \xrightarrow{\boldsymbol{\varphi}^{\mathbf{V}}-\boldsymbol{\varphi}^{\mathbf{i}}=\boldsymbol{\varphi}^{\boldsymbol{\theta}}} |\mathbf{Z}|\frac{|\mathbf{V}|}{|\mathbf{I}|}\mathbf{e}^{\mathbf{i}(\boldsymbol{\theta})} \qquad \textbf{eq2}$$

In **eq1 R** is the resistance, **V** represents the potential and **I** is the current. Whereas in **eq2**, **j** is the imaginary unit, ω represents the pulsation, φ_v and φ_i are the phase constants of potential and current respectively, **t** represents the time and θ is the phase shift between potential and current.

The exponential function could be easily converted into a more familiar trigonometric formalism by using Euler's formula, **eq3**, which makes it possible to represent impedance as a vector defined into the complex plane, also called Nyquist plot (or Cole-Cole plot):

$$\mathbf{e^{ix} = cos(x) + isin(x)} \qquad \textbf{Euler's formula}$$

$$\vec{\mathbf{Z}} = |\mathbf{Z}|\mathbf{e^{i\theta}} = |\mathbf{Z}|[\mathbf{cos(\theta) + isin(\theta)}] \qquad \textbf{eq3}$$

2.7. Analytical rationale of EIS

When the current flows through the circuit it is not possible to distinguish the impedance due to each component. However, by applying a sweep of pulsation (also called angular frequency), it is possible to measure separately the impedance due to each component at a specific frequency. The rationale could be easily understood considering that each component responds within a specific frequency domain. . However, impedance itself is not a direct measure of capacitances (or inductances) and resistances. To do so, it is mandatory to interpolate the experimental data set with a proper mathematical model (equivalent circuit), which makes it possible to calculate capacitances and resistances.

This short review describes the behaviour of each element and it explains a method to configure them leading to a proper mathematical description of systems.

2.8. Circuit elements

Resistor:

For a pure resistor, V and I are not affected by pulsation because the phase shift is null and therefore the "$e^{i\omega t}$" parameters could be elided, obtaining an expression similar to the first Ohm's law.

$$\vec{\boldsymbol{Z}} = |\boldsymbol{Z}|\frac{|\boldsymbol{V}|\boldsymbol{e}^{\boldsymbol{i}(\boldsymbol{\omega t}+\boldsymbol{\varphi}^{\boldsymbol{v}})}}{|\boldsymbol{I}|\boldsymbol{e}^{\boldsymbol{i}(\boldsymbol{\omega t}+\boldsymbol{\varphi}^{\boldsymbol{i}})}} = |\boldsymbol{Z}|\frac{|\boldsymbol{V}|}{|\boldsymbol{I}|}\boldsymbol{e}^{\boldsymbol{i}(\boldsymbol{\omega t}-\boldsymbol{\omega t})}\boldsymbol{e}^{\boldsymbol{i}(\boldsymbol{\varphi}^{\boldsymbol{v}}-\boldsymbol{\varphi}^{\boldsymbol{i}})} \xrightarrow{\boldsymbol{\varphi}^{\boldsymbol{v}}-\boldsymbol{\varphi}^{\boldsymbol{i}}=\mathbf{0}} |\boldsymbol{Z}|\frac{|\boldsymbol{V}|}{|\boldsymbol{I}|}\mathbf{1} = \sim\boldsymbol{R} \qquad \textbf{eq4}$$

Capacitor:

For a pure capacitor the impedance is proportional to the reciprocal value of the pulsation. **Eq5** shows that the current flowing through a capacitor is defined as the electrical capacitance (**C**) times the partial derivative of potential, calculated in the time domain. The potential can be expressed with the formalism expressed by **eq6**. **Eq7** is a trigonometric expression of impedance and it could be obtained by substituting the **eq6** into **eq5**. By expressing **eq7** in polar form and generalising it with the Euler's formula **eq8** a simply expression for the impedance of a capacitor is achieved, **eq9**.

$$\mathbf{I(t) = C\frac{\partial}{\partial t}V(t)} \qquad \textbf{eq5}$$

$$\mathbf{V(t) = Vsin(\omega t)} \qquad \textbf{eq6}$$

$$\overrightarrow{\mathbf{Zc}} = \frac{\mathbf{V(t)}}{\mathbf{I(t)}} = \frac{\mathbf{Vsin(\omega t)}}{\mathbf{C\omega Vcos(\omega t)}} = \frac{\mathbf{sin(\omega t)}}{\mathbf{C\omega \cdot sin\left(\omega t + \frac{\pi}{2}\right)}} \qquad \textbf{eq7}$$

$$\overrightarrow{\mathbf{Z_L}} = \frac{\mathbf{V(t)}}{\mathbf{I(t)}} = \frac{\mathbf{1}}{\mathbf{\omega C}}\frac{\mathbf{e^{i\omega t} - e^{-i\omega t}}}{\mathbf{2i}} \cdot \frac{\mathbf{2i}}{\mathbf{e^{i\omega t + \frac{\pi}{2}} - e^{-i\omega t + \frac{\pi}{2}}}} == \frac{\mathbf{1}}{\mathbf{\omega C}}\frac{\mathbf{e^{i\omega t} - e^{-i\omega t}}}{\mathbf{e^{i\omega t + \frac{\pi}{2}} - e^{-i\omega t + \frac{\pi}{2}}}} =$$

$$= \frac{\mathbf{1}}{\mathbf{\omega C}}\mathbf{e^{-i\frac{\pi}{2}}} \cdot \frac{\mathbf{e^{i\omega t} - e^{-i\omega t}}}{\mathbf{e^{i\omega t} - e^{-i\omega t}}} = \frac{\mathbf{1}}{\mathbf{\omega C}}\mathbf{e^{-i\frac{\pi}{2}}} \qquad \textbf{eq8}$$

$$\overrightarrow{\mathbf{Zc}} = \frac{\mathbf{1}}{\mathbf{\omega C}}\mathbf{e^{-i\frac{\pi}{2}}} = \frac{\mathbf{1}}{\mathbf{\omega C}}\left[\mathbf{\cos\frac{\pi}{2} - i\sin\frac{\pi}{2}}\right] = \mathbf{-i\frac{1}{\omega C}} \qquad \textbf{eq9}$$

The formalism expressed in **eq.9** reveals that both capacitors should be considered as energy storage elements, because the current changes its phase but keeps its amplitude, leading to a constancy in the energy of the circuit. On the contrary, the amplitude attenuation observed within a resistor is representative of the energy lost by electron scattering, which macroscopically results from circuit heating.

Constant phase element:

Whenever an electrode is immersed into an electrolyte, an interface is generated in the contact region. The interface is a perturbed region of the electrolyte which has specific physico-chemical properties. According to the Gouy-Chapman model [**Errore. L'origine riferimento non è stata trovata.**], the interface is considered a region of the system, wherein the selective accumulation of ions determines a macroscopic polarization (separation of charge at interface).

The interface is able to promote charge separation, but it loses some energy, because the ions' thermal motion opposes to the accumulation of charge. Thus, the interface is a non- ideal capacitor.

In order to have a better mathematical description of interfaces, **Eq9** could be generalized as reported in **eq10**. By comparing **eq9** and **eq10** one can notice the presence of **α** and **Q** parameters, which respectively represent the degree of ideality and the pseudo-capacitance of interface.

$$\mathbf{Z_Q = -i\frac{1}{Q\omega^{\alpha}}} \qquad \textbf{eq10}$$

Warburg element:

In a chemically reacting system under diffusion control, the rate determining step is the reagent uptake at the reaction site. An electrochemical system under diffusion control, which works with a supporting electrolyte, exhibits a current flow proportional to the diffusion flow (**Eq11**), as expected from the first **Fick's law**:

$$J = D\frac{\partial C}{\partial x}$$

Where **J** is the diffusional flow, **D** is the coefficient of diffusion and $\frac{\partial C}{\partial x}$ is the concentration gradient.

$$\mathbf{\Delta I = nFAJ \xrightarrow{J=D\frac{\partial C}{\partial x}} nFAD\frac{\partial C}{\partial x} \approx nFA2\sqrt{DT} = nFA2\sqrt{D\omega}} \qquad \textbf{eq11}$$

Where **n** is the number of exchanged electrons, **F** is the Faraday constant and **A** is the specific surface of the electrode. In the simple case of a single species under one dimensional diffusion control, the $D\frac{\partial C}{\partial x}$ formalism could be reduced to $\mathbf{2\sqrt{D\omega}}$, where $\sqrt{D\omega}$ (diffusion length) represents how far the concentration gradient propagates in the bulk region.

On the other hand, the potential could be generalised by the Nerst formalism reported in **eq12a** and **eq12b** [4]

$$\mathbf{\Delta E = \frac{R_g T}{nF}\ln\left(\frac{a_{ox}}{a_{red}}\right) \sim \Delta E = \frac{R_g T}{nF}\ln\left[\frac{\Delta C_{ox}}{C_{ox}} + 1\right]}; \qquad \textbf{eq12a}$$

$\mathbf{if\ \frac{\Delta C}{C_{ox}} = x\ and\ \lim_{x\to 1}[\ln(x+1)] = x}$; Assumption of weak potential stimulation

$$\mathbf{then\ \Delta E = \frac{R_g T}{nF}\left(\frac{\Delta C}{Co}\right)} \qquad \textbf{eq12b}$$

Where $\mathbf{R_g}$ is the gas constant, **T** is the temperature, **n** is the number of exchanged electrons, **F** is the Faraday constant, $\mathbf{a_{ox}}$ and $\mathbf{a_{red}}$ represent respectively the activity of the oxidant and reductive species, whereas C_{ox} and ΔC_{ox} are the concentration of oxidant and its variation. Assuming relative low concentration activity could be substituted with concentration. In the case of small variation of the concentration ($\Delta C \ll Co$) due to weak potential stimulation ($\Delta E \leq$ 10mV), an expression for "diffusional impedance" is achieved by dividing potential for current, **eq13-a**.

$$|\mathbf{Z_w}| = \frac{\mathbf{\Delta E}}{\mathbf{\Delta I}} = \frac{\frac{\mathbf{R_g T}}{\mathbf{nF}}\left(\frac{\mathbf{\Delta C}}{\mathbf{Co}}\right)}{\mathbf{nFA2}\sqrt{\mathbf{D\omega}}} \xrightarrow{\Delta C \ll Co} \frac{\mathbf{R_g T}}{\mathbf{n^2 F^2 A2}\sqrt{\mathbf{D\omega}}} = \mathbf{W}\sqrt{\boldsymbol{\omega}} \; ; \qquad \textbf{eq13a}$$

Generalising impedance with phasors, it is possible to develop a suitable descriptor (**W**) for diffusion phenomena, that is the Warburg element **eq13b** [5]**.**

$$\overrightarrow{\mathbf{Z_w}} = \mathbf{W}\sqrt{\boldsymbol{\omega}} + \mathbf{iW}\sqrt{\boldsymbol{\omega}} \qquad \textbf{eq13b}$$

Warburg element for rough electrode:

In the chemical scenario previously described, electrodes have been considered as flat and smooth surfaces. However, in real conditions electrodes present defects and pores. As reported in literature [66], the impedance due to charge motion through pores is described for example by **eq14**.

$$\mathbf{M_p} = \mathbf{R_p}\frac{\coth\sqrt{\mathbf{j\omega}/\mathbf{D}}}{\sqrt{\mathbf{j\omega}/\mathbf{D}}} \qquad \textbf{eq14}$$

The element $\mathbf{M_p}$ in **Eq18**, also called penetration depth, represents the impedance due to the electrode porosity at a certain frequency. **D** and $\mathbf{R_p}$ are the coefficient of diffusion and the resistance of pores to ions migration.

Circuit frequency response

When a complex electrochemical system is subjected to EIS analysis a proper equivalent circuit should be designed in order to extrapolate resistance and capacitance values. Several circuit configuration can be considered, wherein circuit component are connected in series or

in parallel. When the circuit components are connected in series (**eq15**), the total impedance is the summation of the impedance values of each component. In circuit configured in parallel, the reciprocal of the overall impedance is equal to the summation of each reciprocal impedance (**eq16**).

$$\mathbf{Z_{tot} = Z_1 + Z_2 \ldots + Z_n = \sum_{n=0}^{n} Z_n \overset{n2}{\rightarrow} Z_{tot} = Z_1 + Z_2} \qquad \textbf{eq15}$$

$$\mathbf{\frac{1}{Z_{tot}} = \frac{1}{Z_1} + \frac{1}{Z_2} + \cdots + \frac{1}{Z_n} = \sum_{n=0}^{n} \frac{1}{Z_n} \overset{n2}{\rightarrow} \frac{1}{Z_{tot}} = \frac{Z_1 + Z_2}{Z_1 Z_2}} \qquad \textbf{eq16}$$

Figure 2-5a and Figure 2-5b are examples of RC circuit wherein the capacitance and the resistance elements are configured in series (R+C). Typically, EIS spectra are represented in a Nyquist plot or in a Bode plot according to **eq17**.

$$\mathbf{Z_{tot} = R - \frac{1}{C(J\omega)}}. \qquad \textbf{eq17}$$

Nyquist plot reports both impedance phasors in the complex plane. The imaginary component is conventionally reported as a negative value in order to have both phasors in the positive half plane. Bode plot reports both phase shift and impedance modulus versus frequency.

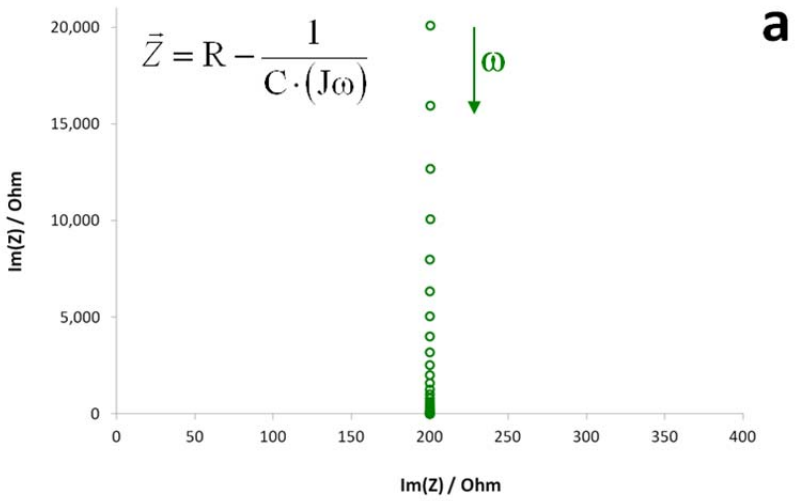

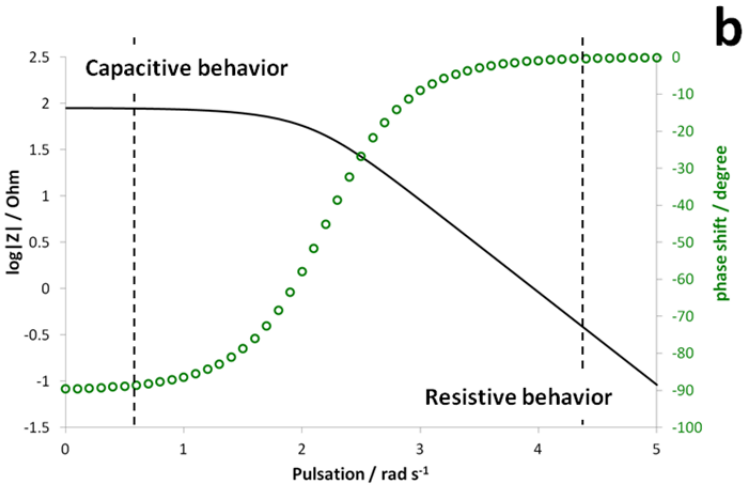

Figure 2-5 Box-a Nyquist plot, Box-b bode plot of R+C circuit

As depicted in Figure 2-5a, such circuit reveals in the Nyquist plane a vertical distribution of data points. This proves that the imaginary phasor increases by decreasing the pulsation, whereas real phasors do not respond to the pulsation sweep. On the other hand, Bode plot reveals that the circuit behaves as a pure resistor (θ=0) at high frequency and that, by decreasing the pulsation, it behaves as a capacitor (θ=90). For all these reasons, the modulus of |Z| approaches to the resistance and to the capacitance by increasing and reducing the pulsation of the voltage. Thus one can extrapolate resistance and capacitance by the modulus of Z calculated at null or infinite pulsation.

In case of R and C elements connected in parallel (R/C), Figure 2-6-a, both phasors change during the sweep of frequency according to **eq18**.

$$\mathbf{Z_{tot}} = -\frac{\mathbf{R}}{\mathbf{RC(J\omega)-1}}. \qquad \textbf{eq18}$$

Thus the impedance vector approaches the real axis by decreasing the pulsation and therefore one can calculate the resistance as the intercept value of the spectrum to the real axis. In the **eq19** the rationale already described has been formalized. Cambria Math

$$\log_{\omega\to 0}|Z| = \log_{\omega\to 0}\left[-\frac{R}{RC(J\omega)-1}\right] = R \qquad \textbf{eq19}$$

Considering that a phase shift "θ" equal 45° determine the condition wherein both phasors are equal. One can assume that "ω^{-1}" corresponds to the product between the resistance "**R**" and the capacitance "**C**". Thus, capacitance could be calculated as the reciprocal of the product

between the resistance "**R**" and the pulsation "**ω**", under the condition wherein **θ** is equal 45°. In the **eq20** the formalism here described has been formalized.

$$\mathbf{If}\ \varphi \to 45^{\circ}\ \mathbf{else}\ \omega^{-1} \quad = RC \to C = \frac{1}{R\omega} \qquad \textbf{eq20}$$

Looking at the frequency response (Bode plot, Figure 2-6-b), one ca notice that current flow through the capacitor a high frequency (capacitive behaviour) and then flow preferentially through the resistor by the very lowering of pulsation (resistive behaviour).

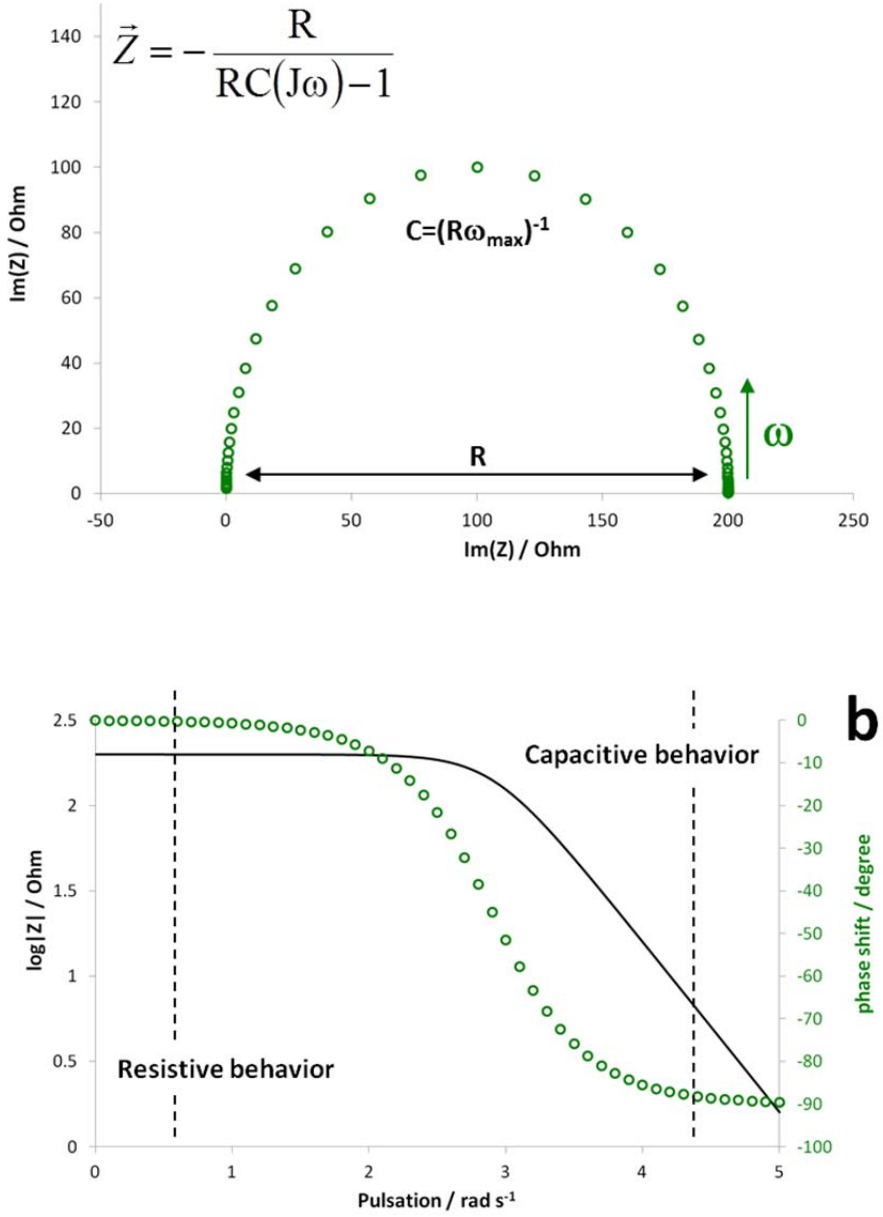

Figure 2-6 Box-a Nyquist plot, b Bode plot of R/C circuit

2.9. The practical case of Li-Ion cell

According to literature Figure 2-7, a Li-Ion cell could be analysed by EIS-measurements by applying an AC-potential of 10 mV, with a sweep of frequency from 100 KHz to 100 mHz, under a sampling rate of 10 points per decade.

In order to do a proper mathematical fitting of the data set, different kinds of phenomena should be taken into account.

Figure 2-7 reports a representative example of an EIS spectrum obtained from a Li-Ion cell. As reported in literature [7], it usually consists of two, or more, convolved semicircles that represent the overlapping of different phenomena, occurred during the sweep of frequency.

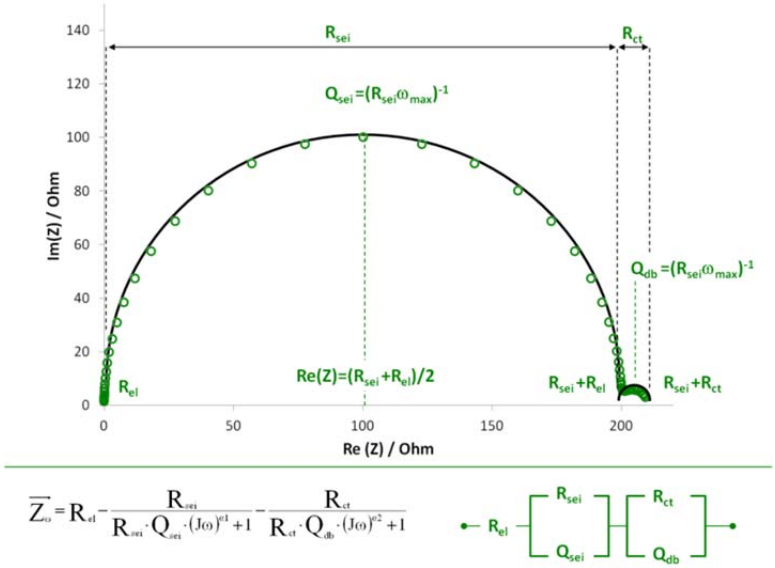

Figure 2-7 EIS spectrum expected for Li-Ion Cell

The phenomenon observed at high frequency is the ion motion within the electrolyte. In particular ions are able to migrate at high frequency (100-50 kHz) and to accumulate at the electrode/electrolyte interface at low frequency (1-0.01Hz). The first phenomenon gives rise to an ohmic-resistance (**R_{el}~10Ω**) and the charge accumulation develops a pseudo-capacitance (**Q_{bd}~5mF**).

On the electrode side, more complicated evaluations should be done, by considering both bulk and surface properties. In particular, electrodes are usually covered by passivation layers. In the special case on Li-ion cells, passivation layers (SEI) display both ion-conducting properties and self-capacitance, which lead to describe it as a parallel configuration of **R_{SEI}** (**~200Ω, 10-1Hz**) and **Q_{SEI}** (**~5μF, 100-10Hz**) elements. In the bulk region of the electrode, the most important process is charge transfer, which must be considered as a pure ohmic resistance at very low frequency (**R_{ct}~50Ω**). **R_{ct}** and **Q_{bd}** belong to the same frequency domain and therefore

they should be considered as elements in parallel, despite they are localised in two different region of the electrochemical system (bulk electrode and interface).

Summarising, the semicircle in the high frequency region (100 kHz-1 Hz) represents the impedance response due to passivation layer (SEI) and the semicircle in the low frequency region is the response due to charge transfer and interface capacitance.

2.10. Introduction to GCPL technique

Galvanostatic cycling with potential limitation is the method of choice to assess on a lab scale the performances of electrochemical cells aimed at working as energy storage devices. The technique is based on the measurement of the potential difference between at least a couple electrodes, under the condition of a constant current flow between them. Undesired electrochemical reactions could be avoided by stopping or inverting the current flow, whether the potential difference between electrodes exceed specific potential limits. For these reasons the electrochemical equipment of choice to perform this kind of measurements are the potentiostat/galvanostat instrumentations.

According to the first Ohm law (**V=RI**) the potential difference between the electrodes (**V**) changes in order to sustain the current flow through the electrolyte, which behaves as an ohmic resistor (**R**).

When the current is flowing, faradic processes might occur at the electrode/electrolyte interfaces. The driving force of the reaction is the difference between the redox potential of the electrode material and the redox potential of the active species dissolved in the electrolyte.

In the case of electrochemical cells consisting of ideal electrodes, the faradic processes must occur when one of the electrode reach the reversible redox potential of the species dissolved in the electrolyte. On the contrary, real electrodes react frequently at potentials higher than the reversible redox potential. In electrochemistry, the difference between the reversible and the experimental redox potentials is called overpotential.

Whether a galvanostatic cycling is performed onto non ideal electrode, and without feedback control, a lowering of the current flow could occur because of overpotentials or electrodes passivation. In order to avoid current drops, the potentiostat/galvanostat instrumentation increases the potential difference between electrodes (**ΔV>0**). Summarising an electrochemical cell, consisting of real electrodes, does not reveal a constant voltage profile. Figure 2-8 summarised the behaviour expected for a real electrode under galvanostatic cycling.

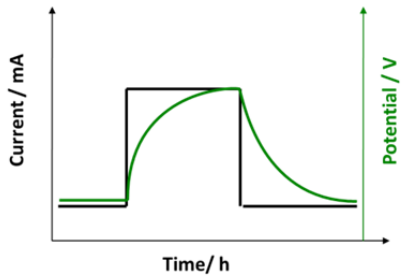

Figure 2-8 behaviour of real electrode under galvanostatic cycling

In this condition the electrochemical cell works under kinetic control. All of the electrochemical reactions that are kinetically favoured can take place at the electrode/electrolyte interface. Moreover further electrochemical reactions might occur when the cell voltage increases.
In order to prevent undesired reactions, this kind of experiment should be performed by applying potential limits. A more precise control of both electrode potentials can be achieves by using an additional electrode, which must be configured as reference.

2.11. The rationale of GCPL

In the specific case of Li-ion technology, the electrochemical cell consists of two electrodes, separated by a porous insulator (separator) which prevents shorting. The circuit is closed by an electrolyte, which migrates through the separator ensuring conduction by ion transport.
In particular, Li-ion technology is based on electroactive intercalation compounds. Despite metallic electrodes, electroactive intercalation compounds do not transfer electrons to the electrolyte. They only intercalate (or deintercalate) Li^+ cations from the electrolyte. During intercalation, lithium does not react itself. It only induces variation in the oxidation state of other atoms present in the electrode lattice. Redox processes determine macroscopic effects on the electrode structure, which results from phase transitions.
The basic characteristic of an electroactive intercalation compound is the voltage-composition relationship, which has been published by Armand and co-worker in 1980 [8].
Basically a GCPL experiment represents a continuous dependency of the composition vs. potential of the electrode. When the current flow through the cell, Li^+ cations are progressively intercalated (or deintercalated) by the electrode, which change is potential in order to support intercalation processes. In particular, the electrode structure might be considered as a solid-solution, thus monotonous potential trend corresponds to single-phase domain whereas potential plateau corresponds to a two-phase domain.
As reported in chapter 1, Al/$LiCoO_2$ and Cu/Graphite are frequently used within Li-ion cell as cathode and anode intercalation electrodes.

2.12. The GCPL experiment on Li-ion cell

The GCPL experiment starts by imposing an electrons flow from the cathode (Al/$LiCoO_2$) to the anode (Cu/Graphite). Structural modification occurred on both electrodes. In particular,

cathode releases Li^+ cations into the electrolyte (deinsertion) and anode stores Li^+ into interplanar regions (intercalation). The reaction at the cathode is reported below:

$$\mathbf{LiCoO_2 \longrightarrow Li_{1-x}CoO_2 + xe^- + xLi^+}$$

In this case the potential difference between electrodes is limited to 4.2V (vs. Li/Li^+), because at higher potentials (5.0V vs. Li/Li^+, [9]) a phase transition occurs to cathode, generating hexagonal lattice, whose reactions are irreversible. Thus intercalation processes should stop when cathode reach the stoichiometry $Li_{0.5}CoO_2$.

The reaction involved at the anode is reported below In this case the potential limit is fixed at 0.001V (vs. Li/Li^+), because the last stage intercalated compound of graphite is LiC_6, which is developed around 0.001V (vs. Li/Li^+).

$$\mathbf{xe^- + xLi^+ + nC \longrightarrow Li_xC_n \longrightarrow LiC_6}$$

When the electrochemical cell reaches the potential limits, the current flow is reverted and therefore all reactions shift toward the opposite directions. In this case the potential limits of anode and cathode are 2.5V and 3.0V (vs. Li/Li^+), respectively. These limits correspond to the pristine stoichiometry of both electrodes.

Figure 2-9 reports an example of a GCPL experiment. The black, red and blue curves refer to current profile, cathode and anode potentials, respectively.

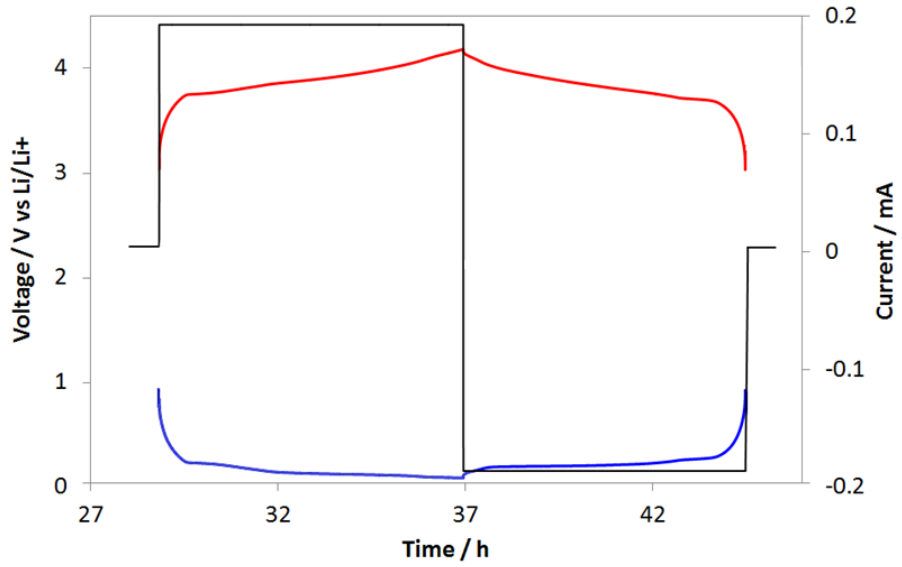

Figure 2-9 GCPL of a Li-ion cell. (red) cathode potential, (blue) anode potential and (black) currents profile

Looking on the potential profile of both cathode and anode one can notice the presence of flexes, which are attributed to modifications occurred to the electrode structures. Figure 2-10 reports an example of structural modification occurred to the electrodes during the charge process. In the figure the potential responses due the cathode and the anode have been reported as red and blue traces, respectively.

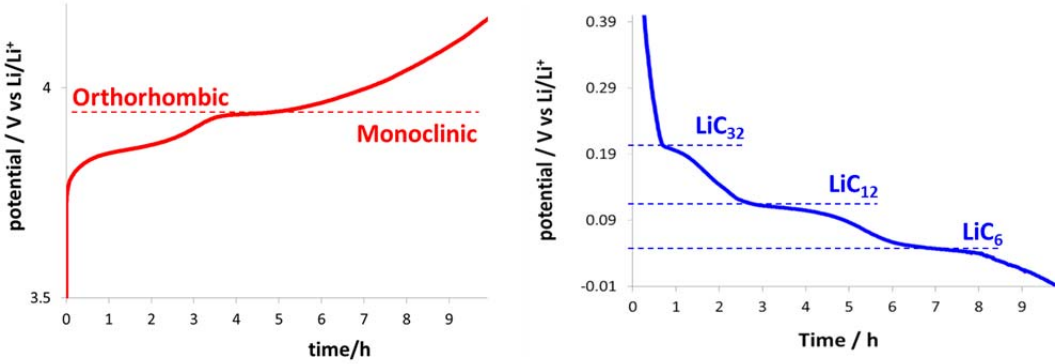

Figure 2-10 phase transition during charge. (red) cathode behaviour, (blue) anode behaviour.

Looking at the red plot a phase transition occurred to the cathode around a 3.9V. According to literature, it is attributed to the growing of monoclinic domain in some grains of the electrode [9]. At the anode side three different intercalation stage compounds could be observed around 0.20V, 0.12V and 0.8V. According to literature [9] they have been attributed to LiC_{32}, LiC_{12} and LiC_6 compounds.

Additional evaluations could be done, noticing that the potential difference between electrodes increases by imposing a positive current flow between cathode and anode. On the contrary, the potential difference between electrodes reduces by reverting the current flow. Considering the direct dependency between the Gibbs energy the cell voltage, one can conclude that positive and negative current flows increase and reduce the cell voltage, increasing and reducing the work obtainable from the electrochemical system.

In conclusion, the electrochemical cell behaves as an energy storage device and thus GCPL experiment provides quantitative information about energy storage performances.

By performing GCPL experiment five fundamental parameters could be obtained and they could be used to describe properly the behaviour of Li ion cell. These descriptors have been briefly summarised below, according to literature [**10**].

- **OV** (operative voltage of the cell). It is the voltage at which the device works properly, and it represents the electrochemical condition in which current and potential are not correlated.

- **C** (capacity). It represents the charge stored (or released) by charging (or discharging) the cell for 1h. In order to refer capacities to charge and discharge processes $\mathbf{C_d}$ and $\mathbf{C_c}$ notation are used to specify discharge and charge capacities. These parameters are physically defined as the product between the current and the time required to reach the charge (or discharge) potential limit. In order to have parameters independent on the amount of active material, capacities are conventionally normalised for the mass of the electrode.

- **SE** (Specific energy): It represents the energy which could be released by discharging the cell. Specific energy is physically defined as the product between discharge capacity and operative voltage of the cell.

- **E%** (cell Efficiency). Calculated as the ratio between discharge and charge capacity ($\mathbf{C_d/C_c}$), it represents the yield of the energy storage process.

- **CR% (**Capacity Retention). Calculated as the ratio between the last and the first discharge capacity ($\mathbf{C_{d\text{-}1}/C_{d\text{-}last}}$). It describes the ageing of the device.

2.13. Reference

1. Gohlke, R. S Anal. Chem. 1959, 31, 535-41
2. Ann Arbor.Clin Chem. (2003), 49(7):1041-4.
3. Di Brian C. Smith, Fundamentals of Fourier Transform Infrared Spectroscopy (CRC press, 1996)
4. Di Andrzej Wieckowski Interfacial Electrochemistry (M. Dekker INC, 1999), pp 6-12
5. Juan Bisquert J. Phys. Chem. B, 2002, 106 (2), pp 325–333
6. Digby D. Macdonald Electrochimica Acta, 51 (2006), 1376–1388
7. Walter van Schalkwijk,Bruno Scrosati Advances in Lithium-Ion Batteries (2002), 31-41
8. M.B. Armand Materials for Advanced, 21, 1981, pp 271-311
9. T. Okumura,Y. Yamaguchi, M. Shikano and H. KobayashiJ. Mater. Chem. (2012), 22, 17340

10. C. Daniel, J. O. Besenhard Handbook of Battery Materials (2011), Wiley-VCH.

Chapter 3

Electrochemical test protocol

3.1. Abstract

This chapter describes the experimental procedures and electrochemical protocols followed to validate the Li-ion cell prototype. At a lab scale, the cell consisted of a Li-Ion device which should mimic a commercial lithium ion cell.

3.2. A glossary about the electrochemical descriptors

In order to do a proper comparison among Li-ion cells, four descriptors were assumed:

- **OV** (operative voltage of the cell). It is the voltage at which the device works properly, and it represents the electrochemical condition in which current and potential are not correlated.
- **C** (capacity). It represents the current stored (or released) by charging (or discharging) the cell for 1h. These parameters are conventionally normalised for the mass of the limiting current electrode.
- **E%** (cell Efficiency). Calculated as ration been discharge and charge capacity ($\mathbf{C_d/C_c}$), it represents the yield of the energy storage process.
- **CR% (**Capacity Retention). Calculated as the ratio between the last and the first discharge capacity ($\mathbf{C_{d\text{-}1}/C_{d\text{-}last}}$). It describes the ageing of the device.

These parameters have been found useful to assess the performances and reproducibility of the electrochemical responses exhibited by the Li-ion cells assembled in lab.

3.3. Cells Assembly

The equipment for cell assembly has been kept within an argon glove box (O2 and H2O lower than 0.5 ppm), and it has been listed below:

- Electrolyte: Lp30 (ethylene carbonate / dimethyl carbonate (1:1 v/v) LiPF6 1M, Merck)
- Cathode: Al/LiCoO2 (d=1cm, 16mg, 140 mAhg-1, MTI Corporation)
- Anode: Cu/C (d=1cm, 18mg, 330 mAhg-1, MTI Corporation)
- Separator: 2 disks (d=1cm, 8mg of glass fibres, Whatman)
- Reference electrode: Li (h=1.5cm, w=0.2cm, Rockwood Lithium)

The assembling procedure starts by spotting 50ul of electrolyte on separators, which have been sandwiched between anode and cathode and then positioned into a T-shaped polypropylene junction. A Lithium wire (pseudo reference) has been inserted between separators and in the end the cell has been closed by using three stainless steel current collectors, see Figure 1-a.

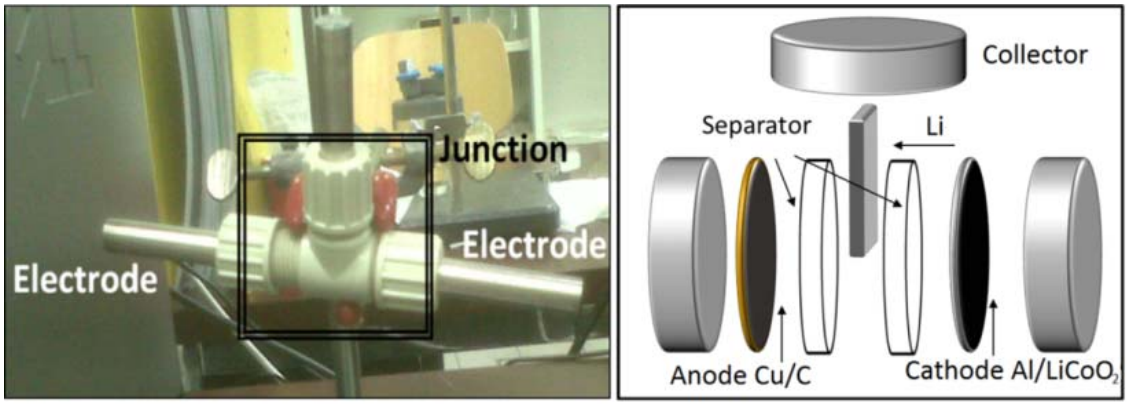

Figure 3-1 Scheme of Li-ion device

3.4. Potentiometric evaluations

When electrodes and electrolyte interact together, several decomposition processes can start. These processes involve the electrodes passivation and they result in the accumulation of insoluble side products. The insoluble species rest embedded on the electrodes surface, hampering the chemical contact between electrolyte and electrodes. Passivation is a spontaneous electrochemical process which determines weak electron transfers at the electrode/electrolyte interface. Thus one can conclude that the measurement of the cell voltage in open circuit condition (**OCV**), represents a good way to probe passivation in real time. To do so, the cell has been configured to use cathode as Working Electrode (**We**), the anode as Counter (**Ce**) and lithium as Reference Electrode (**Re**). OCV has been assessed by measuring separately the potential difference between We/Re and Ce/Re electrodes couples.

According to literature [2], a well performing cell usually stabilizes in 10 h. The experimental results reported in Figure 3-2, proved that cell stabilised in approximately than 10h.

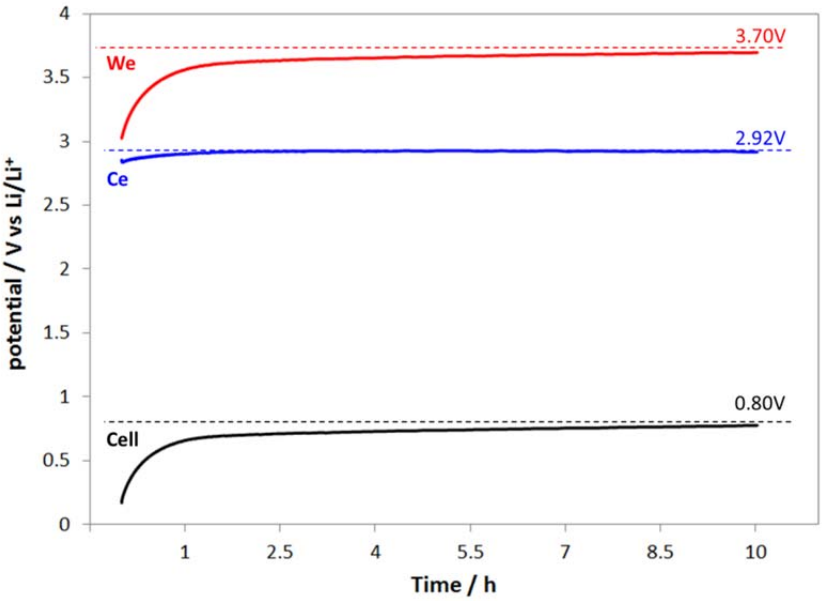

Figure 3-2 OCV stabilization profile of Full Li-ion cell (C/Lp30/$LiCoO_2$) (•-red) We/Re-potential, (•-blue) Ce/Re-potential, (•-black) cell-Voltage

An example of a less performing cell is reported in Figure 3-3. Looking at the plot one can notice that several perturbation of the voltage occurred. The evidence of electrical noise is typically diagnostic of a bad electric contact among electrodes; the voltage fluctuations indicate the diffusion of oxygen in the cell (oxidation of Re), and the presence of local minima (or maxima) in the potential curves are due to the development of faradic processes which are not related to the passivation.. By disassembling the device that gave the behaviour plotted in Figure 3-3, it has been observed that a part of the active phase ($LiCoO_2$ powder) detached from the electrode, exposing the current collector to the electrolyte. The current collector and the electrolyte react leading to the poor performance of the electrochemical cell.

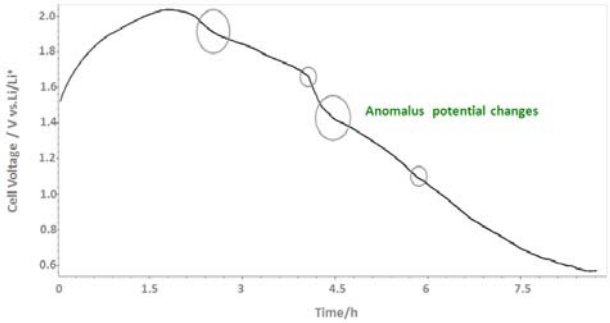

Figure 3-3 example of OCV trace of We electrode stabilization of a less performing Full Li-ion cell (C/Lp30/$LiCoO_2$)

Summarising, a full cell assembled in a proper way should exhibit a stable OCV of approximately 1 V (vs Li/Li^+).

3.5. SEI formation

During the first cycles of the cell the electrolyte decomposes on the electrodes surface, developing passivation layers (Solid Electrolyte Interface, SEI); once this layer covers the electrode surface, the electrolyte does not decompose further. Thus the cell can be cycled continuously, avoiding the energy consumption due to side reaction (capacity fade) [**1**].

Although, the SEI grows up during OCV stabilization, these passivation layers are too fragile to support cell cycling. In fact, during cycling Li^+ intercalation and deintercalation expands and contracts the electrodes, increasing the risk of fractures along the SEI. Thus an electrochemical consolidation step (SEI formation) is necessary to increase the mechanical resistance of these layers.

To do so, the cell has been subjected to galvanostatic cycling with potential limitations (GCPL). Cycling has been performed at C/10 (10 h, 0.26 mA, 140mAhg^{-1}) and 4.2V and 3.0V (vs. Li/Li^+) as potential limits for charge and discharge process, respectively. Figure 3-4 reports an example of GCPL-formation.

The curve revealed a weak capacity loss. In particular, the time spent to charge the cell is longer than the time required to reach the discharge potential limit.

Thus one can conclude that active species (electrons and Li^+), which were not available anymore during discharge, have been probably involved in electrode passivation processes.

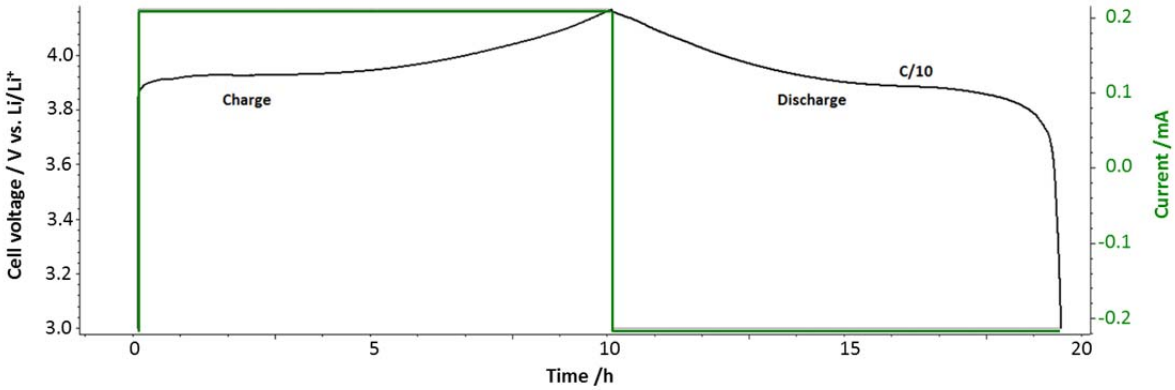

Figure 3-4 First SEI formation cycle (C/10) **of Full Li-ion cell, C/Lp30/$LiCoO_2$**

In general SEI consolidation could be also performed by working at higher C-rate, however low current leads to more efficient and more uniform passivation. In fact, working at low C/rate, passivation processes could occur efficiently also in the whole electrode including pores and interstices, reducing the risk of further side reactions.

3.6. CYCLING

After the formation-step, the cell is ready for cycling. Thus the C-rate should be increased up to C/1, measuring the number of cycles required to reduce the cell capacity under the threshold value of 110 $mAhg^{-1}$.

Figure 3-4 reports a representative example of GCPL experiments. Looking at the graph, one can see that the cell has been able to perform several cycles, exhibiting a capacity retention greater than the 80% (discharge capacities greater than 110 $mAhg^{-1}$). Experiment proves that cells are feasible and are able to perform tens of charge and discharge cycles, according to the expected behaviour of Al/$LiCoO_2$ and Cu/graphite electrodes [2].

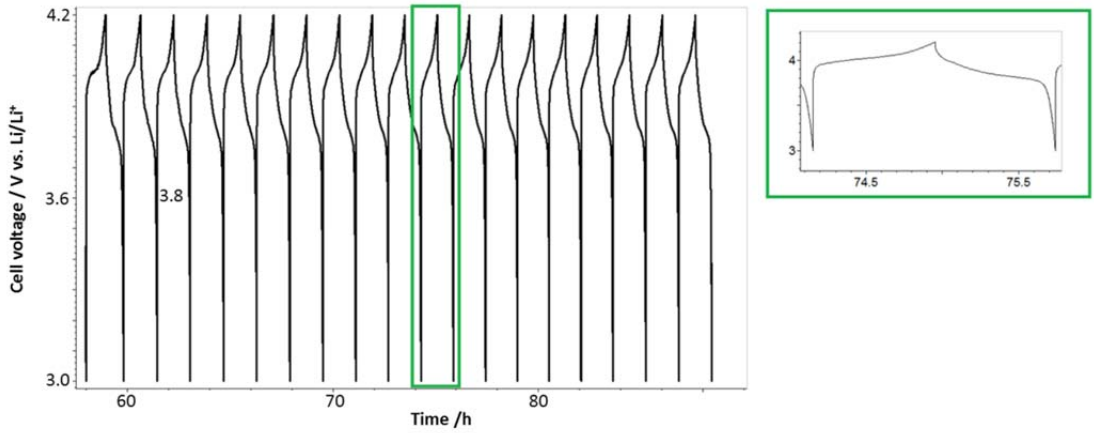

Figure 3-5 Full Li-ion cell (C/Lp30/$LiCoO_2$) cycling test, 20 charge/discharge cycles at C/1

3.7. C-rate effects

The Nominal Capacity (NC, 140mAhg-1) and the Operative Voltage (OV, 3.7 V vs Li/Li+) are two descriptors of the chemistry of Li-ion cell. Capacity represents the total amount of electrons released during discharge, and Operative Voltage is the discharge condition wherein current and voltage are independent.

In this experiment a cell has been assembled and conditioned following the procedures described above. It has been galvanostatically cycled at increasing C-rates (C/10, C/5, and C/1, with C/10 corresponding to 14.5 mAg^{-1}) and finally it has been cycled at C/10 again, evaluating from operative voltage (OV) and capacity (C) whether high C-rates might have led alteration in the chemistry of the cell. The results reported in Figure 3-6 show that, by discharging the cell at C/10, OV and C are in agreement with the values expected from the rated characteristics of the electrode materials(OV=3.7V vs. Li/Li^+, NC=140mAg^{-1}) [2], and that by increasing the C-rate they slightly decrease. By comparing the OV and C parameters obtained at C/10 at the beginning and at the end of the

experiment, it has been confirmed that no irreversible alteration occurred in the cell, because both C and OV have been completely recovered.

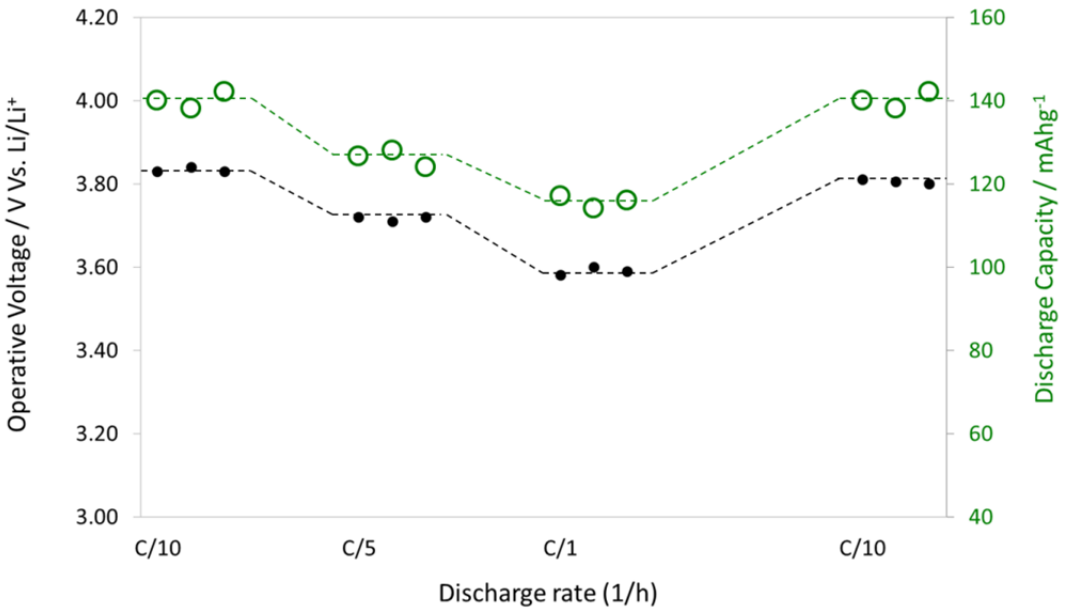

Figure 3-6 C-rate effects on operating voltage and discharge capacity. Experiment on full Li-ion cell (C/Lp30/$LiCoO_2$) discharge at C/10,C/5 and C/1

3.8. Cell validation

In order to assess the reproducibility of the assembling and testing procedures, three different cells were assembled, conditioned and tested.

In order to evaluate **C** and **OV** in reversible conditions, three galvanostatic cycles at C/10 have been performed after SEI formation, finding an average capacity for all cell equal to 136 ± 4 $mAhg^{-1}$ and an operative voltage of 3.82 ± 0.08 V (vs Li/Li^+). The galvanostatic response exhibited by the cells has been reported in Figure 3-7. A good agreement has been found by comparing these experimental results with the expected electrochemical behaviour, reported in literature for this cell configuration [3].

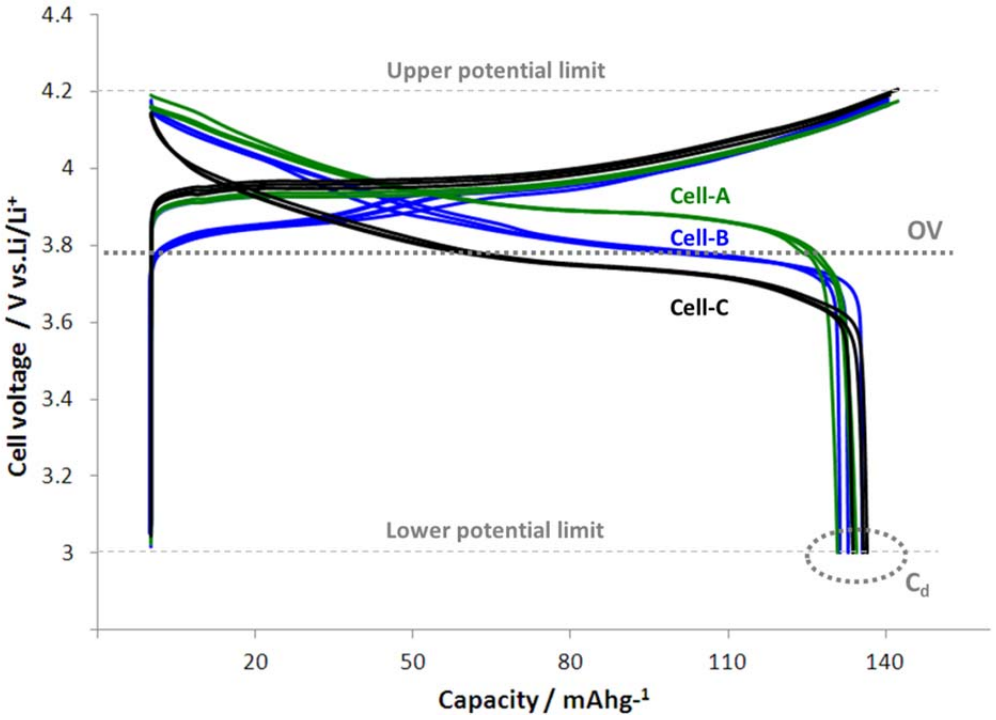

Figure 3-7 three discharge experiments of three different full Li-ion cells, C/Lp30/$LiCoO_2$ (rate C/10)

E% and **CR%** have been assessed by performing twenty galvanostatic cycles at C/5, results have been expressed as average values calculated for the cells under investigation. **E%** and **CR%** average values were 98% (± 1%) and 93% (± 3%), respectively. This C-rate has been chosen in order to perform a conservatory assessment of **E%** and **CR%** parameters in a realistic time of work.

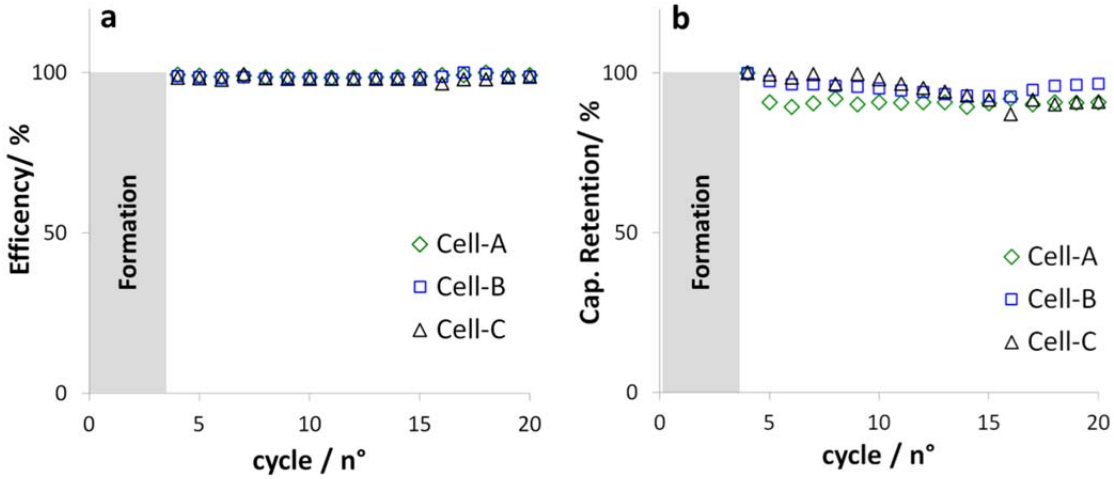

Figure 3-8 Cell efficiency and capacity retention of three different Li-ion cells (C/Lp30/$LiCoO_2$). Experiment at C/5 20 charge/discharge cycles

The results obtained at the end of this validation procedure have been compared with other data the reported in literature by B. Huang at all in 1998 [2]. The good agreement between experimental data and several other scientific work reported in literature [2-3] leads to consider the experimental procedure as a validated tool, useful for assembling on a Lab scale a well performing Li-ion cell.

3.9. Electrochemical impedance spectroscopy (EIS)

EIS technique can provide indirect information about electrodes, electrolyte and SEI. The electrochemical apparatus has been set to apply a bias voltage of 5mV, with a sweep of frequency which ranged from 100 kHz to 50 mHz. To understand the electrochemical behaviour of pristine electrodes and the convolution of signals due to different electrodes in full Li-Ion cells, symmetric and asymmetric cells have been analysed by EIS. The features of the cells tested are reported in Table 3-1.

Table 3-1 Features of cells subjected to EIS investigation

Cell	Configuration	We	Ce	Electrolyte (LP30)
Li/Li	Li/LP30/Li	Li (7mg)	Li (7mg)	50 μL (EC/DMC 1:$_{1\ v/v}$ $LiPF_6$ 1 M)
C/C	C/LP30/C	C (15mg)	C (15mg)	50 μL (EC/DMC 1:$_{1\ v/v}$ $LiPF_6$ 1 M)
Co/Co	$LiCoO_2$/LP30/ $LiCoO_2$	$LiCoO_2$ (18mg)	$LiCoO_2$ (18mg)	50 μL (EC/DMC 1:$_{1\ v/v}$ $LiPF_6$ 1 M)
C/Li	C/LP30/Li	C (15mg)	Li (7mg)	50 μL (EC/DMC 1:$_{1\ v/v}$ $LiPF_6$ 1 M)
Co/Li	$LiCoO_2$/LP30/ Li	$LiCoO_2$ (18mg)	Li (7mg)	50 μL (EC/DMC 1:$_{1\ v/v}$ $LiPF_6$ 1 M)

Symmetric cells

The first EIS experiment has been performed on Li/Li cell and the results have been reported in Figure 3-9. The plot consists of two convolved semicircles, which represent the characteristic behaviour of non-blocking electrodes (faradic processes at the electrode/electrolyte interface).

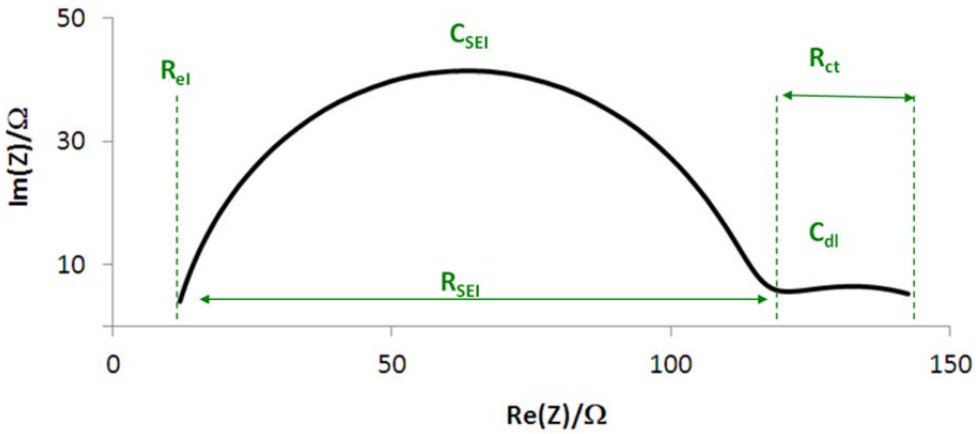

Figure 3-9 EIS spectrum of Li/Li cell. Bias voltage 5mV, frequency range 100kz-50mHz

The data have been interpolated with the equivalent circuit **Ec**[1], which has been sketched in Figure 3-10, and it could be described by using the following notation "$\mathbf{R_{el}+(C_{sei}/R_{sei})+(C_{dl}/R_{ct})}$",

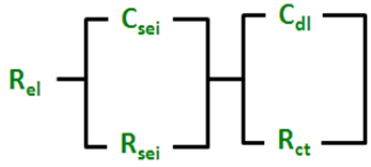

Figure 3-10 equivalent circuit of Li/Li cell

This circuit described the electrochemical system. In particular, $\mathbf{R_{el}}$ is the ionic resistance of the electrolyte and it is connected in series with other two elements, $\mathbf{C_{sei}/R_{sei}}$ and $\mathbf{C_{db}/R_{ct}}$. The $\mathbf{C_{sei}/R_{sei}}$ elements represent the parallel connection between the capacitance and the resistance due to SEI. The $\mathbf{C_{dl}/R_{ct}}$ element represents the parallel connection between the capacitance of the double layer and the charge transfer resistance at the electrode/electrolyte interface.

The experiment carried out on C/C cell is reported in Figure 3-11. In this case the experiment has not revealed faradic processes at low frequency, as expected for an electrochemical cell with blocking electrodes, covered by a weak passivating layer.

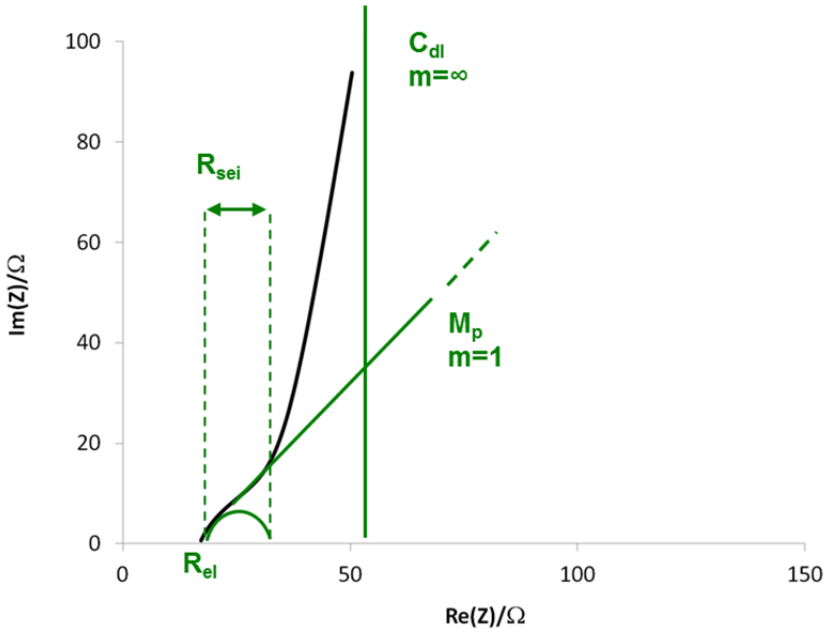

Figure 3-11. EIS spectrum of C/C cell. Bias voltage 5mV, frequency range 100kHz-50mHz

In particular, the high-frequency semicircle represents the response of the Rel+(Csei/Rsei) circuit element. Looking on the plot one can observe one can recognize the typical plot displayed by porous materials. The linear domain, with a unitary slope coefficient, is attributed to the diffusion resistance of ions across pores. In the low frequency region a second linear domain can be observed and it is attributed to the double layer capacitance. In order to fit this spectrum, the equivalent circuit **Ec^2** has been used, which could be described by using the following notation "**R_{el}+(C_{sei}/R_{sei})+(M_p+C_{dl})**".

The element **M_p**, also called penetration depth, represents the impedance due to the electrode porosity and it is mathematically defined as: $M_p = R_p \frac{\coth\sqrt{j\omega/D}}{\sqrt{j\omega/D}}$; where D is the diffusion coefficient, ω is the angular frequency, j is the imaginary unit, and R_p is the porous resistance. The equivalent circuits has been sketched in Figure 3-12

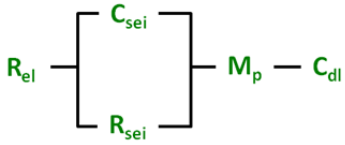

Figure 3-12 equivalent circuit of C/C cell

Co/Co cell has shown a a behaviour typical of less porous electrodes (see Figure 3-13). The EIS displayed an evident semicircle at high frequency followed by a straight line at low frequency (double layer capacitance). The data set had been interpolated with the equivalent circuit **Ec^3**, with the notation **R_{el}+(C_{sei}/R_{sei})+C_{dl}**. In this case the **M_p** parameter

has been neglected, according to the negligible contribution of pore resistance to the total cell impedance.

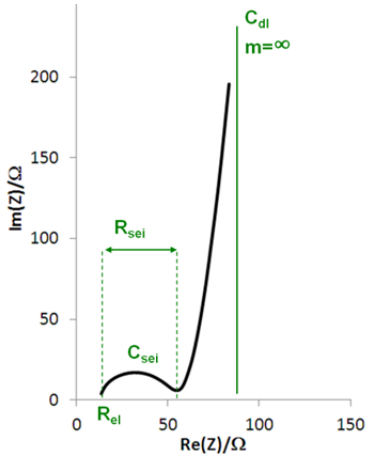

Figure 3-13 EIS spectrum of Co/Co cell. Bias voltage 5mV, frequency range 100kHz-50mHz

Asymmetric cells

Figure 3-14 reports in grey and black the spectra of C/Li and Co/Li cells respectively. Both cells have showed semicircles wider than the relative symmetric cells. Considering that the equivalent circuit modelled an half-cell, the EIS has revealed an average cell behaviour, which is evidently effected by the presence of Li-electrode. Thus one can conclude that the signals of C and Co electrodes convolve with the impedance of Li in the high frequency region. On the contrary, the higher double layer capacitances of C and Co electrodes exceeded the impedance due to electron transfer, which has not been observed. In order to fit the spectra of both asymmetric cells, **Ec^2** and **Ec^3** equivalent circuits have been used for C/Li and Co/Li cells, respectively.

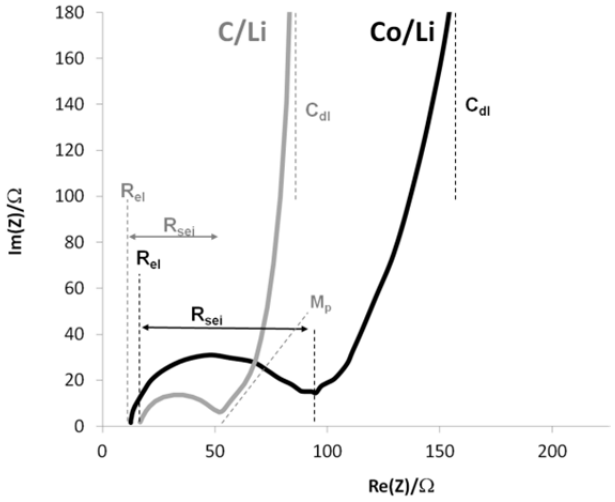

Figure 3-14 EIS spectrum of C/Li (grey) and Co/Li (black). Bias voltage 5mV, frequency range 100kHz-50mHz

Table 3-2 reports the results obtained by interpolating each data set with a proper equivalent circuit. By comparing symmetric and asymmetric cells, it is possible to notice that $\mathbf{R_{sei}}$ increases, whenever Li electrode is present in the cell. In particular the SEI resistance measured into Li/Li cell is the highest compared to all other cells.

Assuming a similar chemical composition among all SEI developed on the electrodes surface and considering the second Ohm, one can conclude that high values of $\mathbf{R_{sei}}$ reveal a thinking passivating layer and therefore greater reactivity at the electrode/electrolyte interface.

Looking at $\mathbf{C_{sei}}$, one can speculate that the wider is the specific surface of electrodes, the higher the SEI-capacitances is. As expected for electrodes with high specific surface, the C/C cell has shown the highest $\mathbf{C_{sei}}$, This class of electrodes is in fact characterised by the highest specific surface among all those used in the experiment. On the contrary, the double layer capacitances measured in the entire cells do not depends on the morphology of the electrode surface. According to the well-known behaviours of porous electrode [4], at very low frequencies the diffusion depth of ions into pores is strongly reduced. Thus rough electrodes are able to behave as smooth charged surfaces in the low frequency domain.

Summarising, the presence of a Li electrode into asymmetric cells induced an alteration in the impedance response in high frequencies region, but it did not exhibit strong distortions in the middle and low frequency domain.

Table 3-2 Results of EIS data fitting

Cell	R_{el} / Ωcm^{-2}	Q_{sei} / $\mu F\ cm^{-2}$	R_{sei} / $\Omega\ cm^{-2}$	Q_{db} / $mF\ cm^{-2}$	M_p / $\Omega\ cm^{-2}$	R_{ct} / $\Omega\ cm^{-2}$
Li/Li	14	8.9	107	0.41	Absent	43
C/C	16	98	31	0.11	318	Absent
Co/Co	14	18	48	0.65	Absent	Absent
C/Li	12	37	46	0.32	170	Absent
Co/Li	17	11	85	0.45	Absent	Absent

Full cells

Figure 3-15 reports the EIS spectrum acquired on a full Li-ion cell (C/LP30/$LiCoO_2$), assembled without the reference electrode. In this condition the analytical system is not able to separate the impedance response due to each cell component and the EIS reveals the impedance of the signals. For these reasons, the spectrum should be fitted with the equivalent circuit **Ec[4]**, whose notation is $\mathbf{R_{el}} + \sum_n \left(\frac{\mathbf{C_{SEI}}}{\mathbf{R_{SEI}}}\right) + \mathbf{C_{dl}}$. The summation operator

has been introduced in other to take in to account the stratification of SEI layers. The spectrum and its relative equivalent circuit have been sketched in Figure 3-15.

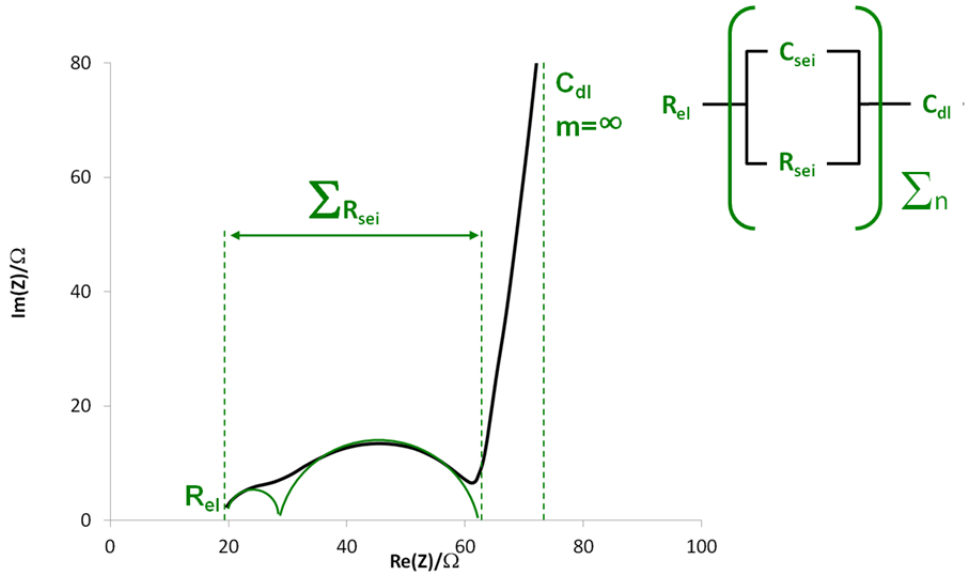

Figure 3-15 EIS spectrum of full Li-ion cell (C/Lp30/$LiCoO_2$). Bias voltage 5mV, frequency range 100kHz-50mHz

Looking at the plot one can distinguish the impedance due to cathode and anode. In particular, the small and big semicircles, positioned in the high and mid frequency domain respectively, represent the impedance of the SEI coatings, developed on anode and cathode surfaces, respectively. The shape of the spectrum lead to speculate that the SEI developed on both electrodes have real and imaginary impedances similar to the corresponding values measured on the C/C and Co/Co symmetric cells.
Although data fitting help to separate the impedances due to each SEI coating, this kind of approach is not conservative. In fact, further convolutions of impedance signals might take place during cell operations.

However by introducing a small Li wire between the separators and using it as a reference electrode, the convolution of signal could be avoided. In fact, such cell configuration makes the electrochemical apparatus able to measure separately the impedance due to each electrode. An example of this alternative approach is reported in Figure 3-16. Looking on the plot one can notice that both anode and cathode spectra resemble the impedance behaviours observed on Co/Li and C/Li asymmetric cells. Cathode and anode spectra have been fitted with **Ec^2** and **Ec^3** equivalent circuits, respectively. Resistance and capacitance obtained by data fitting have been reported Table 3-3

Table 3-3 result of Li-ion cell components at the steady state

Component	R_{el} / Ωcm^{-2}	Q_{sei} / μF cm^{-2}	R_{sei} / Ω cm^{-2}	Q_{db} / mF cm^{-2}	M_p / Ω cm^{-2}	R_{ct} / Ω cm^{-2}
cathode	13	21	54	0.51	Absent	Absent
anode	13	42	35	0.37	150	Absent

Results revealed that both anode/Re and cathode/Re electrodes couples showed a SEI resistance lower than the corresponding asymmetric cell. In fact, the asymmetric cells had a Li-disc electrode, on the contrary full Li-ion cell had only Li-wired between separators. According to the less extension of Li electrode, it should be expected a less perturbation of Li in the high frequency region.

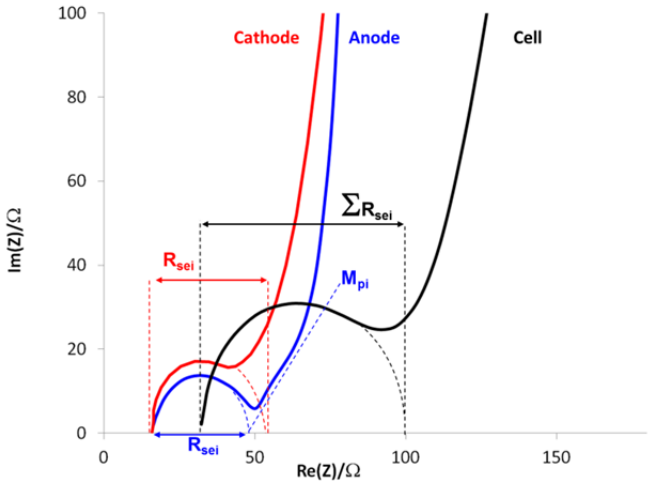

Figure 3-16 EIS Spectra of: anode (blue), cathode (red) and full cell (black). Spectrum of full Li-ion cell (C/Lp30/$LiCoO_2$). Bias voltage 5mV, frequency range 100kHz-50mHz

Summarising, one can conclude that symmetric and asymmetric cells described well the behaviours expected for Li ion cells assembled with or without the reference electrode.

EIS during charge and discharge

Full Li-ion cell can be analysed under operative condition, monitoring the electrochemical behaviour of cell components at different depth of charge and discharge. Figure 3-17 reports an example of EIS experiment performed on a single electrode during the first formation cycle (C/10 rate). Figure 3-17-reports the voltage profile of the cell during the course of the GCPL experiment. In particular the black and green branch of the curve refers to charge and discharge cycles, whereas the relative spot identify the moment of

the cycling during which EIS measurements have been carried out. Figure 3-17-b reports in black and green the EIS spectra recorded during cell charge and cell discharge.
The evaluations on the EIS-behaviour of the Al/$LiCoO_2$ electrode have been done, thanks to the presence of the reference electrode witch lead to measure separately the impedance of each electrode.

The electrochemical apparatus has been set to perform GCPL experiments, stopping the cycling after different period of time. In order to keep stable the cell voltage during the GCPL pauses, the cell has been supplied with the lowest current required to maintain the polarization of the electrodes. Once the cell voltage stabilised (that is, after a few minutes), EIS experiments have been performed by applying a bias voltage of ±5mV with a sweep of frequency, which ranged from 100kHz to 50 mHz.

Results revealed changes in the electrochemical behaviour of the electrode, according to the intercalation/deintercalation processes which occurred during cell cycling. First of all, Al/$LiCoO_2$ behaved as a non-blocking electrode by polarizing the cell (Figure 3-16. According to the case study represented by the Li/Li cell, all of the spectra have been fitted with **Ec**[1] equivalent circuit.

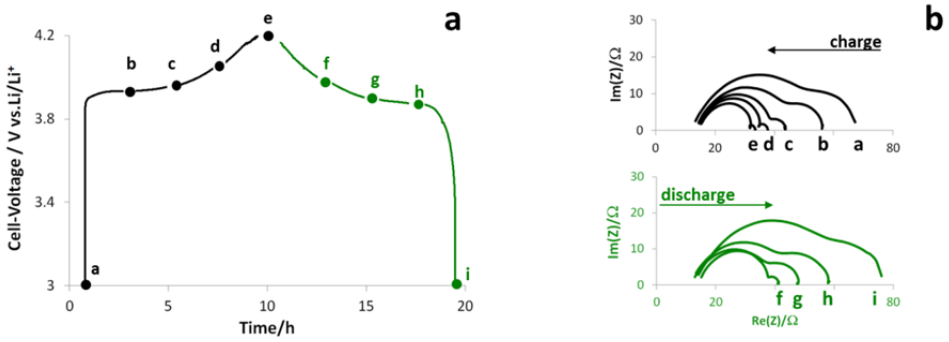

Figure 3-17 EIS measurements performed at different depths of charge and discharge of a full Li-ion cell (C/Lp30/$LiCoO_2$). Bias voltage 5mV, frequency range 100kH0z-50mHz

Results obtained by data fitting have been reported in Figure 3-18. The fitting revealed that $\mathbf{R_{sei}}$ and $\mathbf{R_{ct}}$ values decrease during charge and increased during discharge. On the contrary $\mathbf{R_{el}}$ slightly increased during charge and then decreased by discharging the cell.
The EIS behaviour could be explained according to the deintercalation/intercalation mechanism.
In particular, the charge process develops progressively vacancies in the valence bands of the cathode. By increasing the number of vacancies, faradic process is facilitated leading to a less charge transfer resistance ($\mathbf{R_{ct}}$ decrease).

Deintercalation processes conclude by transferring Li^+ cations from the electrode to its passivation layers (SEI). Thus by charging the cell, an additional amount of charge carries are injected by the electrode into the SEI. An increasing number of charge carriers leads to a more conductive passivation coating. Thus $\mathbf{R_{sei}}$ parameter should be decreased by charging the cell.

By inverting the polarization, valence bands should be saturated, leading to more difficult charge transfer processes ($\mathbf{R_{ct}}$ increases). Moreover, an electron reach cathode recalls Li^+ cations from the passivation coating. By depleting charge carries in the SEI, the passivation coating becomes progressively more insulating ($\mathbf{R_{ct}}$ increases).

The time evolution of the $\mathbf{R_{el}}$ parameter could be easily explained, taking into account the first Ohm law (R=V/I). Under galvanostatic conditions the current which flows through the cell is constant, whereas the cell voltage increases and decreases by charging and discharging the cell. Thus one can conclude that the greater is the potential difference between electrodes, the higher the resistance of the electrolyte will be.

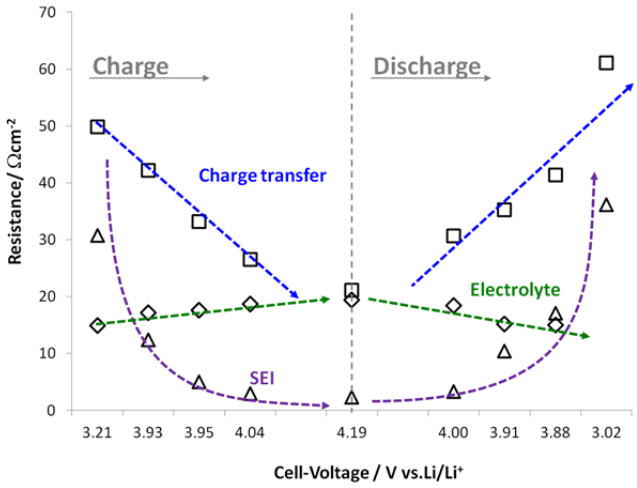

Figure 3-18 Resistances calculate by EIS data fitting

An alternative approach to assess directly the electrolyte resistance is the measurement of the DC resistance. This resistance is physically defined as the ration between cell voltage and current. In Figure 3-19 the **DC-Resistance** and the $\mathbf{R_{el}}$ parameter have been compared. Looking on the plot one can notice a strong agreement between measurements. According to the first Ohm law, both parameters exhibited trends similar to the cell voltage time evolution. Thus is correct to assume that $\mathbf{R_{el}}$ must change during cycling.

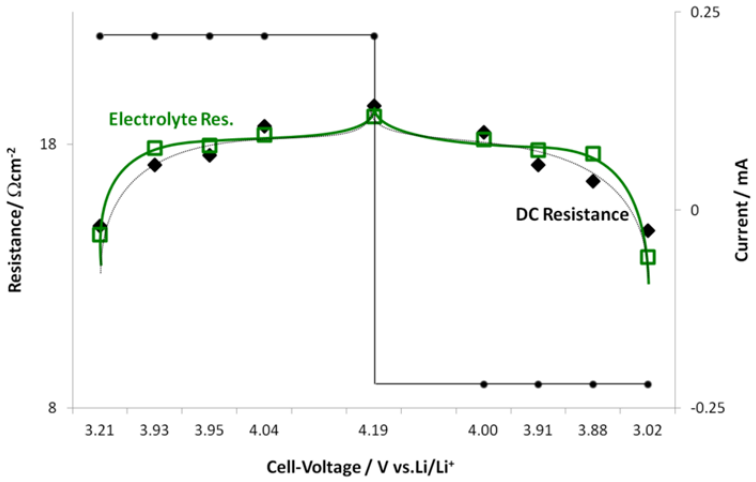

Figure 3-19 Comparison between Rel parameter and DC resistance.

Figure 3-20 reports the capacitances calculated by fitting the spectra. Looking at the plot one can notice that charging the cell the double layer capacitance ($\mathbf{C_{dl}}$) increased progressively, probably because a greater potential difference makes it possible to store more charge at the electrode/electrolyte interface. On the contrary, the capacitance of the SEI ($\mathbf{C_{sei}}$) decreased as soon as the current started to flow on charge and then it stabilised.

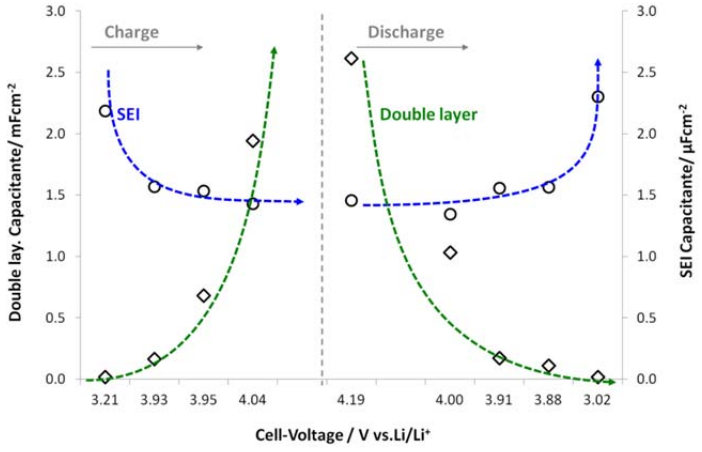

Figure 3-20 Capacitances calculate by EIS data fitting

In conclusion, by performing EIS measurements during GCPL experiment too many phenomena occurred making difficult the interpretation of cell behaviour. An alternative approach to probe the cell components during GCPL experiments consists of the measurement of the cell impedance in OCV conditions. This experimental procedure have been reported in the next paragraph.

Similar EIS results have been observed of the anode electrode and thus it has not been mentioned.

EIS during cycling

Following the rationale described in the last paragraph it is possible to check the cell conditions at different stages of cycling. Figure 3-21 shows the EIS spectra measured on the cathode in pristine condition and after the 1st(formation step), 5th and 10th galvanostatic cycles.

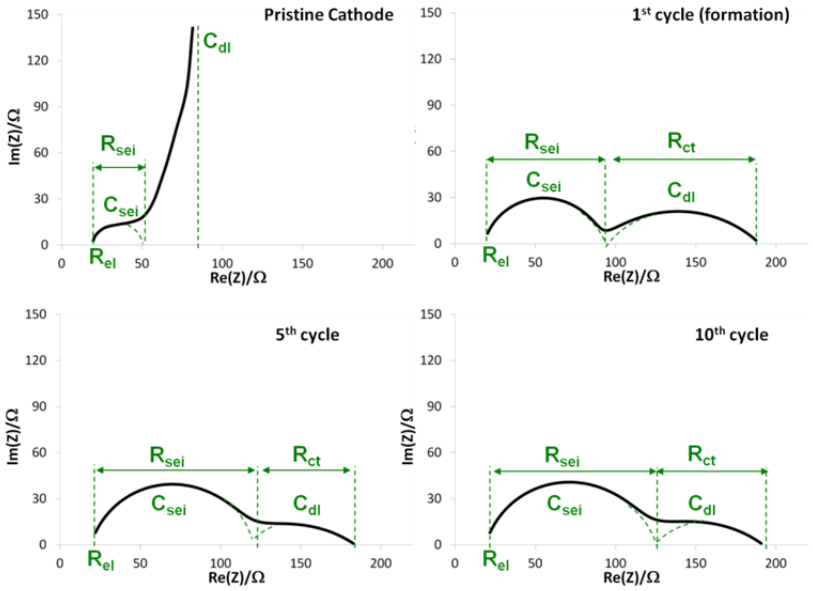

Figure 3-21 EIS spectra at different stage of cell cycling. Spectra recorded on full Li-ion cell (C/Lp30/$LiCoO_2$). Bias voltage 5mV, frequency range 100kHz-50mHz

EIS revealed that cathode behaved as a blocking electrode in pristine condition. However by polarizing the cell and performing the first formation cycle, the impedance response changed. Whenever a fresh electrode is polarized for the first time, several electrochemical processes occur at electrode/electrolyte interfaces. These reactions induce the passivation of the electrode (SEI growing) and the intercalation of Li cations within the electrode structure (charge transfer). Usually SEI and Li^+ intercalation processes have well defined frequency domains and they are represented in the Nyquist plot by two convolved semicircles in the high and mid-low frequency regions, respectively. EIS spectra have been fit according to the equivalent circuits described in the previous sections. Results have been reported in Table 3-4.

Table 3-4 Result of EIS spectra fitting of Li-ion cell during clycling

Stage of the experiment	R_{el} / Ωcm^{-2}	Q_{sei} / $\mu F cm^{-2}$	R_{sei} / Ωcm^{-2}	Q_{db} / $mF cm^{-2}$	R_{ct} / Ω cm^{-2}

Pristine	19.4	7.2	32	0.75	absent
1st formation cycle	21.9	3.4	79	0.25	97
5th cyclie	20.4	2.5	107	0.35	61
10th cycle	21.8	2.8	110	0.28	59

Experiments revealed that after formation charge transfer and SEI resistances stabilised leading to a well performing Li-ion cell.

Similar EIS results have been observed of the anode electrode and thus it has not been mentioned.

3.10. Conclusion

The electrochemical validation test has been successfully concluded confirming the reliability of the experimental procedure. The Li-ion cells have shown good performances and reproducible responses. However for the cell configuration, which has been adopted, it has been found very critical the amount of electrolyte introduced in the cell. In particular cells, with amounts of electrolyte greater than 100µl did not work properly.

The electrochemical test protocol has been optimised leading to experimental results in good agreement with the data already reported in literature.

Thus the methodology here proposed makes it possible to prepare and test, on lab scale, well performing Li-ion cells.

3.11. Reference

1. J. Fong, von Sacken , Dahn, J. Electrochem. Soc. 137 (1990) 2009
2. B. Huang, Y.I. Jang, Y.m. Chiang, D.. R. Sadoway Journal of Applied Elect. 28 (1998) 1365-1369.
3. S.k Jung, A.S. Cavanagh, A. C. Dillon, M. D. Groner, J. of The Electrochemical Society, 157 (1), A75-A81,
4. Digby D. Macdonald Electrochimica Acta 51 (2006) 1376–1388

Chapter 4

Spectroscopic test protocol

4.1. Abstract

This paragraph describes the experimental procedures followed to optimise and validate an analytical method based on FTIR (Fourier Transform Infrared Ray) spectroscopy, aimed at revealing CO_2 into isolated electrochemical systems.

4.2. Cells Assembly

Generally speaking, ideal FTIR-measurements should be carried out by preventing cross contamination, especially whenever the analyte is an anthropic species such as CO_2. In this case the analytical measurements are strongly susceptible to interday fluctuations [1]. However, once established that a specific flux of purge-gas, usually N_2, is sufficient to exclude CO_2 and prevent its back-diffusion into the analytical system, a conventional FTIR apparatus could be easily used for this kind of measurements.

In order to perform CO_2-measurements by excluding environmental contamination, a Jasco FTIR apparatus (580-plus) has been equipped with a purge-gas pipe line, supplied by high purity N_2 gas, as sketched in Figure 4-1.

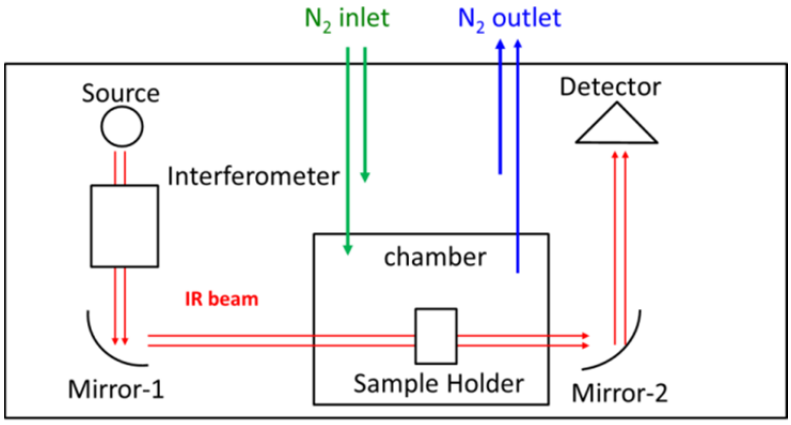

Figure 4-1 scheme of FTIR system

The optimal N_2 flow into the analytical system has been assessed by performing a depletion-test [2]. Experiments have been carried out by purging the FTIR apparatus for 60 minutes, with three different fluxes of N_2 (2.5, 5.0 and 10 $Lmin^{-1}$). During these experiments CO_2 has been revealed by using the FTIR detector, that was set to work at 2360 cm^{-1} (CO_2 asymmetric stretching) in normalised absorbance optical mode. Each spectrum has been recorded as the summation of 32 interferometer scans, acquired with a spectral resolution of 4 cm^{-1}. Figure 4-2 reports results obtained by assuming the average concentration of CO_2 in atmosphere (10^2 ppm) as normalization reference [1].

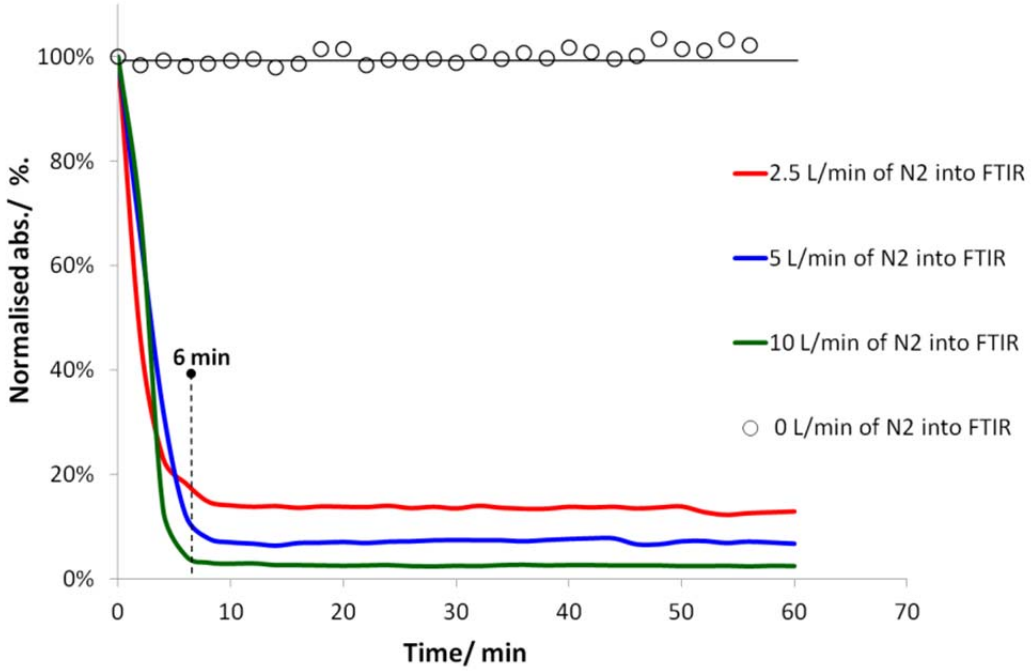

Figure 4-2 Depletion experiment performed at different flows of N_2 (red) 2.5 $Lmin^{-1}$, (blue) 5.0 $Lmin^{-1}$, (green) 10 $Lmin^{-1}$. CO_2 transmittance measured at 2360 cm^{-1}

Looking at the plot one can notice that IR signals stabilised in approximately 6 minutes, independently on the amount of N_2, fluxed into the system. Moreover, the higher the flux of N_2 is, the lower the residual CO_2 will be. In particular by fluxing N_2 at 10 $Lmin^{-1}$, the residual content of CO_2 has been found lower than 3% referred to average atmospheric concentration of CO_2. Well performing analytical conditions might have been obtained by increasing the flux of nitrogen, however, according to manufacturer prescriptions; higher fluxes of N_2 could compromise the interferometer stability.

In order to assess the stability of the analytical system during a long time scale experiment an additional depletion-test has been performed by prolonging it for 24 hour. Results have been reported in Figure 4-3.

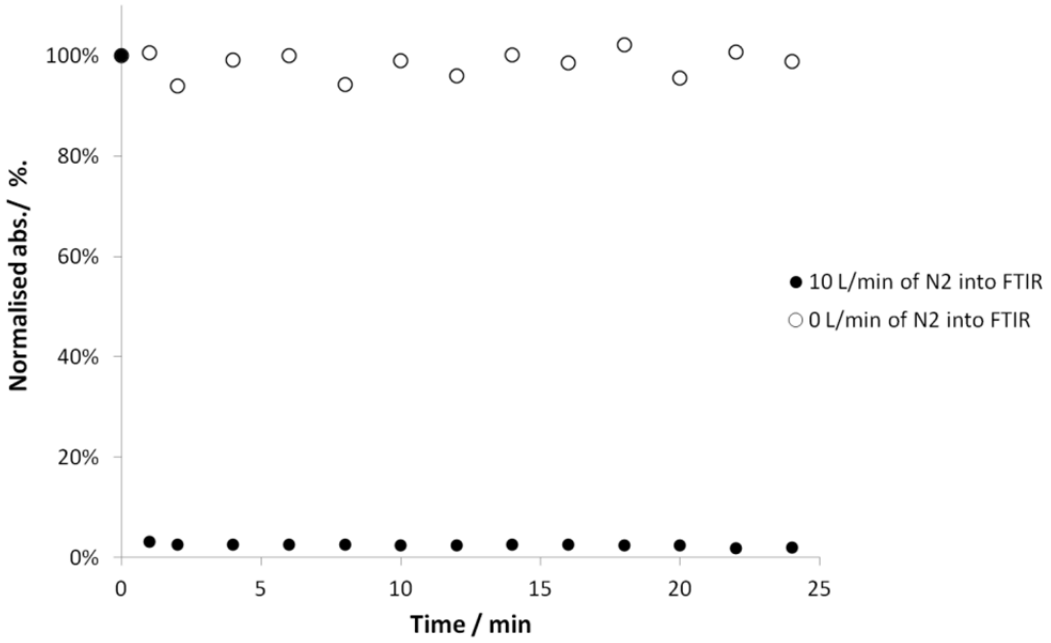

Figure 4-3 Figure 2 Depletion-assay performed for 25h, N_2 flow 10L/min, CO_2 absorbance measured 2360 cm^{-1}

Results suggested that N_2-flux of 10Lmin^{-1} determined both signal stability and less CO_2 contamination. For all these reasons 10 Lmin^{-1} has been assumed as a reference parameter.

4.3. Gas-cell optimization

It is conventionally agreed [3] that well performing gas-cell for FTIR measurements, carried out in gas phase, should exhibit:

an high transmission-rate in the mid infrared region;
null chemical interaction with species in contact with it (eg. moisture opacification)
an high mechanical resistance, because sealing can induce strong structural tensions.

In these experiments the gas-cells have been assembled by applying a couple of 16CF-viewport at a stainless steel T-junction, equipped with copper gaskets for sealing. At the end of assembly, gas-cells has been tested with an He-leak checker (Pifier, HL-T260), confirming the quality of sealing. Figure 4-4 reports an example of gas-cell.

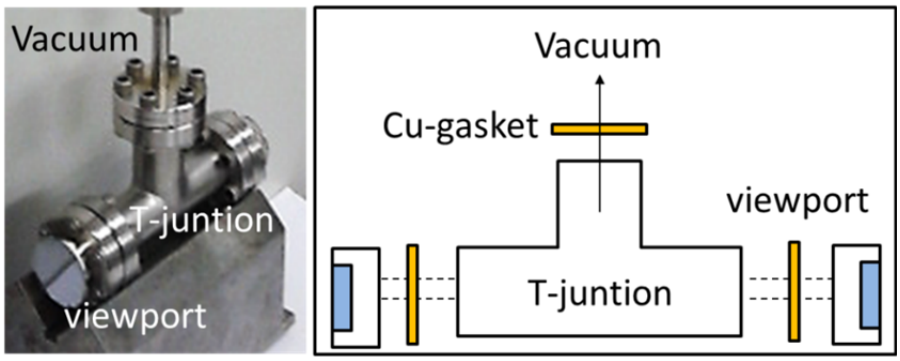

Figure 4-4 Gas cell equipped with two silicon viewports.

In order to find the more performing optical component for CO_2-detection, the transmission rate of three different viewports have been evaluated. Viewports consisted of silicon, glass and CaF_2 respectively. In this experiment FTIR instrumentation has been set to work in transmittance optical mode within the mid infrared.

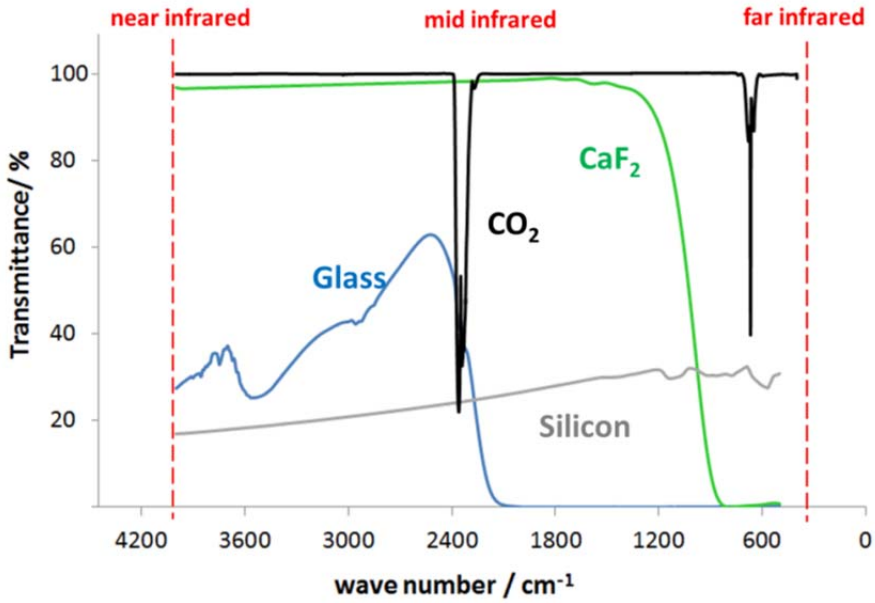

Figure 4-5 Infrared behaviours of viewports:(green) CaF_2, (blue) glass and (grey) silicon

Figure 4-5 reports the behaviour of each viewport. Looking at the plot one can notice that silicon shows a low and constant transmission rate (30% of Transmittance) across the mid and far infrared. On the contrary, glass has a better transmission rate (60-40 $T_{\%}$) in the mid infrared, but unfortunately it cuts off partially the peak of CO_2. Differently, CaF_2 exhibits a higher transmission rate across a wide range of mid infrared region (4000-1200

cm^{-1}). According to these results CaF_2-viewports have been assumed as the component of choice for the assembly of gas-cell.

4.4. FTIR validation

The FITR instrumentation has been calibrated by coupling it with a vacuum apparatus equipped with CO_2 reservoir.

A scheme of the vacuum apparatus is sketched in Figure 4-6. The gas-cell, positioned in the FTIR apparatus, has been connected to the pumping unit by using an isolating valve. The pumping unit consisted of a rotary vane pump and turbomolecular pump connected in series. A CO_2-reservoir has been connected to the system by using a dosing valve. Finally in order to measure CO_2-pressure, a full range vacuum gauge has been to connected to the system.

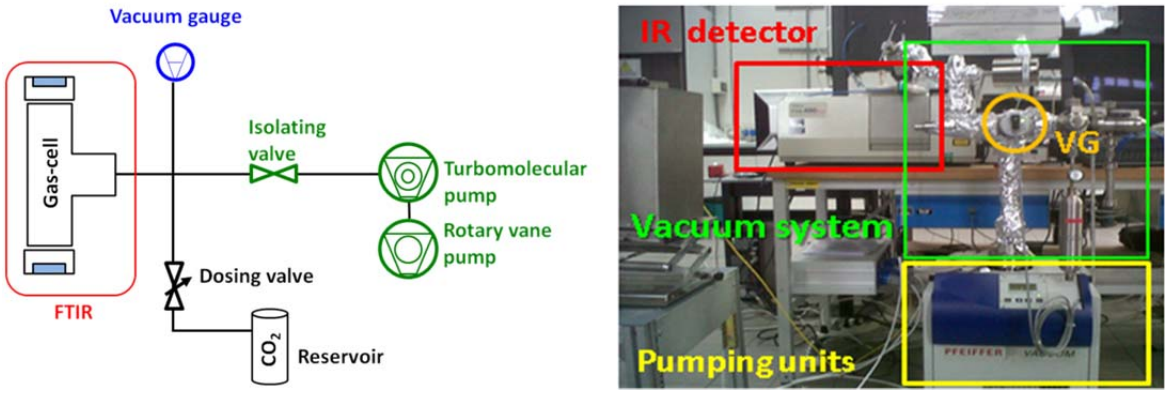

Figure 4-6 Vacuum apparatus

The calibration started by generating vacuum in the pipeline (10^{-8}mBar). Then, CO_2 pressure has been modulated by using the dosing valve while the full range vacuum gauge has been used to measure the pressure in the system.

CO_2 has been revealed by the FTIR apparatus, which was set to work in absorbance optical mode with a spectral resolution of $4cm^{-1}$ and recording 32 scans, which ranged from 4000 cm^{-1} to 500 cm^{-1} (mid infrared). The chemical composition of the atmosphere along the IR-path has been controlled by fluxing N_2. In the end, temperature (36.4°) has been monitored by a thermocouple inserted into the optical chamber.

According to the ideal gas law, CO_2-pressures have been converted into concentrations ($molL^{-1}$).

Figure 4-7 reports the calibration curve obtained by plotting the concentration of CO_2 versus its absorbance at 2360 cm^{-1} (asymmetric stretching of CO_2). Looking on the plot one can notice that the instrumental response exhibited an high sensitivity (102 $UmolL^{-1}$) and an high linearity (R^2=0.998) within a wide dynamic range (10^{-8}-10^{-3} M).

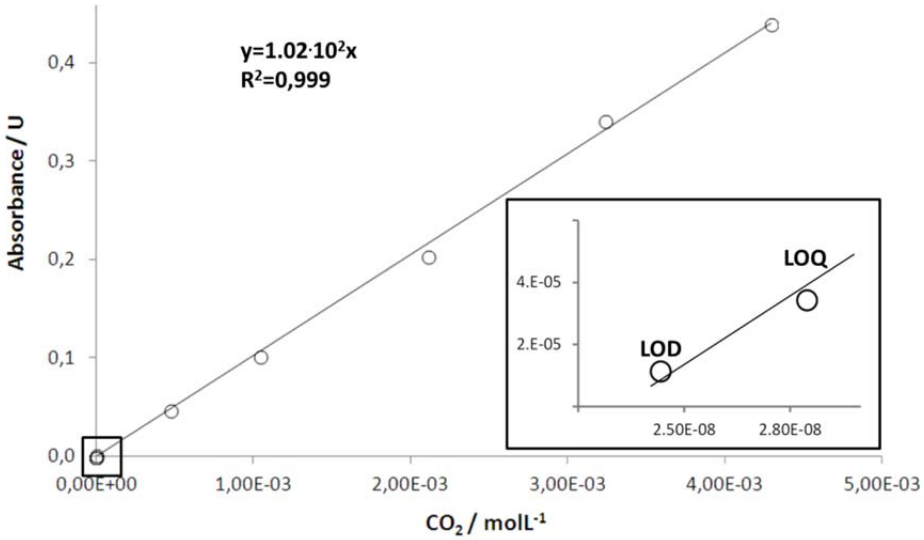

Figure 4-7 Calibration curve. CO_2 absorbance measured at 2360 cm^{-1}

According to literature [4], Limit of Detection (LOD) and Limit of Quantification (LOQ) are defined as the content of analyte revealed with S/N ratios equal to 3 and 10 respectively. Figure 4-8 reports three FTIR spectra of CO_2 characterised by S/N ratios equal to 0, 3 and 10. These results have been found useful to assess the LOD and LOQ, which were approximately equal to $2.4 \cdot 10^{-8}$M and $2.8 \cdot 10^{-8}$M.

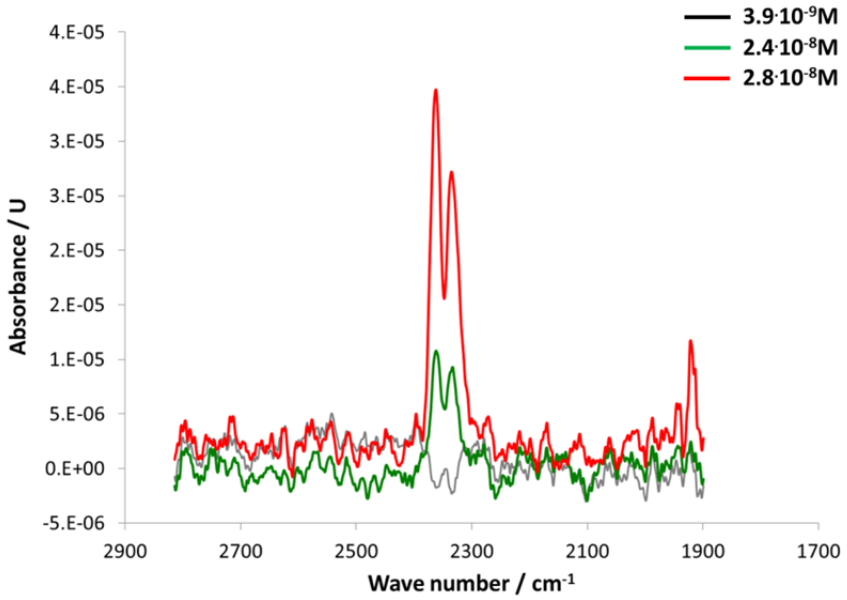

Figure 4-8 LOD (green) and LOQ (red) assessing.

In order to assess the reproducibility and the stability of the analytical method ten measurements have been performed at four different concentration of CO_2 that ranged from 10-8 M to 10-5 M. Table 4-1 reports the experimental results.

Table 4-1Data summary of the reproducibility assessment. Ten measurements at different concentration of CO_2

CO_2 concentration / molL^{-1}	Average Abs / U	Standard Deviation Abs / U	Coef. of variation / %
$3.1 \cdot 10^{-8}$	$7.7 \cdot 10^{-5}$	$1 \cdot 10^{-5}$	13%
$2.8 \cdot 10^{-7}$	$6.6 \cdot 10^{-4}$	$6 \cdot 10^{-5}$	11%
$2.7 \cdot 10^{-6}$	$3.2 \cdot 10^{-3}$	$7 \cdot 10^{-5}$	2%
$2.6 \cdot 10^{-5}$	$9.0 \cdot 10^{-3}$	$2 \cdot 10^{-4}$	2%

According to literature [5], that considers a coefficient of variation (CV) lower than 20% a well reproducible measurement, looking at Table 4-1 it could be noted that the reproducibility stabilised around a CV value approximately equal to 2% for higher CO_2 concentrations and it slightly decreased by lowering CO_2 concentration. A threshold value around 10^{-6} molL^{-1} has been assessed as the analytical condition at which the system started to be less reproducible. However the CV never exceeded the limit, represented by 20% of CV, and therefore it should be considered as an analytical method with a stabile response within a wide dynamic range.

Summarising, the analytical protocol must be considered as a validated analytical method, characterised by a good sensitivity, linearity and stability.

4.5. Reference

1. J. Nösberger, S. Long, R.J. Norby, M. Stitt, G. R. Hendrey, H. Blum. Managed Ecosystems and CO_2, 186 (2006) 22-25pp
2. J. Ehleringer, C. S. Cook. Plant Cell & Environment (1980), vol. 3, Issue 6, pp 479–482,
3. B. C. Smith; Fundamentals of Fourier Transform Infrared Spectroscopy (2011), pp154-170
4. De Bièvre,Helmut Günzle. Measurement Uncertainty in Chemical Analysis (2003),pp250-260
5. Pradip Kumar Sahu. Research Methodology: A Guide for Researchers (2013), pp 216-217

Chapter 5

CO_2 evolution, resting experiment

5.1. Abstract

This paragraph describes experiments performed on full Li-ion cells, under resting condition. The electrochemical cell has been assembled following the procedure described in the paragraph 1.1. For this experiment Al/$LiCoO_2$, Cu/graphite and Li electrodes have been configured as working (We) counter (Ce) and reference (Re) electrodes, respectively. Electrochemical impedance spectroscopy (EIS) measurements have been performed every two hours, to reveal changes in the cell components at different stages of the experiment.

CO_2 time evolution and voltage variation have been monitored by using FTIR-spectroscope (Jasco, 580-plus) and potentiostat (VMP-3, BioLogic). The experimental apparatus has been configured by connecting the gas cell of the FTIR to the Li-ion device, as sketched in Figure ii-1.

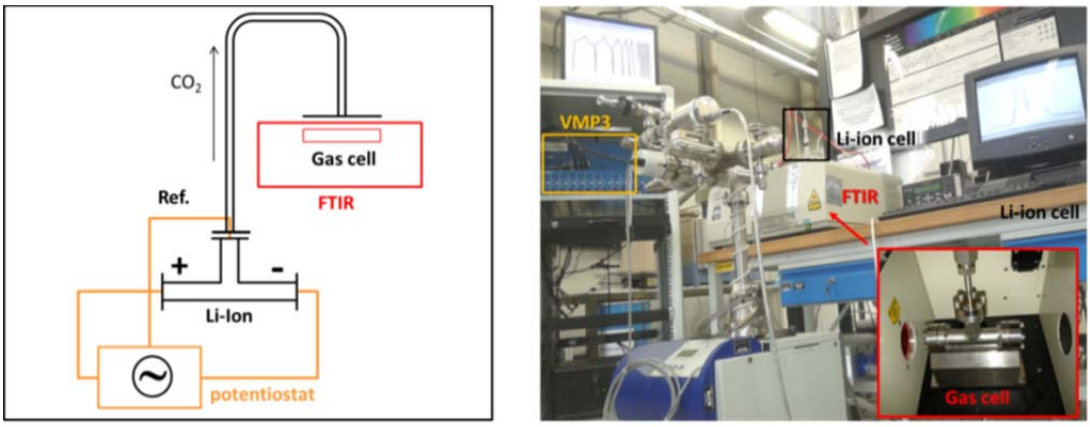

Figure 5-1 Scheme of the experimental setup for resting experiments

5.2. FTIR/Voltage measurements

A representative example of FTIR/Voltage measurements, carried out on a full Li-ion cell, has been reported in Figure 5-2. The electrochemical investigation has been performed by measuring separately the potential difference between both We and Ce versus Re, in open circuit condition. The whole cell voltage has been calculated as the potential difference between We/Re and Ce/Re electrode couples. FTIR spectroscope has been set to work in absorbance optical mode, revealing CO_2 at 2360 cm^{-1}.

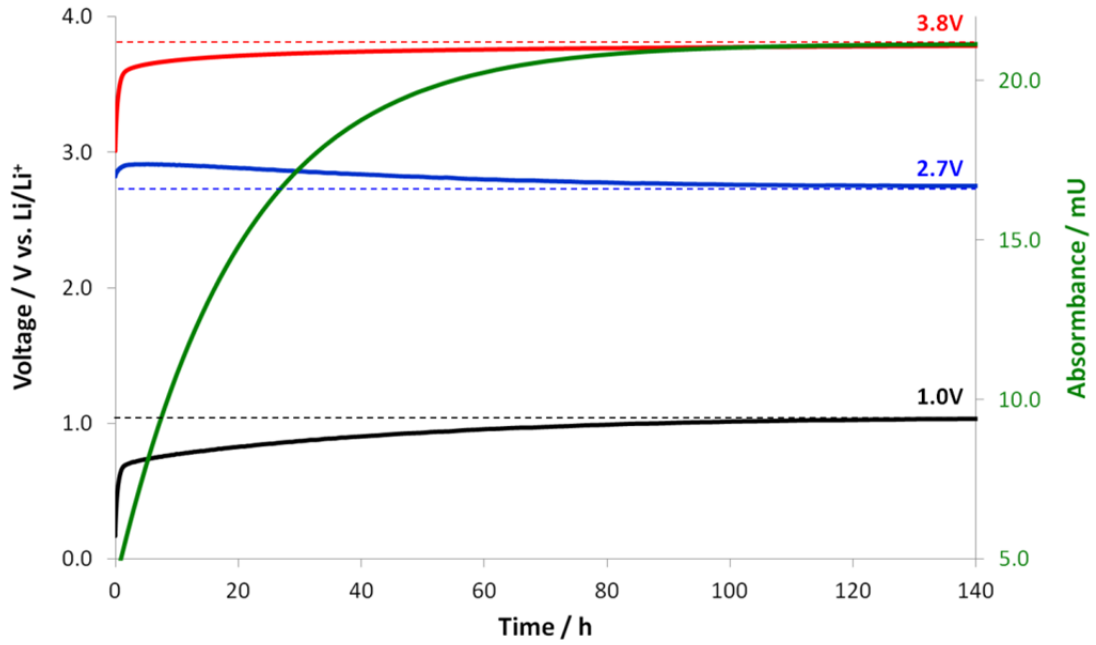

Figure 5-2 Behaviour of a full Li-Ion cell (C/Lp30/$LiCoO_2$) under resting condition, (•-green) CO_2 absorbance measured at 2360cm^{-1}, (•-red) We/Re-potential, (•-blue) Ce/Re-potential, (•-black) cell-Voltage. OCV measurements

Results showed that as soon as the cell was assembled, both We/Re and Ce/Re couples exhibited similar potential differences, which have led to a cell voltage of approximately 0.15V vs. Li/Li$^+$. Looking at the cell voltage profile, one can notice that it increased quickly during the first hour and then stabilised, reaching a plateau at 1.0V vs Li/Li$^+$. In particular, during the first hour of resting both We and Ce exhibited a potential increase, however by prolonging the experiment Ce started to reduce its potential. At the end of resting We and Ce stabilised around 3.8V and 2.7 V vs Li/Li$^+$, which are values close to the electrode potential of an operative cell under resting condition. Thus one can conclude that the stabilization of the cell voltage represent the macroscopic expression of phenomena aimed at stabilising the electrode/electrolyte interfaces

Moreover, a positive voltage enhancement ($\Delta E > 0$) should be considered as a thermodynamically favoured process and thus Li-ion cell must be deemed as redox system which is reacting spontaneously ($\Delta G < 0$). In particular, the chemical contact between the electrodes and the electrolyte determines a weak chemical instability, inducing electron transfer processes, which resulted from the electrodes polarisation.

Additional evaluations might be done taking in to account the Nerst equation, which expresses the relationship between redox reactions and potential measurements. In first approximation it possible to summarise that oxidative processes determine a voltage enhancement, whereas reductions should lead to a voltage decrease. From Figure 5-2 ie evident that oxidations and reductions occurred at We/electrolyte and Ce/electrolyte

interfaces, respectively. Moreover, the higher potential increase due to electrolyte oxidations, represent the driving force of the whole stabilization processes. A redox
FTIR experiments confirmed that CO_2 is produced in the cell as results of oxidation processes. Its time evolution has been found similar to the voltage profile. However, a time delay between voltage increase and the CO_2 evolution has been observed. It could be explained by assuming a sort of induction time approximately 1h, during which decomposition processes generated some intermediates, which further reactions produced CO_2 in the cell. On the contrary, time delay cannot be explained by diffusion phenomena, because according to CO_2 mass diffusivity (0.139 cm^2s^{-1}) CO_2 should expand into the head space of the cell (20ml) in few minutes.

5.3. Parity plot

In order to verify a correlation between the cell-voltage and CO_2 evolution a parity-plot has been done. Parity plot is the method of choice to identify a correlation between couples of aleatory variables. The algorithm consists of a linear regression between variables under investigation. Figure 5-3 reports two parity plots obtained by reporting in graph electrode potential versus CO_2 absorbance. In particular, Figure 5-3a and Figure 5-3b report respectively the parity plots referred to We and Ce. Comparing the correlation parameter (R^2) obtained by using least square method, one can notice a linear correlation domain between We-potential and CO_2 evolution. On the contrary no correlation has been found between Ce and CO_2 evolution.

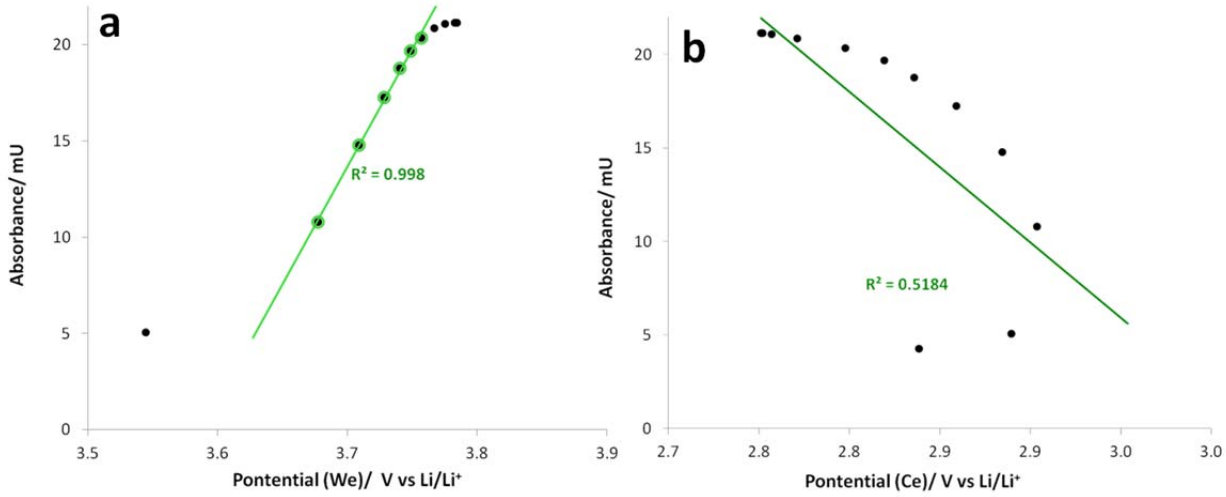

Figure 5-3. (a) parity plot We potential vs. CO_2 absorbance.(b) parity plot Ce potential vs. CO_2 absorbance (2360cm^{-1}).

Figure 5-4 is a parity plot, obtained by reporting in graph the cell voltage versus CO_2 pressure, which has been calculated according to the calibration experiment reported into chapter 4.

The Plot shows three stage of the experiment. The first stage could be considered as an induction step, during which side reaction occurred leading to a strong voltage increase and a weak evolution of CO_2. Prolonging the experiment, parity plots a linear correlation domain between 0.6V and 0.9V has been identified. This stage of the experiment has been called “oxidative degradation stage” ant it ranged from 1 h to 50 h of resting. The linear domain has been interpolated by using least square method. The fitting revealed a good correlation parameter (R^2=0.990). Moreover, the slope coefficient (0,018barV^{-1}) revealed that the electrolyte oxidation induced a pressure build-up of approximately 0.018mBar every millivolt of voltage increase. The experiment concluded with the stabilization stage, during which the correlation between variables has been lost. An explanation might consider the voltage stabilization as the results of electrodes passivation, which reduced the CO_2 evolution by preventing further redox reactions.

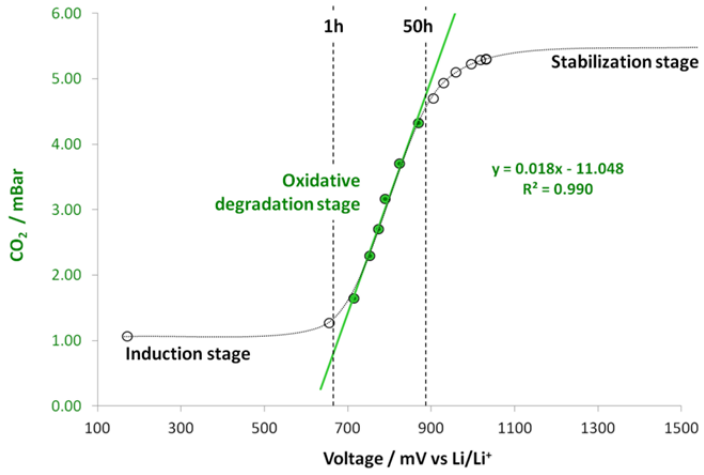

Figure 5-4 Cell voltage of full Li-ion cell (C/Lp30/$LiCoO_2$) vs. FTIR parity plot

5.4. Kinetic evaluations

In order to formalise a mathematical expression for CO_2 time evolution, the first derivative of CO_2 concentration has been calculated in the time domain and then reported in graph versus the concentration of CO_2, Figure 5-5. As expected for a first order kinetic regime, the data revealed a linear trend. The results have been fit with the least square method,

finding a rate constant approximately equal to 13±0.01 ms^{-1}. Summarising, the time evolution of CO_2 speed down linearly by time.

Although CO_2 is the end point of server side reactions (see paragraph 1.2), the unitary correlation factor revealed that the whole kinetic is dominated by one phenomenon, which represents the rate determining step. In particular one can speculate that the passivation of the electrode surface might have reduced the oxidation of the electrolyte, avoiding progressively the CO_2 evolution.

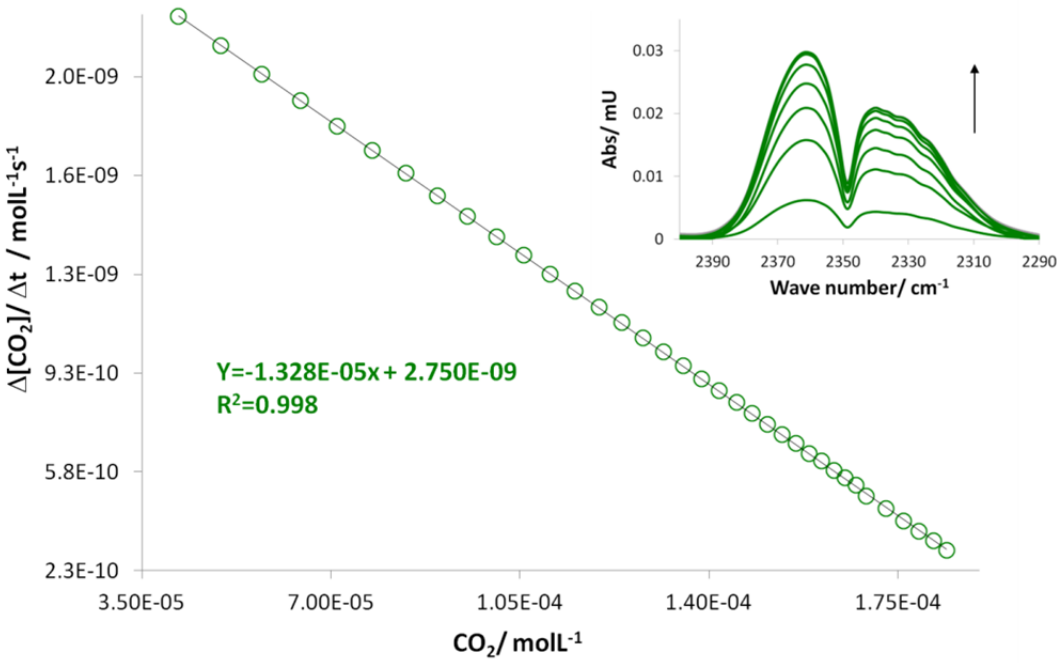

Figure 5-5 Kinetic regression of CO_2 evolution within full Li-ion cell (C/Lp30/$LiCoO_2$) under resting.

5.5. Electrochemical impedance spectroscopy

EIS analyses have been performed during resting, by applying a bias voltage of ±5mV with a sweep of frequency, which ranged from 100 kHz to 50 mHz, and each spectrum has been recorded with a sampling rate of six points per decade.

During resting experiment both We and Ce responded similarly to EIS and therefore Ce has not been reported. Figure 5-6 reports the spectra recorded on We at different stage of resting experiment. Looking on the plot, one can notice weak alterations occurred at electrode/electrolyte interface.

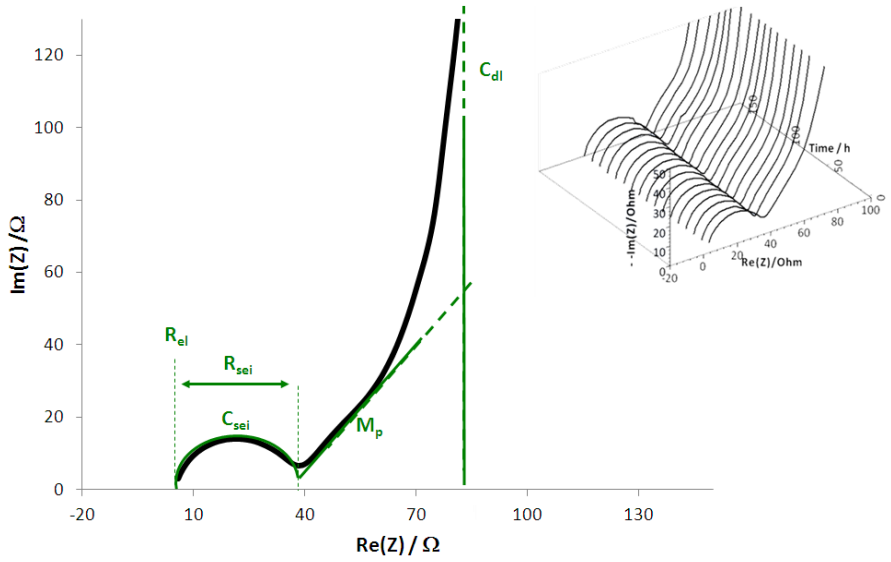

Figure 5-6 EIS experiments performed o full Li-ion cell (C/Lp30/$LiCoO_2$) during resting. Bias voltage 5mV, frequency range 100kHz-50mHz.

All of the spectra recorded on the We consist of a semicircle in the high frequency region (100KHz), followed by two distinct straight lines, which are defined in the mid (100Hz) and low (1Hz) frequency domains. The first intercept of the semicircle and its diameter represent the ionic resistances due to the electrolyte ($\mathbf{R_{el}}$) and SEI ($\mathbf{R_{sei}}$), respectively. The circular shape of the spectrum originates from the dipolar relaxation occurred to SEI, which responds with a pure imaginary contribute to high frequency impedance, behaving as a non-ideal capacitor ($\mathbf{C_{sei}}$). According to literature [1], the linear domain (unitary slope) in the mid frequency range has been attributed to the diffusion resistance ($\mathbf{M_p}$) of ions across the pores of the electrode. The vertical asymptote in the low frequency region refers to the dipolar relaxation of the electrolyte, which results from an additional imaginary contribute to the whole electrode impedance in the low frequency domain. According to the Gouy Chapman model [2], it could be considered as a non-ideal capacitor ($\mathbf{C_{db}}$).

Considering all these evidences, one can that We (and similarly Ce) behaved as a blocking electrodes, which neither accept from, nor supply to, ions from the electrolyte.

Although EIS provide qualitative information about the electrochemical behaviour of cell components, the main output of this technique is the quantification of each resistance and capacitance presents within the electrochemical system. To do so, each spectrum should be interpolated by using a proper equivalent circuit. The spectra of blocking and electrodes have interpolated by using "$\mathbf{R_{el}}$+$\mathbf{C_{sei}}$/$\mathbf{R_{sei}}$+$\mathbf{M_p}$+$\mathbf{C_{dl}}$" and equivalent circuit respectively. The schemes of these equivalent circuits have been sketched in Figure 5-7.

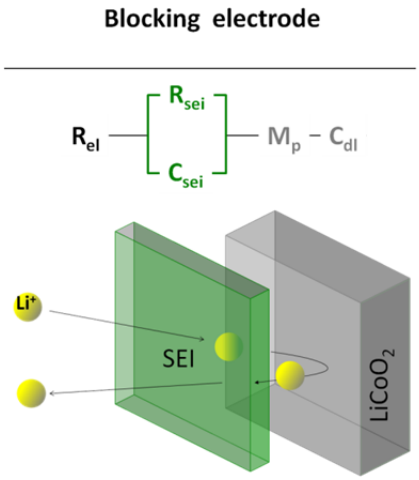

Figure 5-7 electrical description of the equivalent circuit related to blocking electrode

Figure 5-8 reports the time evolution of both $\mathbf{R_{el}}$ and $\mathbf{C_{dl}}$ parameter. Looking at the plot, one can notice that both ionic resistance and double layer capacitance stabilised around average values of 5.7±0.2 Ωcm^{-2} and 0.61±0.04 $mFcm^{-2}$, respectively. In spite of electrolyte resistance which immediately stabilized, double layer capacitance needed approximately thirty hours to reach a complete stabilisation.

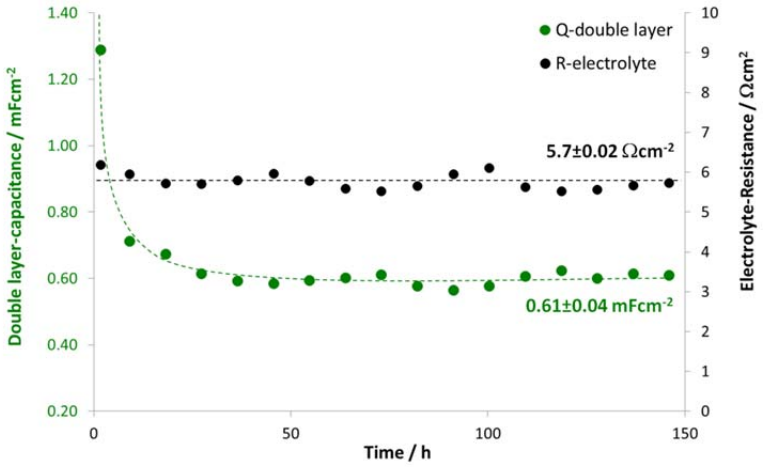

Figure 5-8 Time evolution of: (●) double layer capacitance, and (●) electrolyte resistance.

The capacitance decrease could be explained considering that side reactions depleted the interface of cations. In particular, the charge density of interface could by estimated approximating $\Delta\boldsymbol{\varphi}$ (surface potential) with the We potential and taking in to account the following equation:

$$C_{dl} = \frac{q}{\Delta\varphi} \sim \frac{q}{\Delta E}$$

where, q represents the interface charge density and $\Delta\varphi$ is the surface-potential. Figure 5-9 reports the We potentials and the charge density of We/electrolyte interface. How it could be noted, the oxidations of the electrolyte increased the WE potentials and consumed partially Li^+ cations, which are probably embedded into the growing SEI. Summarising, the oxidative decomposition of the electrolyte lead to an average charge densities of 2.3±0.1 $mCcm^{-2}$.

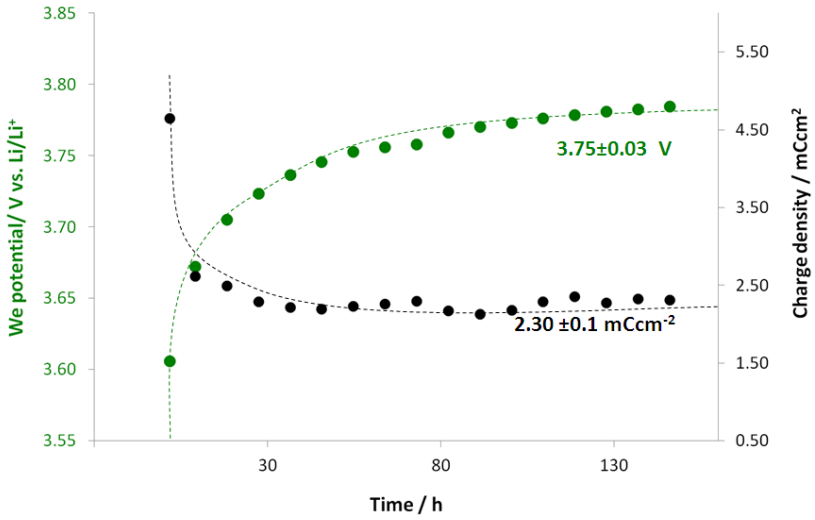

Figure 5-9 Time evolution of: (●) cell-voltage, and (●) double layer capacitance.

Figure 5-10 reports resistance and capacitance of passivating layers (SEI). Contrary to electrolyte, the SEI revealed a linear increase in both resistance and capacitance.

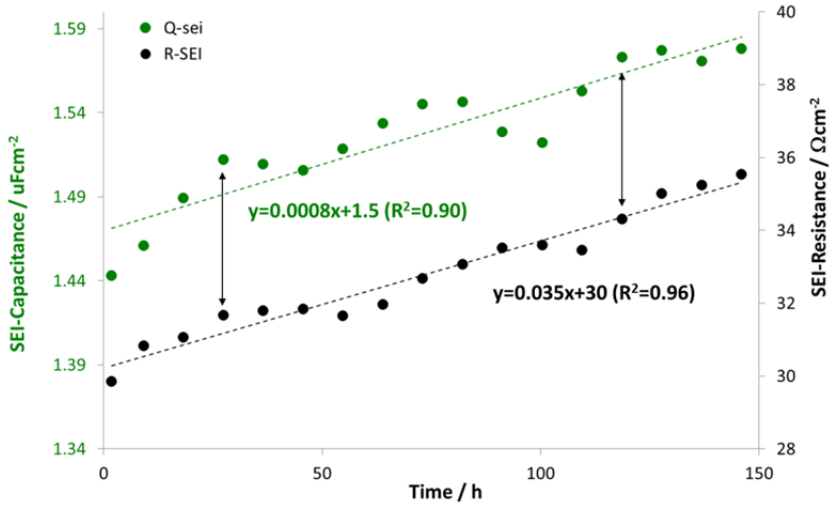

Figure 5-10 Time evolution of: (●) SEI capacitance, and (●) SEI resistance

Taking into account the second Ohm's law (**eq.4**) and the fundamental equation of capacitor (**eq.5**):

$R_{sei} = \rho \cdot {}^{t}/_{A}$ **eq.4** ; $C_{sei} = \varepsilon_0 \varepsilon_r \cdot {}^{A}/_{t}$ **eq5**

Where:

R_{sei}: SEI resistance

C_{sei}: SEI capacitance

t: the thickness of SEI

A: electrode surface covered by passivation layers.

$\boldsymbol{\rho}$: specific resistance of each passivation layer

$\boldsymbol{\varepsilon_0}$: vacuum permittivity

$\boldsymbol{\varepsilon_r}$: relative permittivity of SEI

It is not reasonable to describe the linear increase of **R_{sei}** as an increase of **t**, because the higher is **t**, the lower **C_{sei}**, whereas **C_{sei}** has been increasing during the resting.

Although both equations are not suitable as macroscopic descriptor, they could help in the understanding of microscopic phenomena, whose synergy determines the electrochemical behaviour revealed by EIS.

According to **eq.4** and **eq.5**, both transport and dipolar relaxation properties of SEI, lead to describe each passivated grain as a micro R/C circuit, where R and C elements are configured in parallel. Moreover, each passivated grain should be considered as connected in parallel to the others, thanks to cobalt conduction bands, that provide an electronic contact between each passivated grains.

Summarising, the electrode surface could be described as an equivalent circuit, which consist of R/C elements connected in parallel, as described Figure 5-11.

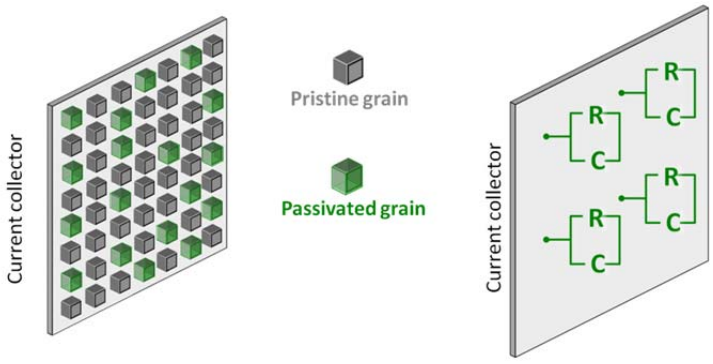

Figure 5-11 Mosaic structure of the electrode surface during passivation

Taking in to account that the inner part of SEI layer consists of inorganic species [3], phase transition of and chemical alteration occurred to SEI might induced similar effects on both capacity and resistances, by increasing both relative permittivity and specific resistance of the SEI layers.

All these speculations lead to consider the SEI growing as a random phenomenon, which occurred on the electrode surface. In other words, although each local passivation contributed to the enhancement of the cell voltage, each passivating grain should be considered as a independent chemical system.
For all these reasons EIS and voltage measurements could be considered as good descriptors for microscopic and macroscopic phenomena that occurred to the cell during resting.

5.6. SEM/EDX ex situ characterizations

Ex-situ evaluations have been performed on We before and after resting, by using electron scanning microscope (SEM) equipped with the EDX probe (energy dispersive X-ray spectroscope). SEM has been set to work in back scattering electron mode, in order to have micrographs sensitive to atomic weight. The rationale of this approach is based on the better scattering efficiency that characterises heavy atoms. In this technique, atoms with high atomic number scatter electrons with high efficiency, leading to a bright image of the grain. On the contrary, light atoms make grains darker because of their lower scattering efficiency.
Micrographs reported in Figure 5-12 refer to We before (Figure 5-12-a) and after resting (Figure 5-12-b). Before resting, the $LiCoO_2$ electrode appeared bright with occasional dark spots which are probably residues of the organic binder (polyvinylidene fluoride, PVdF). On the contrary the same electrode after resting revealed a lot of dark spots randomly distributed on the electrode surface. In particular by magnifying the micrograph in Figure 5-12b, organic coatings have been observed on the surface of the grains.

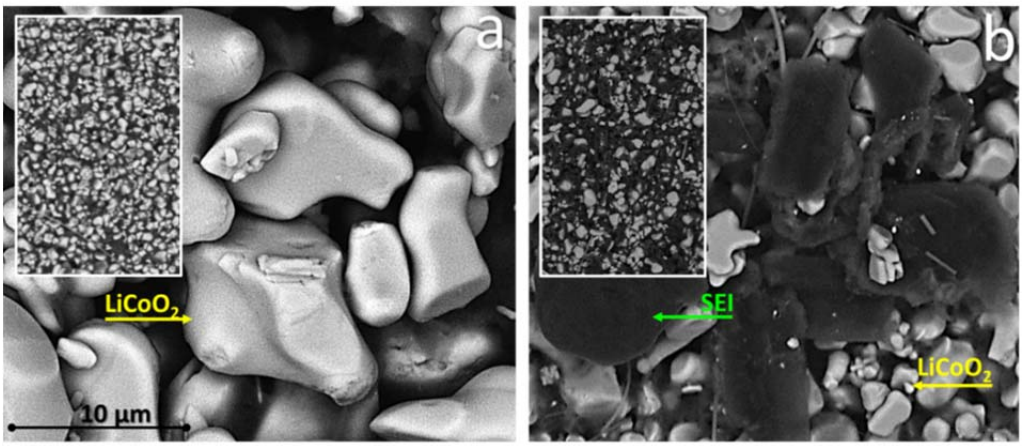

Figure 5-12 $LiCoO_2$ electrodes: (a) electrode before resting , (b) electrode after resting. Micrographs obtained by secondary electrons

Contrary to We that consists of $LiCoO_2$, Ce has been found not suitable for this kind of investigation because both electrode and passivation layers consist of carbon atoms and therefore back scattering did not highlight significant difference after resting.

However, one can conclude that the morphological alteration which occurred at We could be a representative example of phenomena, occurred during resting.

Figure 5-13 reports EDX analysis, performed by focusing the electron beam on a single grain of the We. EDX measurements performed revealed that the organic coatings consisted of fluorine, phosphorus and carbon atoms. These evidences suggest that the organic coating probably resulted from electrode degradation, whose products are embedded on the electrode surface.

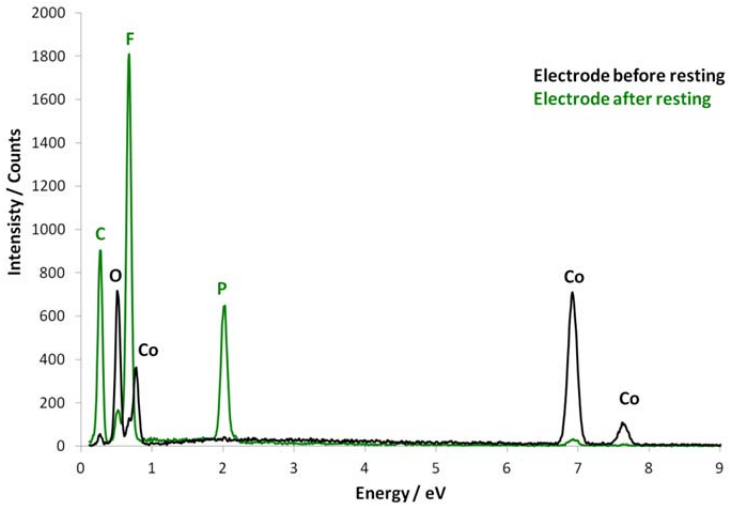

Figure 5-13 EDX spectra: (black) electrode before resting and (green) electrode after resting.

Although grains have been covered by SEI layers, EDX has been found sensitive enough to reveals weak signals of Co atoms, which came from the bottom of passivation layers. By normalising the Co signals measured after and before resting, one can calculate that SEI layers induced an attenuation of the EDX beam equal to 96%. According to the penetration depth of the electron-beam (10-100nm) one can hypothesis that SEI layer was few hundreds nanometers thick [4].

5.7. Conclusion

Resting experiments revealed that redox side reactions spontaneously occurred at the electrode/electrolyte interfaces. These reactions lead to CO_2 evolution, whose time evolution follow a kinetic regime of the first order with a rate constant of $13 \cdot ms^{-1}$. Moreover, the strong potential increase measured between We and Re leads to speculate that oxidation occurred preferentially at We/electrolyte interface and therefore CO_2 is probably generated at the positive pole (Al/LiCoO2 electrode), as schematised in Figure 5-14.

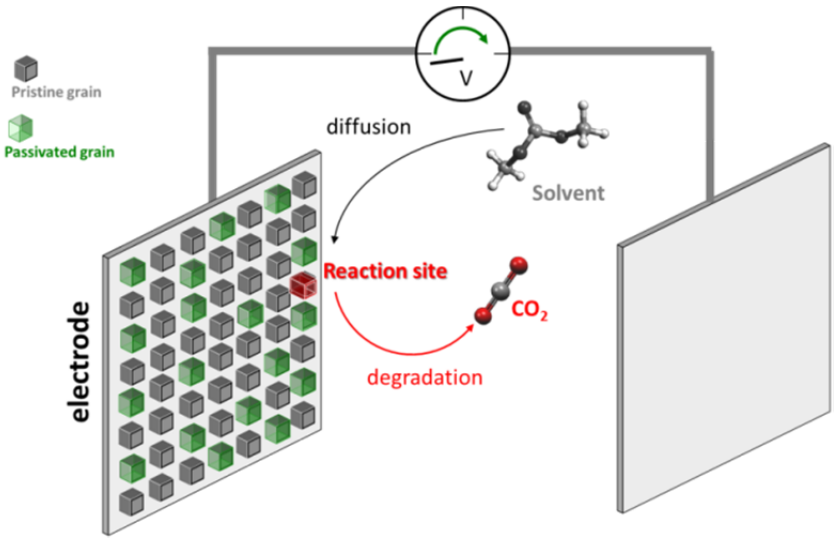

Figure 5-14 Mechanism of degradation at the We/electrolyte interface

EIS measurements and SEM/EDX characterizations revealed a complex mechanism of passivation, which leads to chemical and morphological alterations of the electrode surfaces. These evidences lead to consider passivation as an extremely localised process, which generated protecting coatings on the electrode grains. As depicted in Figure 5-15, passivation should be considered as a series of processes that lead to a mosaic structure of the electrode surface.

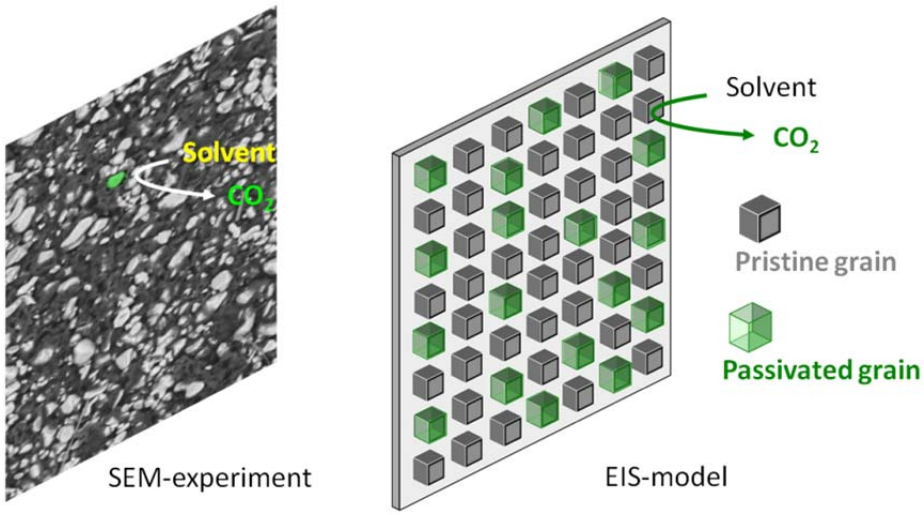

Figure 5-15 Comparison between SEM evidences and EIS model

Although electrochemical evidences revealed that side reactions took place immediately after cell assembly, CO_2 started to pressurise the cell with a time delay of approximately 1h. During the oxidative degradation stage experiments revealed that CO_2 pressurised the cell with a rate of 0.018 mBar per millivolt.

In order to assess the risk concerning the Li-ion cell storage and logistic electrolyte degradation pressurization should be scaled up, because an increase of the electrode surface must lead to an increase of the electrolyte degradation. Comparing an electrode surface of approximately $100cm^2$ with We implemented in the cell model (0.785cm2), one can speculate about pressurization rate of approximately $2.3mBarmV^{-1}$, which might lead to a pressurisation of few Bar over the atmospheric pressure. Although the scale up calculation must be take into account with caution, results emphasise that pressurisation under resting condition might be a relevant safety issue for Li-ion cell device, especially whether they will stored for a long time at RT or transported exposing them to strong thermal excursion.

5.8. Reference

1. Digby D. Macdonald Electrochimica Acta 51 (2006), 1376–1388
2. Electrochemistry Di P.H. Riege pp 59-61 Chapman & Hall (New York, 1994)
3. L. G. Hector, Jr Hong Li, Stephen J. Harris J. Am. Chem. Soc. 2012, 134, 15476−15487

4. H.Li Zhang, F. Li, C. Liu, Jun Tan, j. Phys. Chem. B 2005, 109, 22205 22211

Chapter 6

CO_2 evolution, cycling experiment

6.1. Abstract

This paragraph describes experiments performed on full Li-Ion cell, under cycling conditions. The electrochemical cell has been assembled by following the procedure described in the paragraph 1.1. The device has been cycled by a potentiostat/galvanostat (VMP-3, BioLogic) and the CO_2 evolution has been monitored by using a FTIR-spectroscope (Jasco, 580-plus). EIS measurements have been performed, revealing changes in cell components at different stages of the experiment. The experimental apparatus has been configured by connecting the gas cell of the FTIR with the Li-ion device, as sketched in the Figure 6-1. Additional details about both electrochemical and FTIR protocols have been reported in chapter 3 and chapter 4, respectively.

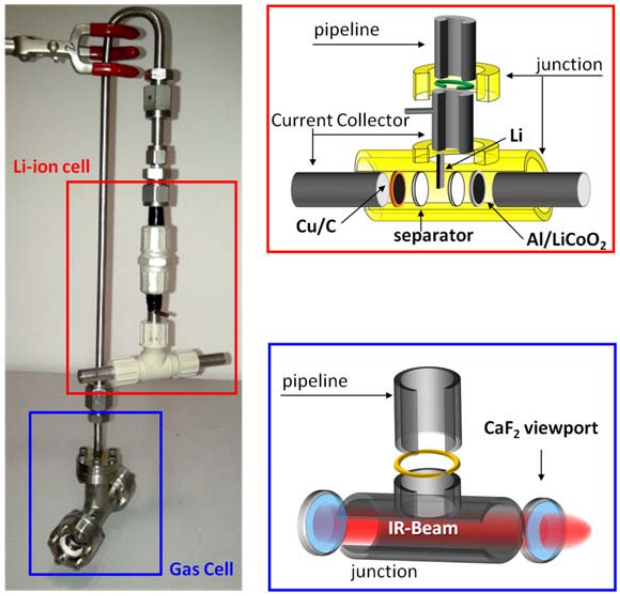

Figure 6-1 Scheme of Li-ion device coupled to Gas cell

6.2. FTIR/GPCL measurements

The Li-ion cell has been configured to use Al/$LiCoO_2$, Cu/graphite and Li as cathode, anode and reference electrodes, respectively. The electrochemical experiment consisted of a Galvanostatic Cycling with Potential Limitations (GCPL). The experiment has been divided in three main stages, which were OCV stabilisation, SEI Formation and Cycling. During the OCV stabilization, the VMP-3 apparatus has been set to work in potentiometric mode (infinite impedance among electrodes), each electrode potential has been measured as the potential difference between cathode (or anode) versus reference

electrode and the whole cell voltage has been calculated as the potential differences between cathode/reference and anode/reference couples. The formation cycles have been performed by using the VMP-3 apparatus in galvanostatic mode. The Li-ion cell has been charged and discharged at low C-rate for three cycles (C/10, 14.5mAg^{-1}). Both charge and discharge processes has been stopped when the cell voltage reached its upper and lower potential limits, fixed at 4.20V and 3.00V (vs. Li/Li^+), respectively. This stage of the experiment makes the electrodes suitable for intercalation/deintercalation processes and stabilised the cell by generating passivation layers (SEI, solid electrolyte interface) on the electrodes surfaces.

Cycling consisted of several charge/discharge processes, performed by cycling the cell within the same potential limits (3.00V-4.20V vs. Li/Li^+) and by increasing the C-rate up to C/5. This stage of the experimental is very useful to simulate at lab scale a Li-ion device under operation conditions.

FTIR apparatus has been set to work in absorbance optical mode, revealing CO_2 at 2360 cm^{-1}.

A representative example of FTIR-measurements performed on a Li-ion cell during the experiment has been reported in Figure 5-2. Where CO_2, cathode, anode and cell voltage have been reported in green, red, blue and black, respectively.

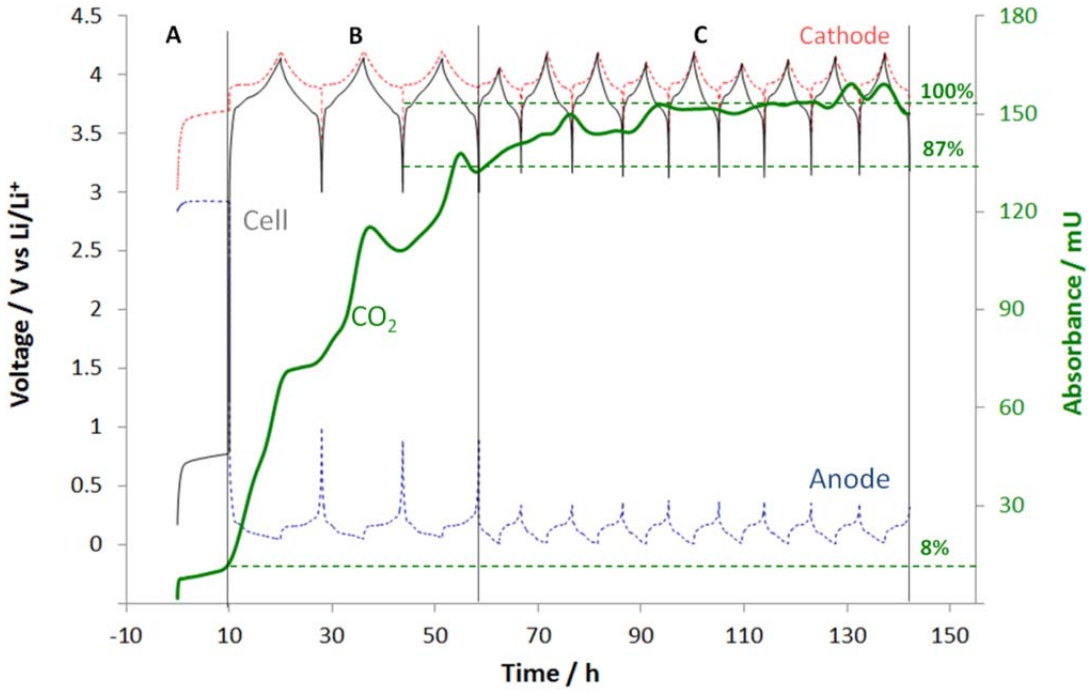

Figure 6-2 Behaviour of a full Li-Ion cell during OCV stabilization (A), SEI Formation (B) and Cycling (C). SEI Formation performed at C/10 and cycling performed at C/5. CO_2 absorbance measured at 2360cm^{-1}

Results highlighted that the cell have been producing CO_2 for all of the experiment, CO_2 diffused within the cell, reaching the FTIR gas cell, where a travelling infrared beam revealed it.

In particular, as soon as the cell has been assembled a little amount of CO_2 evolved spontaneously and it increased slightly during the OCV stabilization, as confirmed by resting experiment this CO_2 originated from spontanuos oxidation processes occurred at the cathode/electrolyte interfaces. Although CO_2 has been detected during the first stage of the experiment (OCV stabilization), the most relevant contribution to the final pressure build up is due to SEI-Formation steps, during which approximately 80% of the total CO_2 has been generated. An additional amount of CO_2 (10%) has been observed during cycling because of the dynamic nature of SEI layers, which occasional damages could have made the electrode surface accessible to the fresh electrolyte.

FTIR data-set has been interpolated whit a polynomial fitting, finding a mathematical expression for the baseline ($Y=-3.5\cdot10^{-1}+5.1x-4.8\cdot10^{-2}x^2+1.5\cdot10^{-4}x^3$). Data-set has been deconvolved by subtracting the baseline function and by using a Gaussian algorithm. Results have been reported in Figure 6-3.

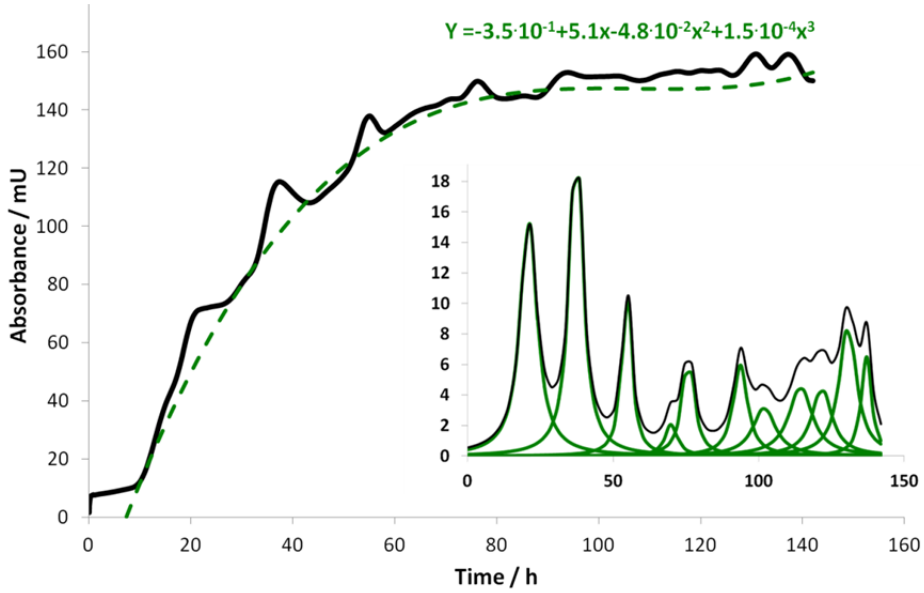

Figure 6-3 Baseline correction and deconvolution of the absorbance trace

By comparing deconvolved CO_2 peaks with the cell voltage trace, an interesting correlation has been found during the formation steps. As reported in Figure 6-4, the experiment revealed that CO_2 has been produced by the oxidation of the electrolyte during charge. CO_2 evolution slowed down when the cell reached its upper voltage limit (4.2V

versus Li/Li^+), and its signal decreased by discharging the cell voltage, probably because of its reductive decomposition.

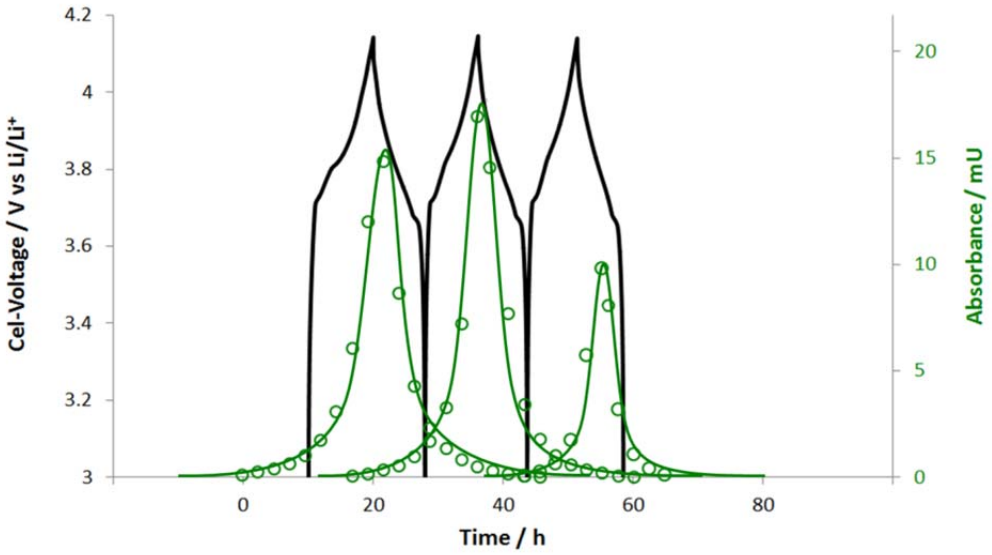

Figure 6-4 CO_2 absorbance versus cell voltage profile.

In order to confirm and assess the correlation already observed, a parity plot has been done for both charge and discharge processes. Figure 6-5 reports an example of parity plot, calculated for the charge/discharge cycle of the first SEI-Formation step. A linear correlation between CO_2-absorbance and cell voltage has been found in both cases (R^2>0.9).

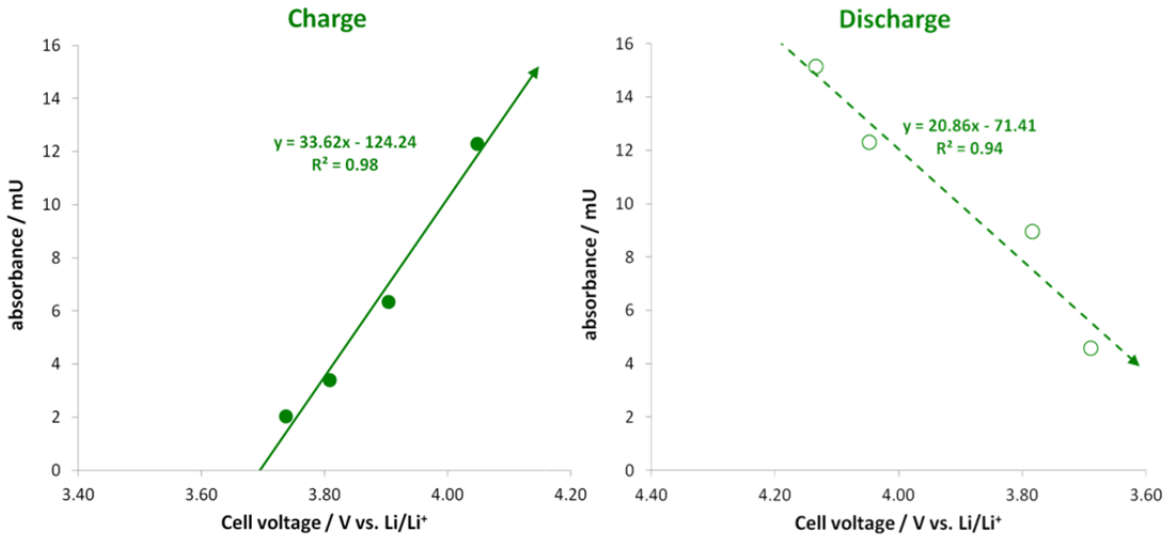

Figure 6-5 Parity plot of 1st formation cycle. Cell voltage vs. CO_2 absorbance.

All Results revealed that CO_2 has been produced by electrochemically controlled processes, which occurred particularly during charge.

Moreover, the amount of CO_2 generated by charging the cell is greater than what might be consumed during discharge.

6.3. Pressurization rate

Converting the absorbance of CO_2 into pressure (see paragraph 4.4) and calculating its first derivative in time domain, one can obtain the pressurization rate of the cell. This parameter might be plotted versus the cell capacity or cell voltage, highlighting the charge/discharge conditions, where pressurization and depressurization rate reach their maximum values. A representative example is reported in Figure 6-6, wherein the pressurization rate of the first formation cycle has been plotted versus cell-capacity and cell voltage.

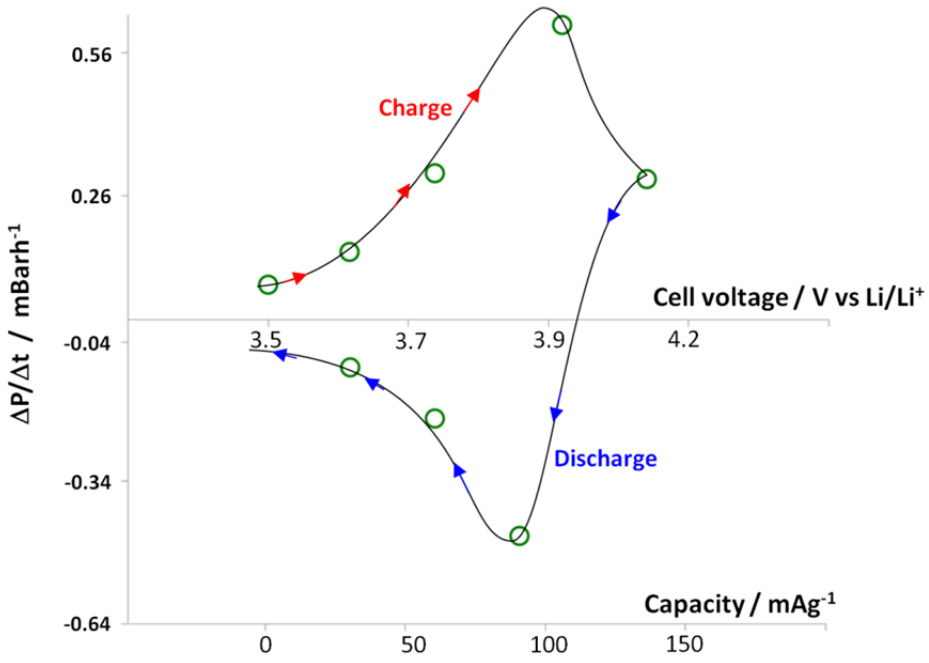

Figure 6-6 pressurization rate vs. capacity and cell voltage.

Evaluations confirm that charge and discharge processes have led to positive and negative pressurisation rate. In particular, the pressurization rate increased when the cell reach its operative voltage (3.8V vs. Li/Li^+). Approaching the upper potential limit (4.2V vs. Li/Li^+) pressurization rate decreased and it became negative (CO_2 consumption), when the cell started to be discharged.

In order to understand where CO_2 generation and consumption might have taken place, few aspects should be considered.

First of all, CO_2 has been generated by electrochemical dependent phenomena, which concerned the oxidation of the electrolyte. In particular, electron transfers from the electrolyte to an electrode should have occurred by charging the cell. Considering that charge induces electronic vacancies in the valence bands of the cathode, It's reasonable

to speculate that electrolyte oxidation should have occurred at cathode/electrolyte interface. On the contrary, anode electrons stored electrons into its conduction bands, making its surface active for reduction. Thus one can speculates that CO_2 could have been reduced at the anode/electrolyte interface.

The well known boundary conditions for faradic processes require that valence and conduction bands must have electronic states lower and higher than CO_2 HOMO and LUMO energetic levels, respectively. Moreover, the different populations of these electronic states are responsible for CO_2 generation and consumption rates. Thus one can conclude that charge and discharge depths determine the pressurization and depressurizations rates, respectively.

Although decomposition processes take place preferentially in overcharge (or overdischarge) conditions [1], pressurization rate revealed that CO_2 evolved quickly under operative condition (cell voltage 3.80V vs.Li/Li^+) and it slowed down approaching the voltage limits.

Concluding, CO_2 evolves preferentially during charge and it accumulates strongly when the cell reached its operative voltage (cell voltage 3.80V vs.Li/Li^+), because the anode is not active to consume efficiently CO_2. For all these reasons, 3.80V should not be longer considered as a safety operative condition for users, especially for cell characterised by wide electrode surfaces.

6.4. GCPL-EIS/FTIR experiments

Further evidences that support a correlation between the electrode side-chemistry and CO_2 evolution are offered by EIS-experiments. Measurements have been performed at different stages of the test protocol, revealing changes in the cell components. The analyses have been performed by applying a bias voltage of ±5mV with a sweep of frequency, which ranged from 100 kHz to 50 mHz and each spectrum has been recorded with a sampling rate of six points per decade.

Figure 6-7 reports a spectrum recorded on the pristine cathode. It consist of a semicircle in the high frequency region (100KHz), followed by two distinct straight lines, which are defined in the mid (100Hz) and low (1Hz) frequency domains. The first intercept of the semicircle and its diameter represent the ionic resistances due to the electrolyte ($\mathbf{R_{el}}$) and SEI ($\mathbf{R_{sei}}$), respectively. The circular shape of the spectrum originates from the dipolar relaxation occurred to SEI, which responds with a pure imaginary contribute to high frequency impedance, behaving as a non-ideal capacitor ($\mathbf{C_{sei}}$). According to literature (**ref**), the linear domain (unitary slope) in the mid frequency range has been attributed to

the diffusion resistance ($\mathbf{M_p}$) of ions across the pores of the electrode. The vertical asymptote in the low frequency region refers to the dipolar relaxation of the electrolyte, which results from an additional imaginary contribute to the whole electrode impedance in the low frequency domain. According to the Gouy Chapman model, it could be considered as a non-ideal capacitor ($\mathbf{C_{db}}$).

Considering all these evidences, one can concluded that the pristine cathode behaves as a blocking electrode, which neither accept from, nor supply to, ions from the electrolyte

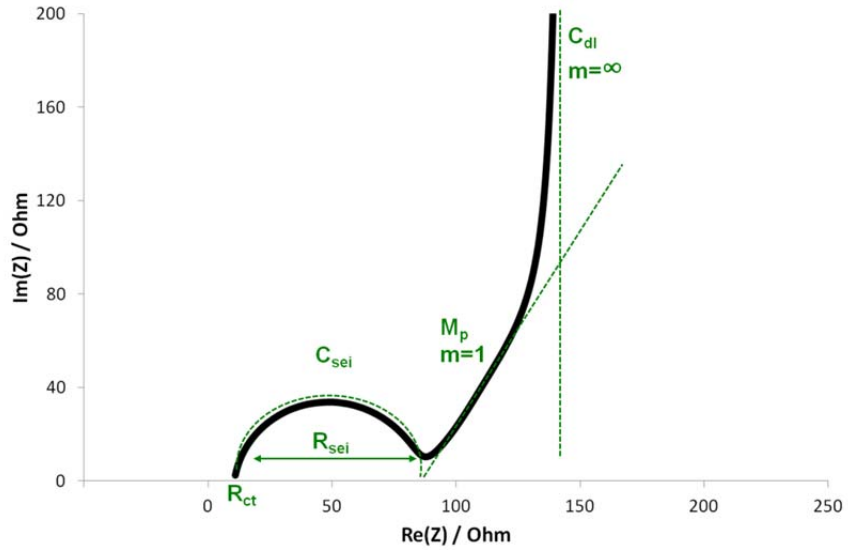

Figure 6-7 spectrum recorded on the pristine cathode. Bias voltage 5mV, frequency range 100kHz-50mHz.

Figure 6-8 is a spectrum recorded on the cathode at the end of the first formation cycle. It consists of two semicircle positioned in the high (100KHz) and low (1Hz) frequency regions.

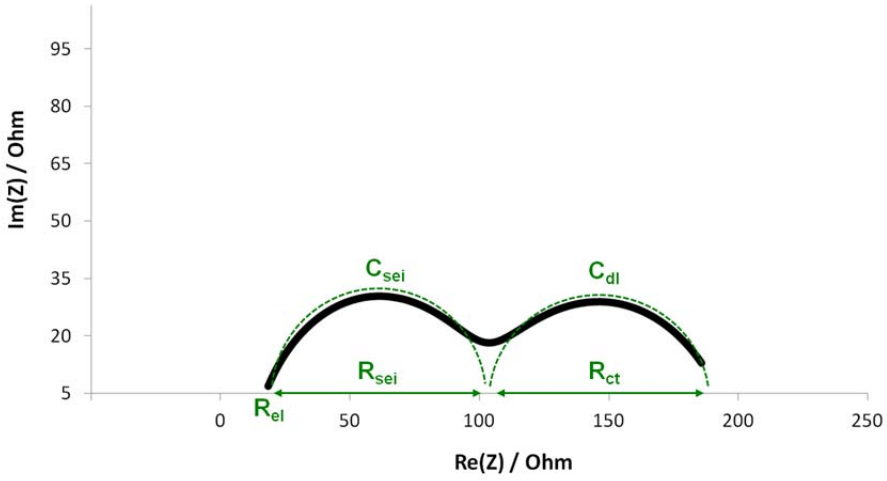

Figure 6-8 cathode at the end of the first formation cycle. Bias voltage 5mV, frequency range 100kHz-50mHz.

Unlike pristine condition, the electrode responded differently in the low frequency region. In particular, an additional semicircle has been observed between 100 kHz and 0.1Hz. According to literature, the diameter of this semicircle has been attributed to the charge transfer resistance of intercalation processes ($\mathbf{R_{ct}}$). As previously motioned, a circular shape of an EIS spectrum originates from dipolar relaxation processes. Considering the low frequency domain, this imaginary contribute can be attributed the dipolar relaxation of the electrolyte.

Considering all these evidences, one can concluded that cathode behaved as non-blocking electrode, intercalating and deintercalating Li^+ during charge and discharge processes, respectively.

Figure 6-9 reports in black and green the EIS spectra recorded at the end of the 5th and 10th charge/discharge cycles, respectively. By comparing these spectra with one data reported in Figure 6-8 one can notice that formation cycles induced an increase of $\mathbf{R_{el}}$, which resulted stable during cycling. On the contrary, by comparing spectra in Figure 6-9 one can observed that the second semicircle weakly contracted, which lead to conclude that $\mathbf{R_{ct}}$ parameter weakly decreased, as expected for a well performing cell.

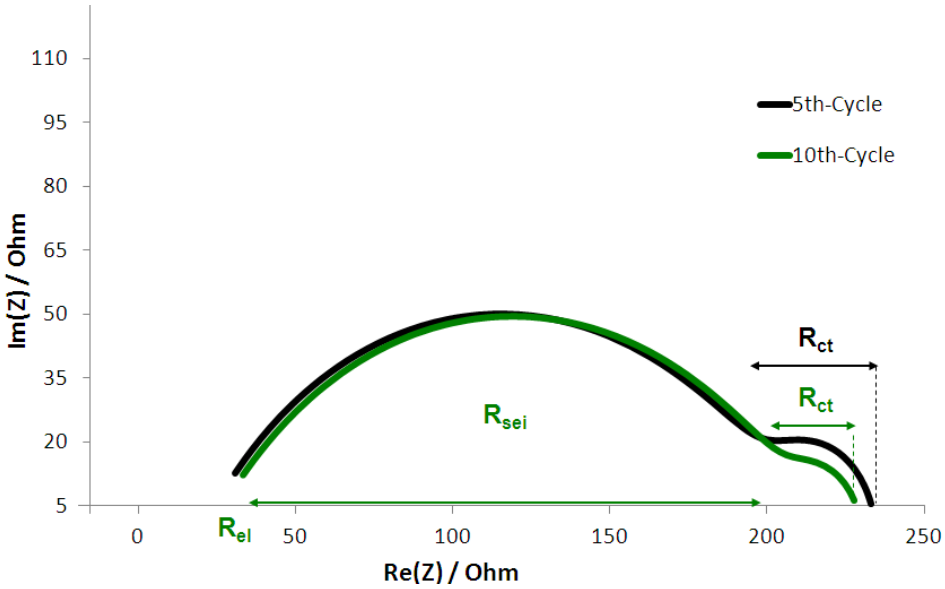

Figure 6-9 cathode at the end of the 5th (black) and 10th (green) charge/discharge cycles. Bias voltage 5mV, frequency range 100kHz-50mHz.

Similar observation might be done taking into account EIS results obtained by anode and therefore they have not been reported. Additional details about EIS measurements and the relative theoretical descriptions have been reported in paragraph 3.9.

Beside qualitative information about the electrochemical behaviour of cell components, the main output of this technique is the quantification of each resistance and capacitance presents within the electrochemical system. To do so, each spectrum should be

interpolated by using a proper equivalent circuit. The spectra of blocking and non-blocking electrodes have interpolated by using "$R_{el}+C_{sei}/R_{sei}+M_p+C_{dl}$" and "$R_{el}+C_{sei}/R_{sei}+C_{dl}/R_{ct}$" equivalent circuits, respectively. The schemes of these equivalent circuits have been reported in Figure 6-10

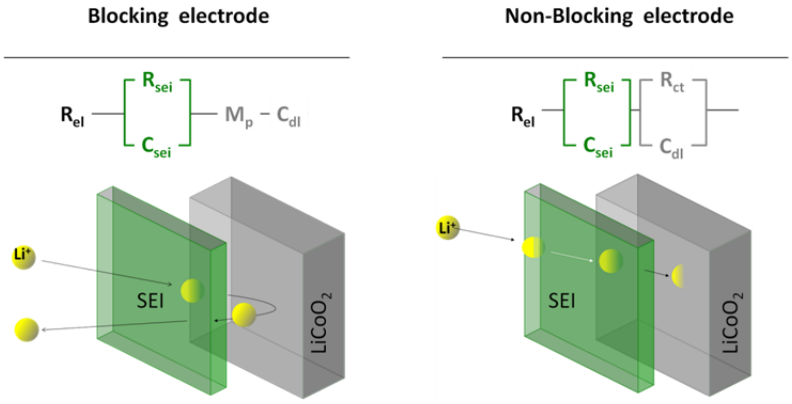

Figure 6-10 Equivalent circuits of the bucking and non-blocking electrodes

By comparing the time evolution of each cell parameter several observations could be done, understanding the cell behaviour during cycling. For example, Figure 6-11 reports the electrolyte ionic resistance (R_{el}) and the double layer capacitance C_{dl} parameters. Looking at the plots one can notice that GCPL experiment induced strong alteration in both R_{el} parameters. In particular, C_{dl} decreased after the first formation cycle and then stabilised. However the electrochemical stress induced by GCPL resulted from C_{dl} fluctuations, which could be explained by morphological alterations, occurred onto the electrode surface (SEI covering) and considering the local alterations occurred to the electrolyte permittivity (chemical alteration of the electrolyte composition).

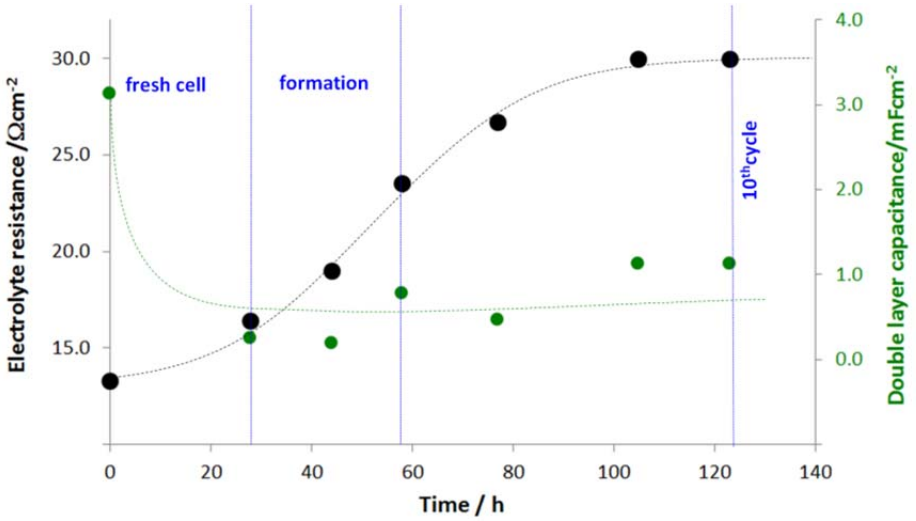

Figure 6-11 Time evolution of: (•) double layer capacitance, and (•) electrolyte resistance.

A further confirmation about the decomposition of the electrolyte is proved by the increase of $\mathbf{R_{el}}$ parameter**.** Such phenomenon is well-known in literature [2] and it due to the irreversible Li^+ Loss. In fact, the side reactions which build up the SEI, immobilised Li^+ cations within the passivation layers. Figure 6-12 reports the time evolution of both SEI resistance ($\mathbf{R_{sei}}$) and capacitance ($\mathbf{C_{sei}}$). Looking at the plot one can notice that $\mathbf{R_{sei}}$ increased during resting and then, revealing that SEI-layers have been thickening making longer the ion path across passivation layers. On the contrary, $\mathbf{C_{sei}}$ stabilised after the first formation cycle, confirming that SEI covered uniformly the electrode surface.

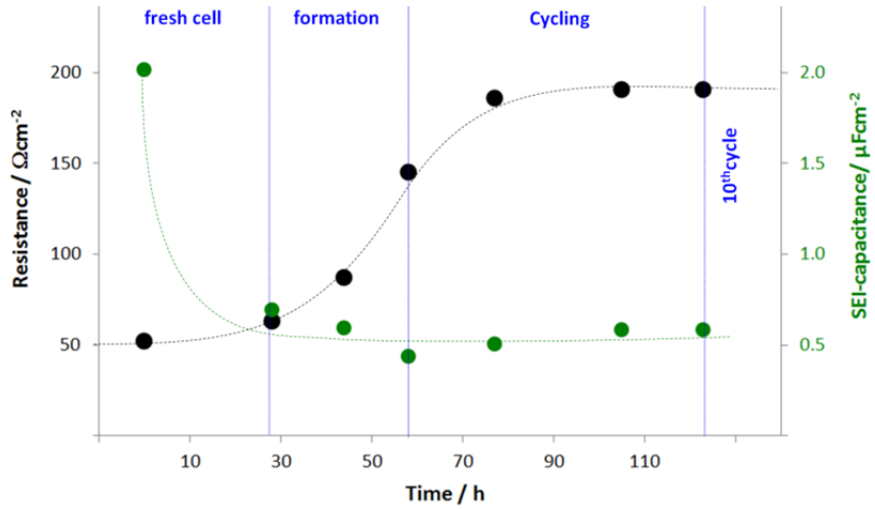

Figure 6-12 Time evolution of: (•) SEI capacitance, and (•) SEI resistance

As reported in Figure 6-13, EIS measurements revealed that Formation steps induced an alteration in the electrochemical behaviour of the electrode, reducing the charge transfer resistances and making it suitable for intercalation/deintercalation processes.

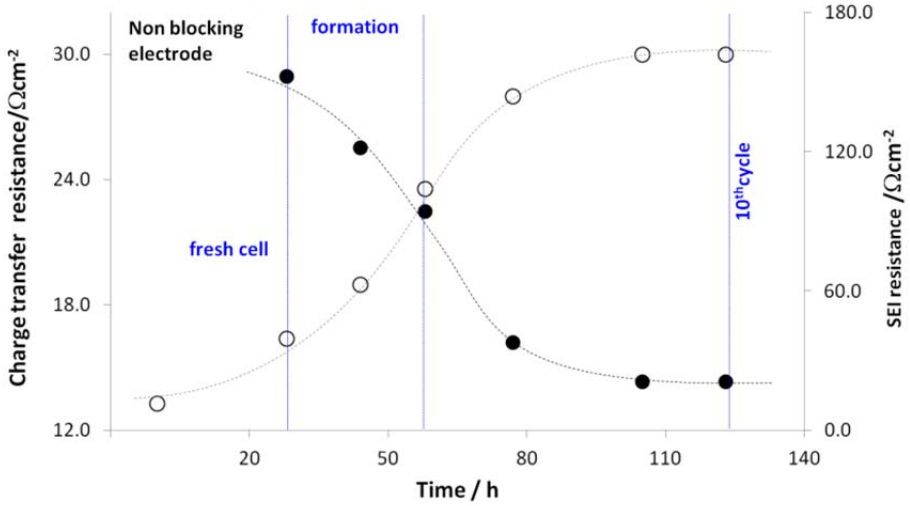

Figure 6-13 comparison between (o) SEI resistance, and (•) charge transfer resistance

Good linear correlations between $\mathbf{R_{el}/R_{sei}}$ and $\mathbf{R_{sei}/R_{ct}}$ variable couples have been found by performing parity plots (R^2>0.9). The correlation between $\mathbf{R_{el}/R_{sei}}$ highlighted a cause/effect relationship between the electrolyte decomposition and electrode passivation. Whereas $\mathbf{R_{sei}/R_{ct}}$ correlation confirms that an efficient electrode passivation leads to a well performing electrode.

In Figure 6-14 $\mathbf{R_{sei}}$ has been compared with CO_2-evolution. Looking at plots one can notice that CO_2 evolved as a consequence of both SEI-growing and it stopped when $\mathbf{R_{sei}}$ parameters stabilised.

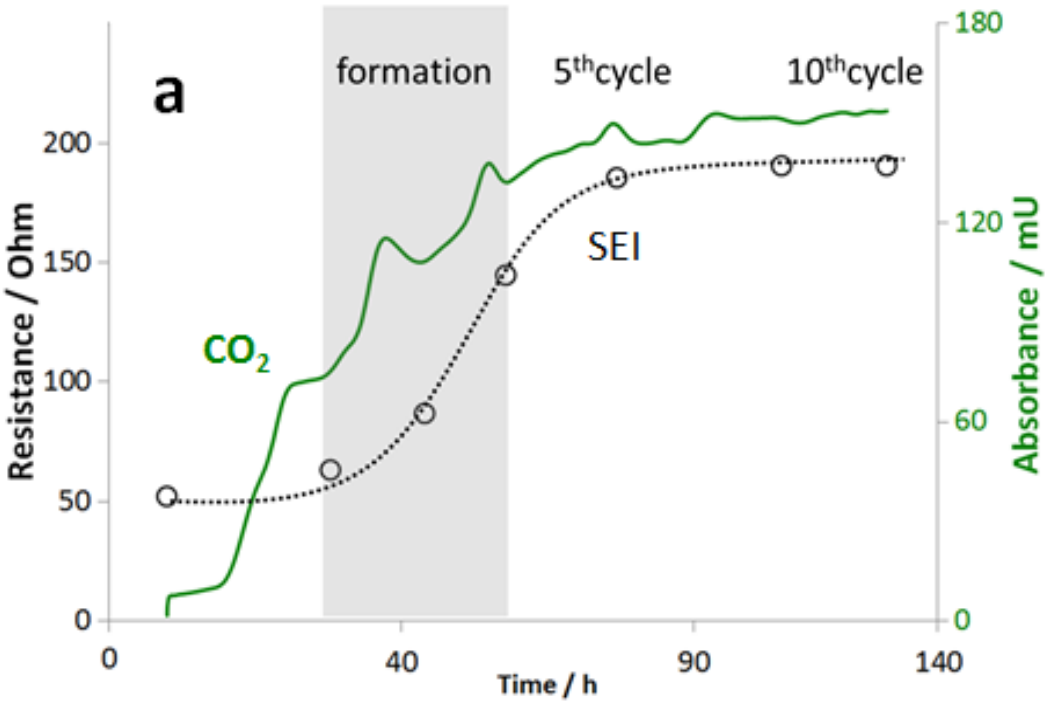

Figure 6-14 Comparison between EIS and FTIR measurements

6.5. CV/FTIR

In order to investigate deeply the dynamic of CO_2 generation, a Li-ion cell has been submitted to Cyclic Voltammetry (CV). Al/$LiCoO_2$, Cu/graphite and lithium has been configured as working (WE), counter (CE) and reference (RE) electrodes, respectively. Figure 6-15 schematises the electrochemical apparatus and its coupling to the FTIR system.

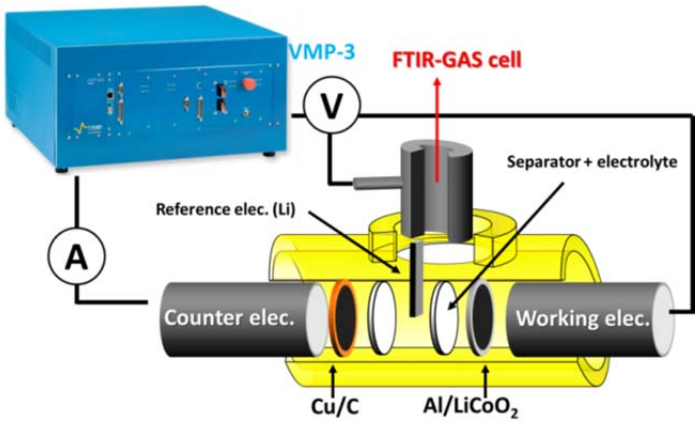

Figure 6-15 Experimental configuration for CV/FTIR measurements

The VMP-3 apparatus has been set to work in potentiostatic/galvanostatic mode. In particular, a potential difference has been imposed between WE and RE, CE closed the circuit, supporting conduction and preventing back currents through RE. By using this configuration, interferences have been avoided during potential measurements, because no alteration occurred to the Fermi level of RE.

The experiment consisted of ten potential scans, which ranged from 3.00V to 4.20V versus Li/Li^+. In order to have a time scale comparable to GCPL experiment (cycling stage, 5/C-rate), the scan rate has been set at $50\mu Vs^{-1}$.

Figure 6-16 reports an example of voltammetric traces obtained.

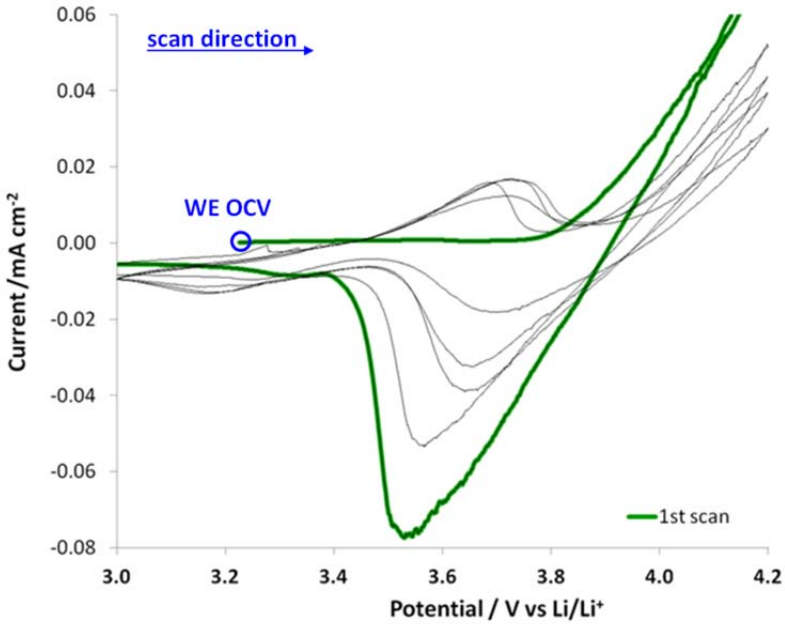

Figure 6-16 Cyclic voltammetry , $50\mu Vs^{-1}$, on full Li-ion cell (C/Lp30/$LiCoO_2$), (green) first cycle and (black) subsequent cycles.

Looking at the plot one can notice that no faradic processes occurred during the first anodic scan (from OCV to 4.20V vs. Li/Li^+), because the WE is fully lithiated in pristine

condition. However, a strong faradic current started to flow at 3.80V and it could be attributed to the oxidation of the electrolyte.

Unlike anodic scan, the first cathodic scan revealed a strong faradic peak at 3.55V. According to literature [] this signal has been attributed to the deintercalation of Li^+ cations from the WE lattice.

During the next voltammetric cycle, an anodic peak has been observed around 3.70V. According to literature [3], it has been attributed to Li^+ cations re-intercalation into the WE structure. However, the anodic current of this peak resulted lower than the cathodic current measured during the previous deintercalation process. These evidences lead to consider that a part of the Li^+ cations previously released by the WE, has been found not available for the further intercalation process. These evidences represent an additional confirmation about the irreversible Li loss mentioned to explain the time evolution of the electrolyte resistance (paragraph 6.4, Figure 6-11).

During the following scans, anodic and cathodic half wave potential approached and faradic currents became progressively more similar, as expected for a system which is becoming electrochemically reversible.

Usually side reactions, occurred to Li-ion cell, stabilised the electrode/electrolyte interface. As reported Figure 6-17, similar processes occurred during cyclic voltammetry. In fact proceeding with cycling, the oxidative decomposition of the electrolyte reduced progressively, Figure 6-17.

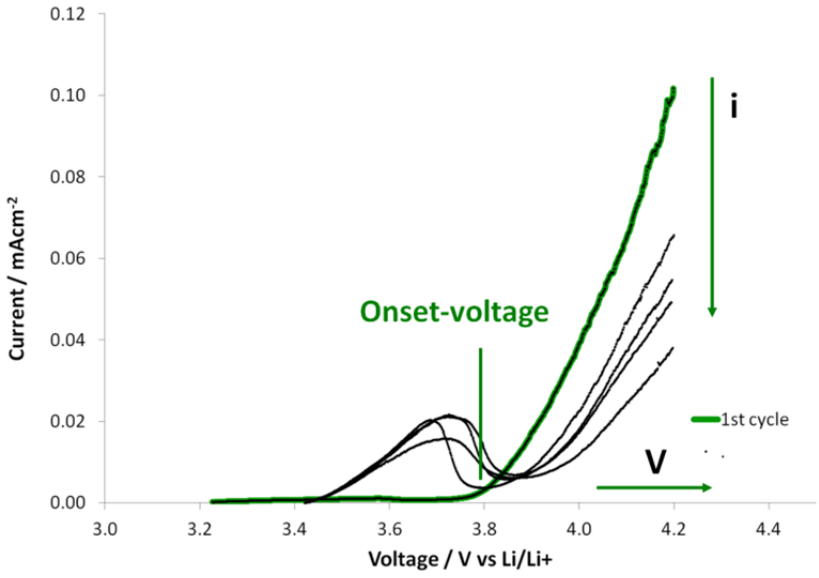

Figure 6-17 anodic scans of WE, 50µVs^{-1}

As reported in Figure 6-18, the onset potential of the anodic tail moved linearly to higher voltages (higher energies) and corresponding faradic current reduced, with an hyperbolic trend.

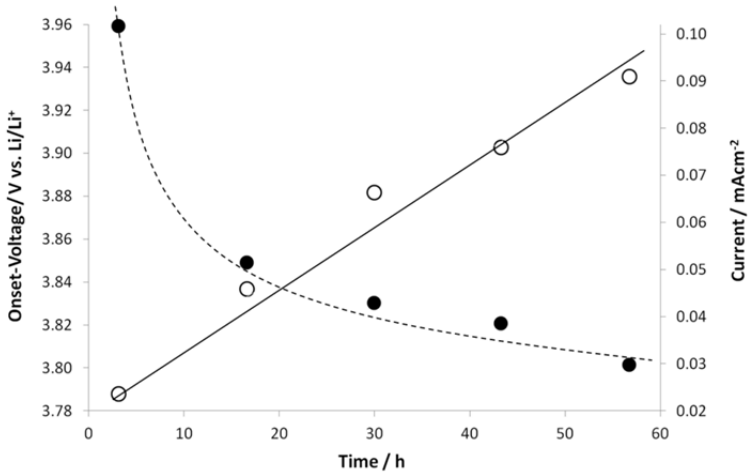

Figure 6-18 (O) Onset potentials and (●) faradic currents of the electrolyte decomposition

These evidences lead to speculate that the electrolyte decomposition peak move d to higher anodic voltage cycle by cycle. Thus one can conclude that the electrode surface has been stabilising for all the CV experiment.

Additional information about decomposition processes might be obtained, looking at the cathodic scans in Figure 6-19. In particular, irreversible cathodic peaks positioned around 3.20V have been observed. These peaks are not usually observed by performing backward scan on pristine cathode. Thus one can speculated that cathodic peaks are probably the expression of faradic process occurred to insoluble side-products, which rest embedded on the electrode surface after the anodic decomposition of the electrolyte.

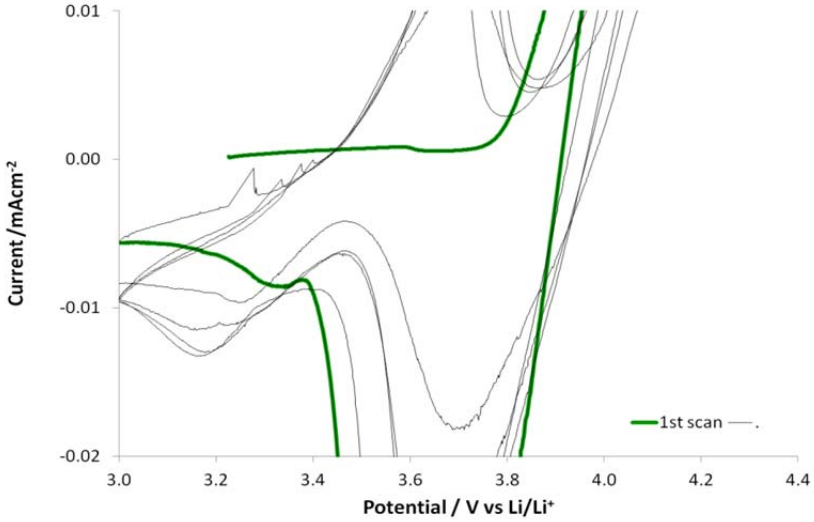

Figure 6-19 Cathodic scans of WE 50µVs^{-1}

As expected from voltammetric evaluations the oxidative decomposition of the electrolyte have led to CO_2 generation, which evolved as reported in Figure 6-20. CV results revealed that CV-cycling induced a CO_2 evolution, similar to what has been observed during GPCL experiment.

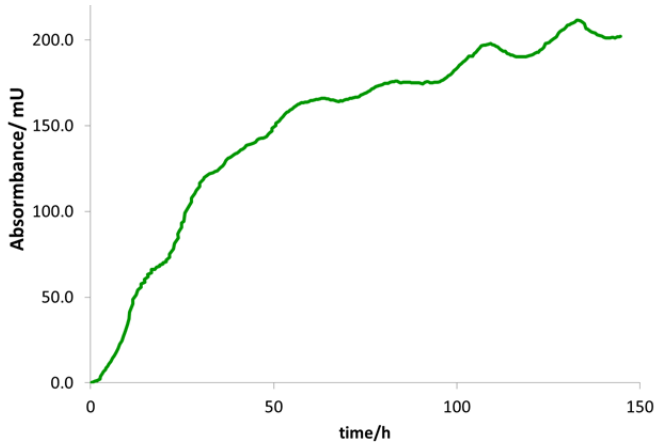

Figure 6-20 CO2 evolution during CV experiments.

An interesting correlation has been observed by comparing the FTIR absorbance with the current response measured during CV experiments,

Figure 6-21. In particular, CO_2 stared to evolve when the cell reached the onset potential of the anodic tail (3.80V vs Li/Li^+), which must correspond to the oxidative decomposition of the electrolyte.

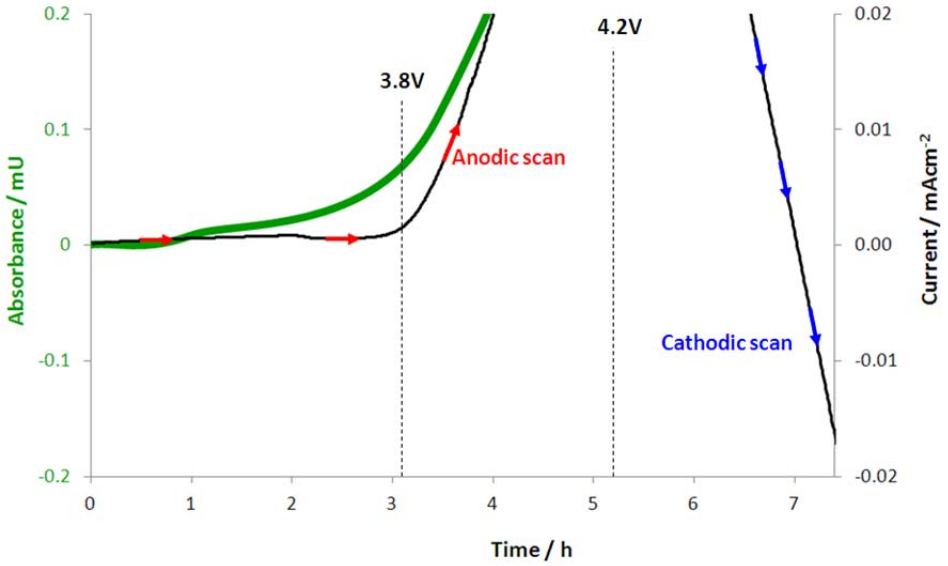

Figure 6-21 CV/FTIR measurements. CO_2 absorbance 2360 cm^{-1}

Considering that anodic polarization induces vacancies in the cathode valence bands, CV evidences confirm that CO_2 is generated by oxidations occurred at cathode/electrolyte interface.

CV and GCPL experiments induces electrochemical processes under thermodynamic and kinetic controls, respectively and both experiments proved that CO_2 has been generated

by oxidative processes that start around 3.80V (operative voltage of commercially available device)

6.6. SEM/EDS ex situ characterization

Ex-situ characterizations have been performed by using electron scanning microscope (SEM) equipped with the EDX probe (energy dispersive X-ray spectroscope). SEM has been set to work in back scattering electron mode, in order to have micrographs sensitive to atomic weight.

Micrographs reported in Figure 5-12-a abd Figure 5-12 -b refer to the cathode before and after cycling (10 cycles at C/5), respectively. Before GCPL, $LiCoO_2$ electrode appeared bright with occasional dark spots which are probably residues of the organic binder (polyvinylidene fluoride, PVdF). After cycling, SEM revealed the presence of a sponge-like coating, which covered the electrode surface. The rough morphology of the coating confirmed that the electrode specific surface lowered by cycling the cell. This could account for the fluctuations of C_{dl} and C_{sei} parameters, which have been monitored by EIS.

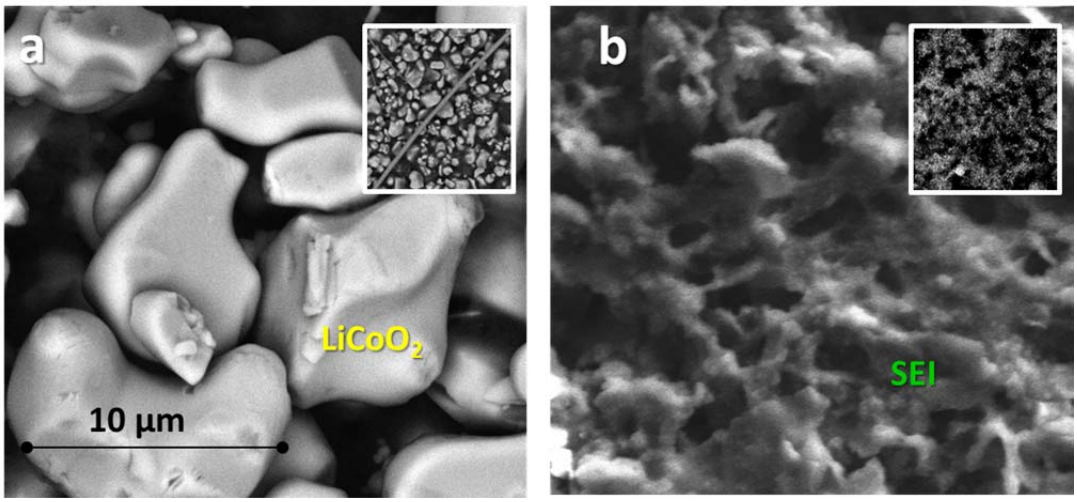

Figure 6-22 LiCoO2 electrodes: (a) electrode before GCPL , (b) electrode after GCPL. Micrographs performed by secondary electrons

The chemical composition of the coating has been characterised by X-ray energy dispersion spectroscopy (EDX, Figure 6-23).

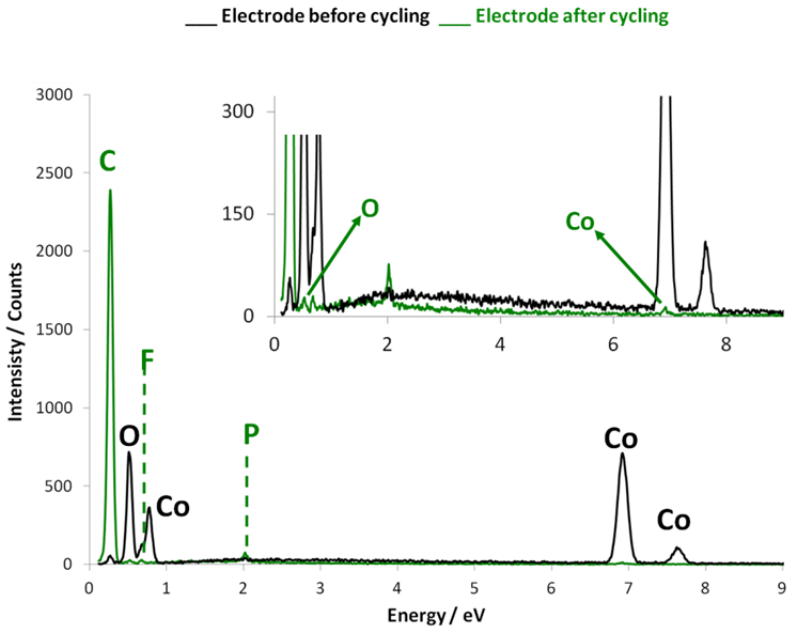

Figure 6-23 EDC spectra on LiCoO2 electrode before and after ageing

As depicted in Figure 6-23, the pristine cathode revealed strong peaks due to Co and O X-ray emissions, respectively. However, weak signals due to C and F atoms have been observed because of the PVdF-binder presented at the electrode surface. After cycling, the diagnostic signals due to Co and O completely disappeared because of the SEI gowning, which increased its thickness, making the electrode surface barely accessible to the electrons beam. Moreover, light atoms such as C and P have been easily revealed by EDX probe, confirming that coatings consisted of electrolyte decomposition products.

6.7. Conclusion

The evidences obtained by GCPL, EIS and CV proved that CO_2 evolution occurred preferentially at the cathode side. The oxidation of solvent occurred, generating CO_2 and other insoluble side products, as shown by EIS and CV. Insoluble products are embedded in the electrode coating and are able to stop CO_2 evolution, avoiding a chemical contact between the electrolyte and the electrode (passivation). However, intercalation/deintercalation processes, expands and contracts the electrode lattice inducing a mechanical stress on passivation layers. Fractures and craters could be originated by local tension and they can uncover partially the electrode, leading to a further decomposition of the electrolyte.

This mechanism represents one of main causes related to the mechanical failure of Li-ion cells, under operative conditions.

Although mechanical failure seldom occurred during these experiments, performance declines are more relevant and frequent phenomena. In fact, it has been proved that CO_2 works as a redox shuttle. In particular, the cell reduced CO_2 at anode during discharge. Reductions consumed electrons, leading to a less discharge efficiency and a fast self-discharge. Moreover, CO_2 reduction contributes to the irreversible capacity loss, immobilising Li^+ cations in the SEI coating.

Summarising, although a well performed electrode passivation could prevents such adverse effects, it cannot be considered as conservative approach. In order to present at the market safe and well performing Li-ion cells, CO_2 should be completely avoided by using a scavenger, specifically configured.

6.8. Reference

1. P. Arora, R. E. White, Marc Doyle J. Electrochem. Soc. 1998 volume 145, issue 10, 3647-3667
2. C.Wang, A.J. Appleby, F.E. Little Journal of Electroanalytical Chemistry 519 (2002) 9 – 17
3. B. Huang, Y-I. Jang, Y-M. Chiang, D. R. Sadoway Journal Of Applied Electrochemistry 28 (1998) 1365-1369

Chapter 7

Cells under resting and cycling conditions

7.1. Abstract

This paragraph compares the different behaviours of full Li-ion cells, in the course of resting and cycling experiments.

The electrochemical cells have been assembled according to the procedure described in the paragraph 3.3. Voltage profiles and electrochemical impedance spectroscopy results of have been reported in order to show the relation between the electrodes passivation and CO_2 generation. Electron scanning micrographs and EDS measurements have been described, revealing how resting and cycling conditions induced two different kind of electrode passivation, which differs for both morphology and chemical compositions. Finally, FTIR measurements have reported, assessing how resting and cycling conditions can determine different evolutions of CO_2.

7.2. Cell voltage profiles.

Figure 7-1 reports in black and green the cell voltage profiles due to Li-ion cells during resting and cycling experiments.

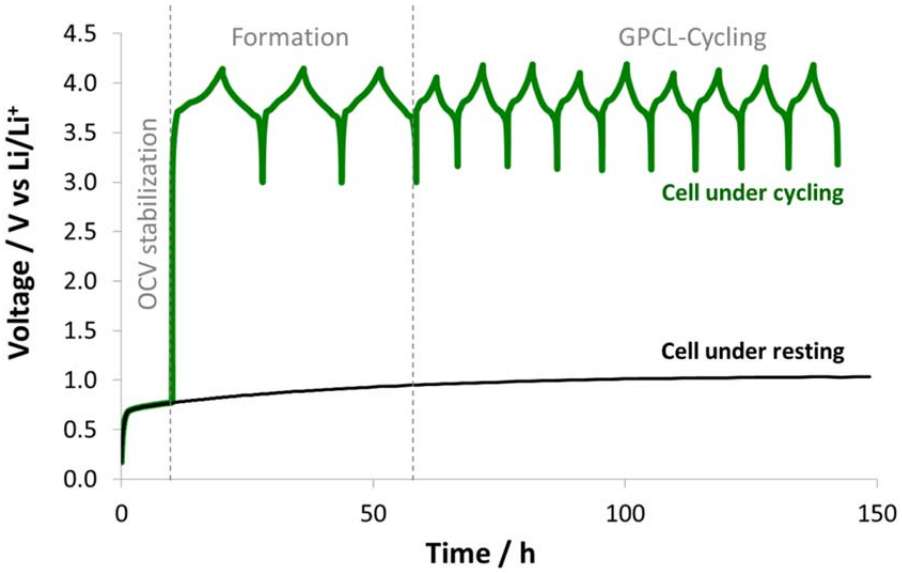

Figure 7-1 voltage responses of cells during resting (black) and cycling (green) experiments. SEI Formation performed at C/10, cycling at C/5.

The first 10h of the cycling experiments involve a resting step, performed under OCV conditions and thus both cycling and resting experiments led to similar electrochemical cell behaviours.

After the first experimental step of 10h the electrochemical behaviour of cell under resisting conditions did not change significantly, reaching a plateau at 1.0V (vs. Li/Li^+). On

the contrary, the cell under cycling conditions revealed strong variations in the voltage profile, which increased and reduced by charging and discharging the cell [5]. Thus one can conclude that resting experiments simulate the behaviour of batteries during stocking into warehouse and cycling experiments simulate the behaviour of devices under operative condition.

7.3. EIS measurements.

According to the speculations about EIS experiments reported in Chapter 5 and Chapter 6, it results clear that electrodes passivation is the main cause of gas evolution within Li-ion cells.

These speculations are principally based on resistance measurements and therefore the results concerning capacitances have been neglected in this paragraph.

Figure 7-2 reports in black and green the electrolyte resistance ($\mathbf{R_{el}}$) of Li-ion cells during resting and cycling experiments.

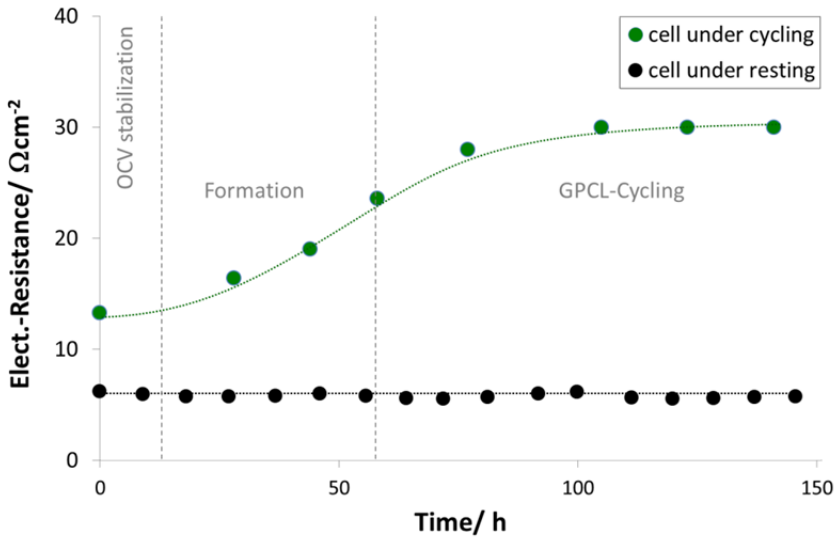

Figure 7-2 Resistance of the electrolyte during resting (black) and cycling (green) experiments.

The plot shows that all cells in pristine conditions have $\mathbf{R_{el}}$ close to 10 Ωcm^{-2}. In the case resting experiment, $\mathbf{R_{el}}$ did not change significantly and it fluctuated around values of 6-7Ωcm^{-2}. On the contrary, cycling experiments determined an increase of $\mathbf{R_{el}}$, which has been increasing during the formation step with a rate of 0.2$\Omega cm^{-2}h^{-1}$. According to literature (**REF**), the enhancement of $\mathbf{R_{el}}$ parameter has been attributed to decompositions processes occurred at the electrode/electrolyte interfaces. At the end of the formation step $\mathbf{R_{el}}$ parameter stabilised, thanks to a passivation coating (SEI , solid electrolyte interface) generated on the electrode surface (**REF**).

Errore. L'origine riferimento non è stata trovata. reports in black and green the resistances due to SEI layers ($\mathbf{R_{sei}}$), during resting and cycling experiments.

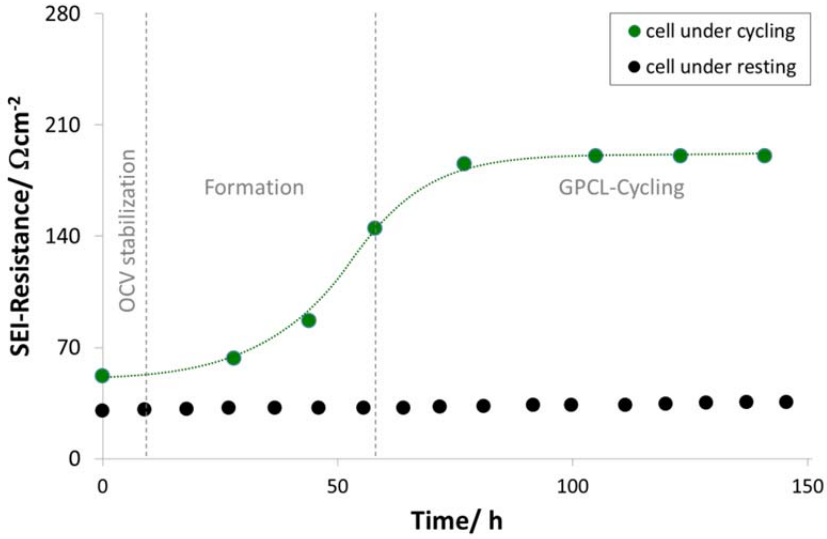

Figure 7-3 Resistance of the SEI under resting (black) and cycling (green) conditions.

The cell maintained under resting conditions showed a weak and linear enhancement of the SEI resistance, which had been increasing for all of the experiment with rate of 0.035 $\Omega cm^{-2}h^{-1}$. On the other hand, cycling experiments led to strong increase of SEI resistance, which had been increasing only on the course of the formation cycles with a rate of 2.7 $\Omega cm^{-2}h^{-1}$. According to literature (**REF**), the enhancement of the $\mathbf{R_{sei}}$ parameter has been attributed to the accumulation of insoluble side products, which remained embedded on the electrodes surfaces (growth of passivation layers) (**REF**).

At the end of the formation cycles $\mathbf{R_{sei}}$ parameter stabilised, thanks to the presence of SEI layers, which avoided further decomposition processes at the electrode/electrolyte interfaces.

In conclusion, EIS experiments emphasises that chemical alterations occurred to cell components during both resting and cycling experiments.

Resting experiments induce weak and continuous chemical alterations of the cell components. For the time scale of this kind of experiment one can conclude that resting conditions impact weakly on the electrochemical behaviour of the cells. However, taking into account a long time scale experiment (a few months), one can speculate that cell degradations occurred under resting conditions could significantly comprise the safety of cells.

On the other hand, cycling experiments impact more on cell components. However, strong resistances increases have been observed only in the course of the formation

cycles. Thus formation is a crucial experimental step, which make the cells suitable for GCPL-cycling.

7.4. SEM micrograph.

As prove by EIS results both resting and cycling experiments lead to electrodes passivation. In order to assess the morphology of SEI layers, SEM measurements have been performed on Al/$LiCoO_2$ electrodes at the end of each experiment.

Figure 7-4a and Figure 7-4b report the SEM micrographs of Al/$LiCoO_2$ electrodes after resting and cycling experiments. The micrographs have been obtained by the means of secondary electrons and thus fresh $LiCoO_2$ appears as bright grains and passivized grains appear darker.

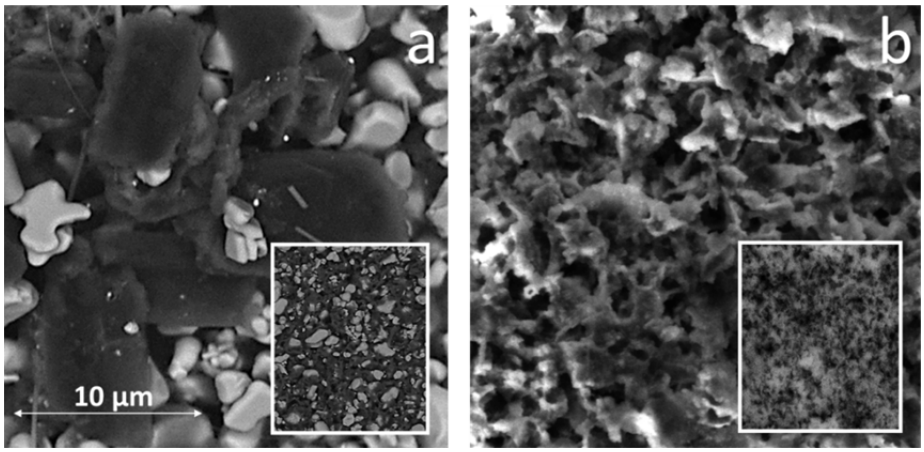

Figure 7-4 SEM micrograph of SEI after resting experiment (a) and after cycling experiments (b). Micrographs obtained by secondary electrons

The micrograph in Figure 7-4a reveals that rest induces an extremely localised passivation. SEI layers grew on some grains, leading to a random coverage of the electrodes surface. Summarising, electrodes after resting experiments exhibit a mosaic-like passivation.

The micrograph in Figure 7-4b reveals that after cycling an organic coating covers homogenously the electrodes surface. Summarising, cycling experiments generate a sponge like passivation coatings.

The micrograph in Figure 7-4a and The micrograph in Figure 7-4b schematise the structures of the SEI coatings deduced by SEM observations. Looking on the sketches one can understand that resting induced weak and extremely localised decomposition processes. On the contrary, an extended decomposition of the electrolyte has been observed during cycling, which resulted from an homogeneous coverage of the electrode.

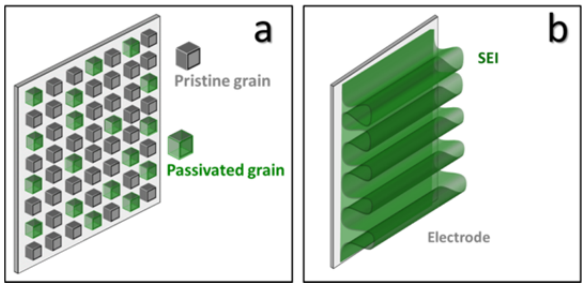

Figure 7-5 Schemes of the SEI structures after resting (a) and cycling (b) experiments.

7.5. EDX measurements

The chemical composition of the SEI coatings has been characterised by X-ray energy dispersion spectroscopy (EDX). The measurements have been carried out by focusing the electron beam on the electrodes surface and by measuring the energy of the out coming X-photons.

Figure 7-6 reports in green and black the spectra of Al/$LiCoO_2$ electrode at the end of resting and cycling experiments.

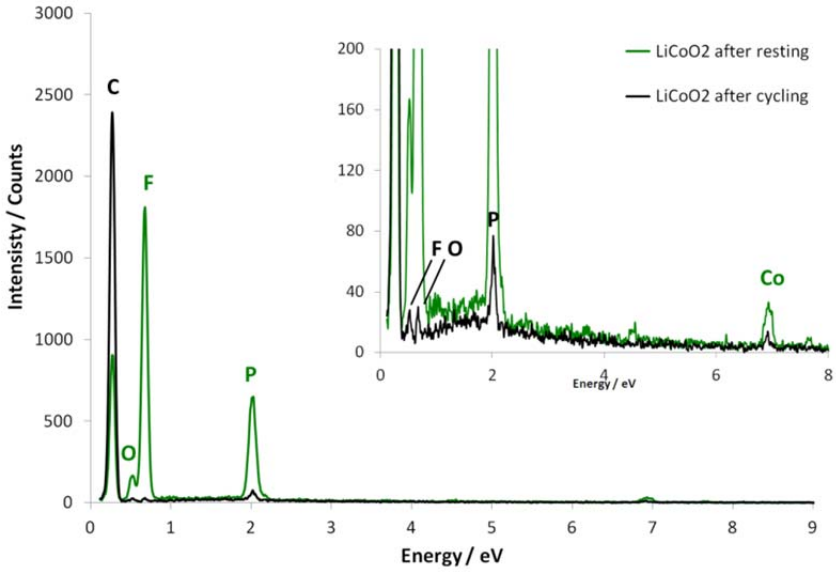

Figure 7-6 EDS spectra of $LiCoO_2$ electrode after resting (green) and cycling (black) experiments.

EDX measurements reveal that resting generates SEI coatings, which consist of fluorine and phosphorus atoms, which according to literature [6] have been attributed to the inner region of SEI (crystalline domain). On the contrary cycling experiments generate SEI coatings that consist principally of carbon atmos. According to literature [6] these signal have been attributed to the outer region of SEI (polymeric domain). Moreover, the signals of Co substrate which were barely detectable in the spectra after resting, resulted undetectable after cycling. Thus, one has to conclude that cycling induces a passivation

coatings which is thicker than free electron path across the soft matter (hundreds of nanometers).

Summarising, the different experimental conditions determine different chemical composition within in the SEI layers and the greater abundance of carbon after cycling experiment lead to speculate about a stronger electrolyte decomposition induced by formation cycles.

7.6. FTIR measurements.

All the evidences proved that Li-ion cells are quite stable under resting conditions, and they could be stabilised during cycling experiments, by performing formation cycles. However, It still unclear how SEI growth impacts on the pressure build up within the cells. Figure 7-7 reports in black and green the pressure build-up of CO_2 into Li-ion cells during resting and cycling experiments.

Measurements have been carried out by the means of FTIR spectroscope, calibrated to work in absorbance optical mode at 2360 cm^{-1}.

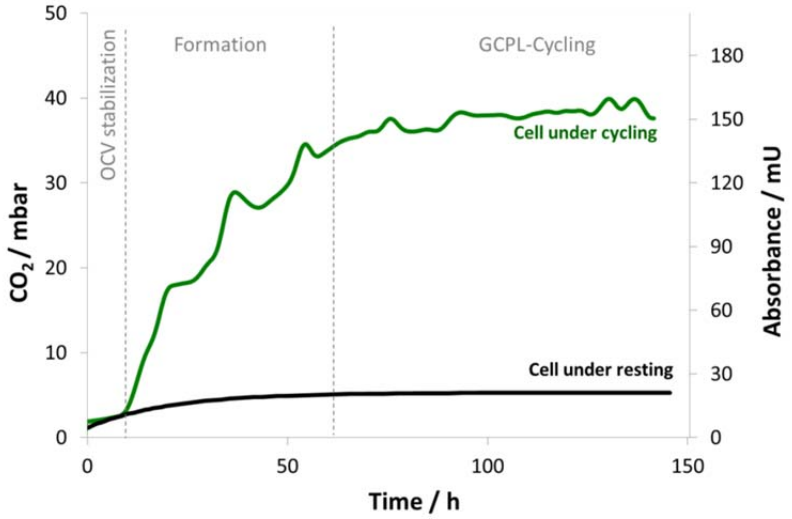

Figure 7-7 Evolution of CO_2 under resting (black) and cycling (green) conditions. CO_2 absorbance measured at 20360 cm^{-1}

The FTIR data revealed that in both conditions CO_2 evolves from the cells. The CO_2 generation appears quite similar in the experimental steps related to the OCV stabilisation.

In the course of the resting experiments the pressure builds up slowly, reaching a plateau at 5mbar. On the contrary, the cycling experiment induced a strong pressure builds up, which reached a pressure upper bound of 40mbar.

Taking into account that resting experiments simulate the behaviour of batteries during stocking into warehouse, one can speculate that resting might represent a long term

safety issue. In the particular case of cells with a wide electrodes surface (eg. 300cm^2), one can expected that resting can determines a pressure build of a few bars.

On the contrary, the pressure build up due to cycling, represents a short time safety issue. Among all of the experimental stages of both resting and cycling tests, the most important contribute to pressure build has observed in the course of the formation cycles, which induced a pressurization of approximately 35 mbar.

Assuming the decomposition reactions reported in Figure 7-8 one can assess the percentage of electrolyte decomposed to produce CO_2.

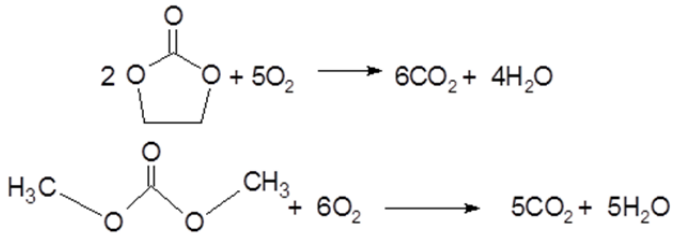

Figure 7-8 decomposition reactions of EC/DMC based solvente

Calculation lead to speculate that resting and cycling decomposed approximately the 0.5% and 7% of the electrolyte.

7.7. Conclusion

Although formation cycles are able to stabilise the electrode surface, preventing decomposition processes and limiting the pressure build-up, it is not conservatory to consider it as a solution aimed at preventing and avoiding adverse effects due to gas accumulation within Li-ion cells.

In fact, mechanical damages can occur to SEI during cycling, according to the dynamic behaviour of intercalation stage compounds (expansion/intercalation, contraction/deintercalation). Moreover, SEI consists of ionic species which could dissolve into the electrolyte exposing portions of the electrode to fresh electrolyte. These happenings lead to additional decompositions, which further pressurise the cell.

Taking into account that CO_2 promote self-discharge, behaving as a redox shuttle between cathode and anode, one can speculate that eliminating this gas secondary side reaction based on CO_2 will be avoided, increasing the capacity retention and columbic efficiency of the cell. For all these reasons a scavenger directed against CO_2 is mandatory to present on the market cell with longer time life, greater safety and better performances.

7.8. Reference

5. M.B. Armand Materials for Advanced, 21, 1981, pp 271-311
6. S. Shi, P. Lu, Z. Liu, Y. Qi, L.G. Hector, H. Li, S.J. Harris J. Am. Chem. Soc. 2012, 134, 15476−15487

Chapter 8

Gas management solution for Li-ion technology

8.1. Abstract

On the base of a review in literature concerning the possible side reactions occurring in the battery cell, the experimental work has been directed to the selection of a CO_2 getter material. A screening of candidate material has been carried out according to their supposed ability to capture CO_2. The goal of the experimental task was the assessing of the theoretical sorption capacity of these materials in the presence of the organic solvents, by means of volumetric measurements. This chapter contains a detailed description of the experimental protocol carried out by using a sorption bench entirely designed and built in SAES. The main results obtained from the CO_2 sorption measurements have been reported, showing that the LiOH is the most promising material to develop a gas management technology.

8.2. Experimental apparatus

A series of candidate materials has been screened by using a dedicated volumetric static bench. The experiments have been carried out by measuring the pressure decrease of CO_2 in a volumetric static bench, which has been set to work in isolated conditions. Figure 8-1 reports the volumetric apparatus.

Figure 8-1 Volumetric sorption bench dedicated to CO_2

The layout of the measuring system is reported in Figure 8-2. The system allows for testing two samples at the same time in independent mode. It comprises 5 functional

modules: a pumping unit (VACUUM), 2 sample units (SAMPLE 1-2), 2 gas inlet units (GAS INLET 1-2), and a solvent inlet unit (SOLVENT).

The gas inlet unit comprises a capacitive vacuum gauge, CAP1 (F.S. 5000 Torr) and a chamber, VE whose volume can be modified according to the experiment requirements. The gas inlet module is connected with three gas lines at high pressure (CO, CO_2, Ar) by the sapphire valves V6, V7 and V8. Downstream of the gas inlet module is the sample unit, connected through the automatic valve V11 and the valve V10. The heating cord R3 and the Gefran thermoregulating unit are used for the bench baking.

The sample unit comprises a quartz bulb, two capacitive gauges CAP2 and CAP3 (F.S. 2000 Torr and 10 Torr, respectively), the valve V13 connected to the pre-vacuum and the valve V1 connected to the high vacuum system. The valve V14 isolates BL1 from the solvent inlet unit. The whole unit is thermoregulated by means of a heating cord R4. The temperature of the bulb is regulated by R1. The bulb can be removed from the system by the valve V12 for handling samples in glove box where needed.

The solvent inlet unit comprises a quartz bulb which is isolated from the system by the valve V14. The bulb is thermoregulated by using a muffle to heat and an alcohol/liquid nitrogen solution to freeze the solvent.

The vacuum unit comprises a turbomolecular pump and a scrolling pump. It is connected through V5 and V3 (pre-vacuum) and V4 and V1 (high vacuum) to the gas inlet module and to the sample module. The scrolling (oil-free) pump is suitable for organic solvent vapours.

All system modules can be connected directly to the pre-vacuum by-passing the turbomolecular pump: this makes the test steps independent from each other and limits the contamination of the system in the most critical steps, such as the solvent conditioning and the thermal treatment of the sample.

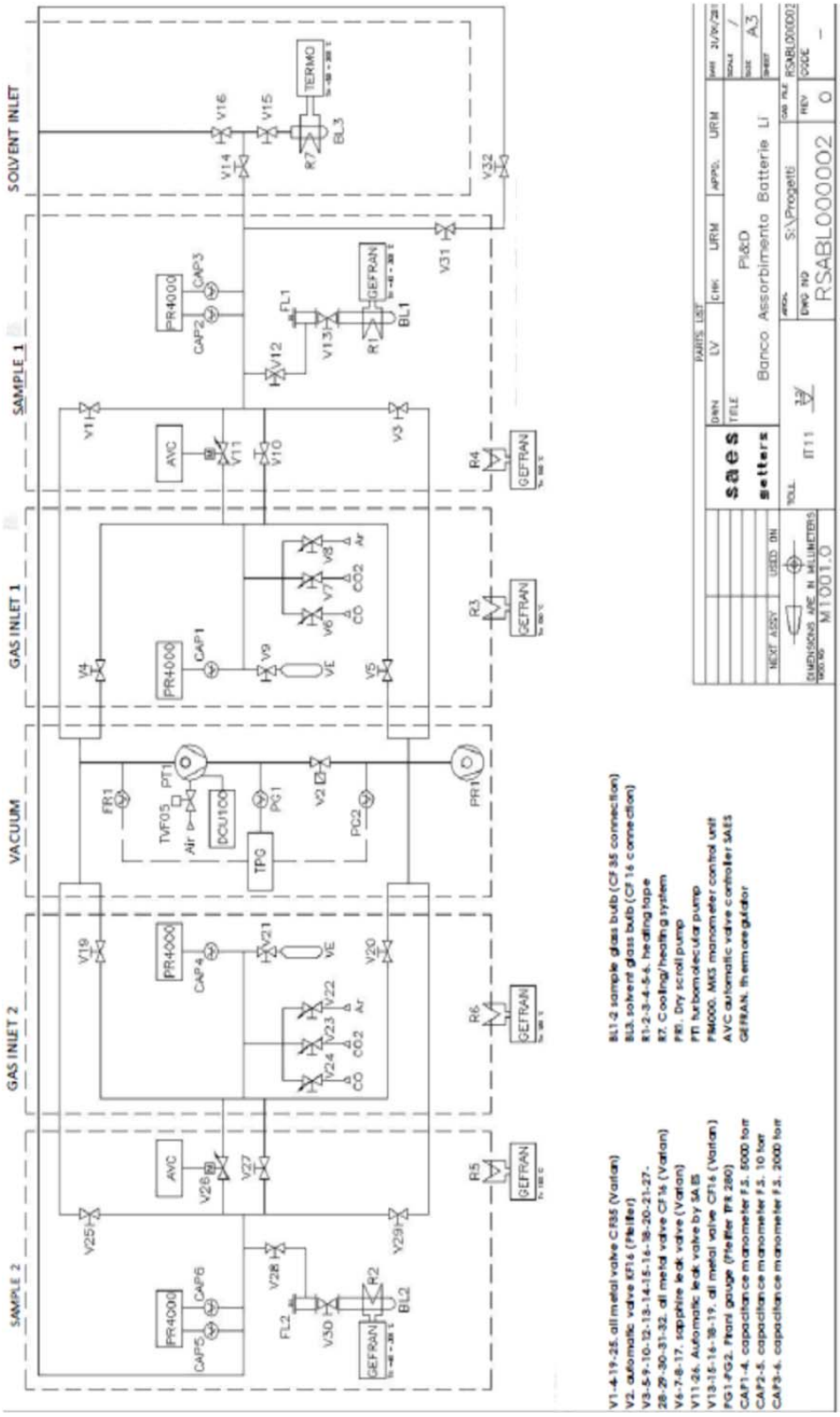

Figure 8-2Layout of the volumetric sorption bench.

8.3. Experimental procedures

After the review of the possible side reactions occurring in the battery cell, the experimental work has been directed to the selection of a CO_2 getter material. The getter material must not react with electrolytes, in order not to jeopardize its sorbing properties and to avoid the release of harmful substances in the battery. The sorption tests were carried out according to the following procedure.

- *Solvent conditioning*

The solvent must be conditioned by removing the non-condensable gases, which are dissolved in it. Conditioning is carried out by means of freezing-thawing cycles. The solvent is cooled down to -50 °C and the non-condensable gases are removed by pumping. Then the bulb is isolated from the system and thawed so that the gases that were dissolved in the solvent can be released in the headspace. This procedure is repeated 5 times.

- *Baking of the gas inlet and the sample units*

The baking is carried out under vacuum at 150 °C for 12 hours. After tests using solvent vapours, the system is always subjected to a baking step prior to the next test.

- *Sample Holding*

The sample is weighed and inserted into BL1. The bulb is then gradually pumped by connecting it first to the pre-vacuum and then to the high vacuum line.

- *Sample thermal treatment*

The sample can be subjected to a vacuum thermal treatment according to the nature of the sample. It is important that the temperature of the system is lower than the temperature of the sample, avoiding the condensation of impurities. The heating accelerates the removal of such contaminants by using the pumping units.

- *Solvent inlet*

After isolating the pumping units, the solvent vapor is expanded from the gas inlet into the sample units through V15 and V14. When the pressure of the solvent stabilizes, the gas inlet is closed. The partial pressure of the solvents is ruled by the minimum temperature in the bench. The solvents selected for these tests are Ethylene Carbonate (EC) and DiEthyl Carbonate (DEC) in 1:1 v/v mixture.

- *Sorption test in static condition*

After isolating the gas inlet unit from the sample unit, a known pressure of CO_2 is loaded in the gas inlet module, monitoring the pressure by CAP1. The gas is then expanded in the sample volume unit by opening V10 and the pressure on the sample is monitored by means of CAP2 and/or CAP3 until a steady state condition is reached. For the tests here reported, the samples were exposed to an atmosphere initially composed of CO_2 at 760 Torr and solvents vapors at 4 Torr. At the end of the test, the sample is extracted from the system and weighed. The weight difference is just a conservative indication of the sorbed CO_2 amount, since it does not consider the weight of the gases desorbed during the thermal treatment of the sample.

- *Measurement of the sorption quantity*

The same procedure described above is carried out for a blank test w/o sample, monitoring the eventual variation of the CO_2 pressure due to outgassing effects. By subtracting this curve to the one measured with the sample one obtains a pressure variation which can be entirely attributed to the sample absorbing action. All tests here reported were carried out at room temperature.

8.4. A survey of candidate materials

Table 8-1 reports the candidate materials for the screening.

Table 8-1candidate materials for the screening

	Theoretical CO_2 absorption (TorrL/g)	*Experimental CO_2 absorption (TorrL/g)*
Zeolite 13X	67	40
LiOH	388	259
NaOH	232	174

- *Reversible getters: Zeolites*

Zeolite X is the most widely studied sorbent for CO_2 capture. It has a caged structure and a Si/Al ratio of 1.3. The presence of alumina gives the framework a negative charge. Zeolite 13X is known to be very selective to carbon dioxide [1] due to the CO_2 quadrupole moment -1.43 10^{-39} C m^2 and polarizability 29.11 10^{-25} cm^3.

The tests performed on nanometric 13 X zeolites confirmed their ability to sorb CO_2, see Table 8-1. In order to normalize the results towards the random exposure to air, all samples were activated in bulb at 180°C for 60' under vacuum conditions. During this process, it was noted that pristine grains exposed to the solvents vapor changed their color from white to brown. It was then found that these samples were no more able to capture CO_2. This phenomenon may be related to the ingress of the solvent in the zeolite

pores, and to the following cracking of the carbonate molecules at high temperature. This result remarks the difficulty to separate CO_2 from the carbonate-based solvents by means of size selectivity. These difficulties origin from the similar Van der Waals radii of both molecules and therefore the molecular sieve is not efficient.

- *Irreversible getters: Alkaline hydroxides*

The second class of materials investigated is that of hydroxides of alkaline metals. Their reaction with CO_2 is already used in processes of air regeneration in closed enviroment.
In particular the lithium hydroxide reacts with carbon dioxide according to the following reaction:

$$2LiOH + CO_2 \rightarrow Li_2CO_3 + H_2O$$

LiOH and NaOH display the highest stoichiometric capacity for CO_2 that is 387 TorrL/g (92 wt %) for LiOH and 232 TorrL/g (55 wt%) for NaOH, and they were chosen for the screening tests.

- *Test 1. LiOH powder*

The tests revealed that CO_2 sorption by LiOH powder is immediate and it leads to a quick saturation. The sorption process is accompanied by a temperature increase, which is responsible for the small peak in the sorption curve observed in the first part of the experiment (Figure 8-3). Figure 8-3 reports the sorption profile of different types of LiOH-based scavenger. The profiles in red and brown refer to LiOH powder in CO_2 atmosphere and in CO_2 mixed with solvent vapors. The overall capacity is 259 torrL/g, vs. 387 torrL/g expected from the stoichiometric capacity of LiOH, see Table 8-1.

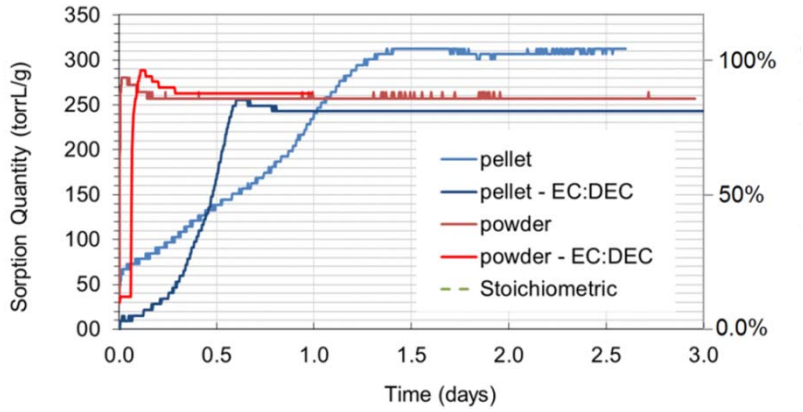

Figure 8-3 Absorption profile of different kind of LiOH: (light blue) free pellet,(blue) pellet in solvent (EC:DMC), (brown) free powder, (Red) powder in solvent (EC:DMC)

,

- *Test 2. LiOH and NaOH pellets*

By changing the morphology of the sample and testing the LiOH powder in pellet form, the kinetic of the sorption is modified with respect to the powder samples. Figure 8-3 reports in light blue and blue the sorption of a LiOH pellet in CO_2 atmosphere and in CO_2 mixed with solvent vapors (EC/DMC1:1 $_{v/v}$), respectively. The sorption is very fast at the beginning of the test, and slows down in the following minutes displaying an overall kinetic slower than that of the powder samples.

The morphology effect is evident also in the case of NaOH pellets, where the kinetic of the sorption resembles that of the LiOH pellets (data not shown). The observed sorption capacity was 311 TorrL/g for LiOH and 174 TorrL/g for NaOH.

An explanation for this sorption mechanism is following.

In the initial step, the reaction of the pellet with CO_2 generates the carbonate at the rate typical of this reaction. The carbonate is "passivating" the external surface of the pellet, slowing down the following steps of the sorption process. The reaction also produces water, but the carbonate solubility in water is not so high (1,31 g/100g H_2O at 20 °C), and therefore the CO_2 gas should go through a solid carbonate layer to reach the inner LiOH particles.

In the case of the powder samples, higher portion of LiOH surface is available for the reaction with CO_2 that proceeds so quickly that the carbonate does not have time to form a compact, passivating shell on the sample surface.

Concerning the difference between the experimental sorption capacity and the stoichiometric value, one should take into account that the pellets were prepared from a non-anhydrous powder and the water content has not been considered in the sample weight determination.

- *Test 3. LiOH pellet in presence of solvents.*

The sorption mechanism changes when the pellet is in presence of the solvents vapor. The reaction rate is slow since the first exposure to CO_2. After this slow sorption step, the process speeds up to a rate higher than that of the pellet in pure CO_2 atmosphere. At this stage, the sorption rate is 7 cc.torr/g sec^{-1} (vs. 2 cc.torr/g sec^{-1} determined in the test without solvents). The last part of the sorption curve shows a trend similar to that obtained from the tests on LiOH powders.

Keeping in mind the mechanism proposed for the pellet w/o solvent, one can speculate the following considerations. The missing fast sorption step suggests that the pellet have not a sufficient surface available to the gas sorption. This could be due to solvent condensation phenomena. In such a situation, the LiOH does not react with gaseous CO_2,

but with the gas dissolved in the carbonates that solvate the pellet. The gas dissolution in the solvent might be the rate determining step in the first part of the sorption process.
In the second step of the process, the sorption rate abruptly increases. The CO_2 likely saturates the solvent condensed on the LiOH pellet and it is now available and in intimate contact with the LiOH surface, the condensed solvent acting like a saturated carrier of CO_2. This counterbalances the initial hindrance to the CO_2 transport that was due to the compact morphology of the pellet, and the sorption process can proceed at a speed close to that showed by the LiOH powders.
The sample temperature monitored during the sorption tests apparently supports the interpretation elaborated above. The reaction of LiOH with CO_2 is exothermic and in fact at the beginning of the sorption process the sample temperature usually increases. In the case of the test 3, two temperature peaks are observed: the first occurs during the first, slow step of the process; the second one is in correspondence of the maximum slope of the fast part of the sorption curve. The trend of this latter part of the curve resembles that of the LiOH powder sorption and it is likely related to the actual reaction of LiOH with CO_2. The first temperature peak must be related to another phenomenon, characterized by a slower rate. This phenomenon can indeed be the dissolution of CO_2 in the condensed carbonate mixture, which is itself an exothermic process [2]. It is worth noting that neither the adsorption of EC:DEC nor the CO_2 sorption did damage the LiOH pellet that at the end of the test appeared swollen but not pulverized.
The main issue of the possible use of hydroxide-based materials is that water is present as a product of the reaction. The need to employ a H_2O getter material coupled with the hydroxides might lead to bulkier systems or systems that show a reduced capacity for CO_2.

8.5. LiOH as gas management solution

The main goal of the optimization of the gas management solution is to attain the compatibility with the battery application, both in terms of electrochemical stability and of sorption ability. The results shown above indicate that the best material responding to the requirements for a gas scavenger in battery environment is the LiOH, which should be chosen also for its higher CO_2 sorption capacity, even in presence of solvents.

8.6. Configuration of the getter

Although LiOH offers good efficiency in CO_2 absorption, it could not be directly used into Li-ion cells because the benefit concerning the CO_2 absorption does not compensate the negative effects due to LiOH dissolution (eg. fast electrolyte decomposition at high pH, [3]).

Configurations alternative to LiOH powders have been considered. In order to exploit the getter material in the battery cell, a suitable configuration has been designed taking into account the low-cost and environmentally sustainable manufacturability of the materials as well as the easiness of integration in the battery architecture. In order to confine the getter material powder (LiOH) and to avoid particulation phenomena inside the cell, the LiOH is dispersed in a polymer matrix obtained in the form of strips by an extrusion process. To test the concept, a first extrusion was carried out by using high-density polyethylene, HDPE and LiOH powder with 10-um particle size. The samples obtained have thickness ranging from 250 to 300 micron. The extruded sample have been characterised by the means of TGA/DSC apparatus, finding a loading of active phase approximately equal to 35 %.

A comparative experiment has carried out in solvent atmosphere (1 bar CO_2 + 10 Torr DEC vapors, 25 °C) by assessing absorption performances of milled powders and extruded samples. The sorption experiments have been reported in Figure 8-4, where light blue and red traces refer to 10μm LiOH powder and LiOH extruded in HDPE.

The sorption kinetic of the powder is not much improved by the reduced particle size, the sorption being very rapid even with non-milled powders (as reported in Figure 8-3). The fine-milled powder is still stable and its sorption properties are not affected by the presence of DEC solvent vapours.

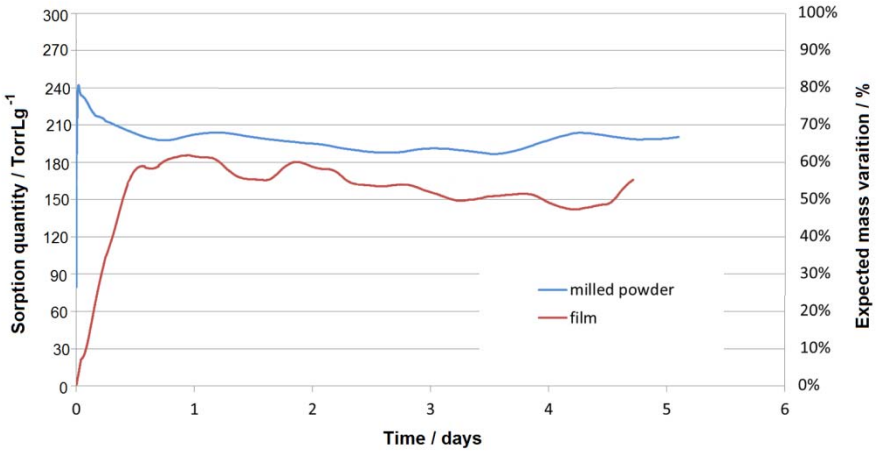

Figure 8-4 Absorption profile of CO2 due to 10um LiOH powders (1 bar CO_2 + 10 Torr DEC vapors, 25 °C)

The sorption mechanism starts as soon as LiOH is exposed to CO_2. After gaining 80 % of the initial weight, the sample slowly begins to lose weight until it reaches a plateau around 65 %. Obviously, at the beginning the sorption of CO_2 is so fast that it disguises the second, competitive process, which is the release of water according to the carbonatation reaction:

$$2LiOH + CO_2 \rightarrow Li_2CO_3 + H_2O$$

Moreover, the fast sorption kinetics at the beginning leads to some accumulation of water that is responsible for the initial extra weight gain (80 %). The release of water becomes evident only after LiOH approached its maximum capacity for CO_2. This assumption explains the second part of the curve, where a slow desorption occurs. The overall weight gain is calculated as 65 %, close to the value expected for the stoichiometric reaction of LiOH with CO_2 with a complete release of water.

Compared to the powder, the extruded getter has slower sorption kinetics. Most likely, in the case of the film the rate-determining step is the diffusion of CO_2 into the polymer matrix. In the film sample, it is possible to observe the resultant of the same phenomena described above. In this case, the sorption kinetics is slower so that the water can be progressively released during the sorption process. In fact, the weight increase is milder compared to the powder behavior, and the saturation point is reached without evidence of desorption phenomena. The plateau is around 55 wt%. Taking into account that a quantitative conversion of LiOH into Li_2CO_3 determines a mass variation approximately equal to 54%, the sorption performances of the extruded configuration might be considered efficient enough to carry out the role of CO_2 scavenger for Li-ion cells.

To avoid the drawbacks of water release, the extruded strip could be enveloped into an external polymer layer that might serve as a proper barrier for the water generated into the getter. Figure 8-5 schematized the getter configuration.

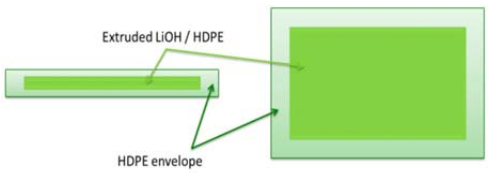

Figure 8-5 Schematization of the configuration of the getter for CO2

8.7. Conclusion.

A screening of candidate materials aimed at capturing CO_2 has been carried out, revealing that CO_2 could be efficiently captured by using LiOH. Although LiOH powders offer good efficiency in CO_2 absorption, they could not be used directly into Li-ion cells, because the

uncontrolled dissolution of its ions can interfere with the chemistry of the cell. In particular, a strong increase of pH can easily promote the electrolyte decomposition [3].

Summarising, the negative effects due to LiOH dissolution are not compensated by the benefit concerning the CO_2 absorption. For all these reasons the direct use of LiOH powders within Li-ion cell must be completely excluded.

Configurations alternative to LiOH powders have been considered, finding in extruded samples a promising configuration aimed at proposing a self-standing solution for gas management. LiOH has been extruded with HDPE, obtaining a composite material. This scavenger has been characterised, revealing good carbonatation yield. In conclusion, the experimental results suggest that extruded samples could be a useful solutions for gas management within Li-ion cell.

8.8. Reference

1. Hedin et al. Nanoscale 2 (2010) 1819-1824
2. Blanchard, Can. J. Chem. 81 (2003) 385-390
3. A.V. Plakhotnyk et al. J.of Fluorine Chemistry 126 (2005) 27-31

Conclusion

- The analytical part of the project have been concluded demonstrating that the analytical protocol based on FTIR spectroscopy is able to offer reliable quantification of the CO_2 gas generated in a Li-ion cell.

- An experimental procedure aimed at preparing Li-ion cells, on lab scale, has been optimized and validated according to specific electrochemical test protocols, taking as reference tests frequently reported in literature.

- Experiments carried out on full Li-ion cells have been performed in both resting and cycling conditions. Resting experiments simulate the behaviour of batteries during stocking into warehouses, and give an indication of the shelf life of the battery. Shelf life might by affected by long-term safety issue. On the other hand, the pressure build-up due to cycling represents a short-time safety issue. Among all of the experimental stages of both resting and cycling tests, the most important contribute to pressure build-up has been observed in the course of the formation cycles.

- The oxidative passivation of the electrodes resulted to be the main cause of pressure build-up in Li-ion cells, under both resting and cycling conditions.
  Experiments demonstrated that electrodes passivation might prevent side reactions, but it could not avoid the accumulation of CO_2 into the electrochemical cells. Thus, a screening of candidate materials aimed at capturing CO_2 has been carried out, revealing that CO_2 could be efficiently captured by using LiOH. Different configurations have been considered for the getter solution, finding in extruded samples a promising configuration aimed at proposing a self-standing solution for gas management in Li-ion cells.

Acknowledgments

I would like to thank SAES Getters company to have believed in this research project and to have funded it, providing my Ph.D scholarship. Moreover, I would like to extend my sincere thanks to Dr. Alessandra Fernicola and Mrs Anna Lisa Caterino for their supervision and help in the course of the daily experimental activity.

I wish to dedicate a personal acknowledgment to my colleges of CPC lab Dr. Stefano Zilio and co-workers for their analytical support.

I am grateful to dedicate a personal thought to Prof. Vertova to have introduced me to SAES Getters company and to have supervised the experimental work.

In the end I would like to thank my family and friends for their support during these years.